8-7-2020

Phenomenological identification of bypass transition onset markers using temporal direct numerical simulation of flat plate boundary layer

Satish Muthu

Phenomenological identification of bypass transition onset markers using temporal direct numerical simulation of flat plate boundary layer

By

Satish Muthu

Approved by:
Shanti Bhushan (Major Professor)
Like Li
Adrian Sescu
Yu Lv
Yucheng Liu (Graduate Coordinator)
Jason M. Keith (Dean, Bagley College of Engineering)

A Dissertation
Submitted to the Faculty of
Mississippi State University
in Partial Fulfillment of the Requirements
for the Degree of Doctor of Philosophy
in Mechanical Engineering
in the Department of Mechanical Engineering

Mississippi State, Mississippi

August 2020

Name: Satish Muthu

Date of Degree: August 7, 2020

Institution: Mississippi State University

Major Field: Mechanical Engineering

Major Professor: Shanti Bhushan

Title of Study: Phenomenological identification of bypass transition onset markers using temporal direct numerical simulation of flat plate boundary layer

Pages in Study: 115

Candidate for Degree of Doctor of Philosophy

Temporally developing direct numerical simulations (T-DNS) are performed and validated for bypass transition of a zero pressure gradient flat plate boundary layer to understand the interplay between pressure-strain terms and flow instability mechanisms, and to propose and validate a phenomenological hypothesis for the identification of a robust transition onset marker for use in transition-sensitive Reynolds-averaged Navier-Stokes (RANS) computational fluid dynamics (CFD) simulations. Results show that transition initiates at a location where the slow pressure-strain term becomes more dominant than the rapid term in the pre-transitional boundary layer region. The slow pressure strain term is responsible for the transfer of turbulence energy from the streamwise component to other components while the rapid pressure strain term counteracts with the slow term in the pre-transitional regime before transition onset akin to a shear sheltering like effect. The relative magnitudes of the slow and rapid terms thus provide a basis for the development of physically meaningful large-scale parameters that can be used as a transition onset marker for Reynolds averaged Navier-Stokes RANS simulations.

DEDICATION

Dedicated to my parents, Mr. and Mrs. Muthu and my sister Dr. Sumitha Muthu, who have inspired me to be what I am today.

ACKNOWLEDGEMENTS

The gratification and euphoria that accompany the successful completion of a project would be incomplete without mentioning those who made it possible. I would like to express my deep sense of gratitude and indebtedness to Dr. Shanti Bhushan for his incomparable counsel and indefatigable efforts, which were invaluable for the completion of this work. I appreciate our valuable discussions for my countless impromptu walk-ins. In addition, I would also like to sincerely thank Dr. Keith Walters for proposing the hypothesis which laid the foundation for this work. I would also like to thank all my committee members for their expertise and valuable input regarding this research.

I would like to thank the Department of Mechanical Engineering and Center for Advanced Vehicular Systems (CAVS) for all their financial and technical support during the research. This study was partly funded by CAVS and NASA EPScoR Project Number 80NSSC17M0039. All simulations were performed on Talon and Shadow HPC systems at the High-Performance Computing Collaboratory, Mississippi State University.

Finally, I would like to thank my parents and friends for their unconditional love and affection that kept me going through hard times. Sanderson center which was like a second home and together with TATW as well as ASOT provided me the required energy to push through and complete my work. Finally, a special shout out to Vicky Huang (wo de monku bubu) for all the help during my defense (All those practices and PPT tips definitely paid off ^_^).

TABLE OF CONTENTS

LIST OF TABLES

LIST OF FIGURES

LIST OF SYMBOLS

b_{ij} normalized anisotropy tensor

C_f skin friction coefficient

$C_{p'}$ critical ratio of the fluctuating pressure

$C_{R_{ij}}$ critical ratio of the pressure-strain correlation

C_{source} critical ratio of the fluctuating pressure source term

k turbulent kinetic energy, $k = \frac{1}{2}(u'^2 + v'^2 + w'^2)$

k_{2D} normal planar k, $k_{2D} = \frac{1}{2}(v'^2 + w'^2)$

p' fluctuating pressure

p'_r rapid/fast pressure

p'_s slow/return pressure

p'_{st} stokes/wall pressure

R_{ij} pressure-strain correlation

R^r_{ij} rapid/fast pressure-strain correlation

R^s_{ij} slow/return pressure-strain correlation

R_{ij}^{st}	stokes/wall pressure-strain correlation
Re_x	Reynolds number based on plate length
Re_θ	Reynolds number based on momentum thickness
Re_τ	Reynolds number based on mean friction velocity
Tu_{in}	free-stream turbulence intensity
U_∞	free-stream mean velocity
$\bar{u}_j$	Mean velocities
u'	streamwise turbulent fluctuating velocity
u'_{2D}	$u'_{2D} = \sqrt{2k_{2D}}$
$u_{\tau 0}$	mean friction velocity, $u_{\tau 0} = \sqrt{\tau_{w0}/\rho_0}$
v'	wall-normal turbulent fluctuating velocity
w'	spanwise turbulent fluctuating velocity
y	distance to the nearest wall
y^+	dimensionless wall distance, $y^+ = \frac{u_\tau y}{\nu}$
δ_0	initial boundary layer thickness
λ_2	second largest Eigen value of the Hessian of the pressure
τ_{ij}	Reynolds stress component
τ_{w0}	mean wall shear stress
ω	local mean vorticity magnitude

θ momentum boundary layer thickness

CHAPTER I

INTRODUCTION

1.1 MOTIVATION

Bypass transition from laminar to turbulent flow conditions is important in many engineering applications and impacts important flow quantities such as drag or heat transfer. Bypass transition occurs due to the presence of strong disturbances which are in turn induced by high free-stream turbulence, large wall roughness elements, flow separation, pressure gradient effects etc. [1] and entails strongly nonlinear phenomena. A review of the literature shows that its modeling in general is not mature enough to accurately predict flow behavior [2] over a wide range of complex geometries and flow conditions [3]. Direct numerical simulation (DNS) of canonical flows such as flat-plate boundary layers are very useful in understanding the transition flow physics. DNS have been performed for spatially developing flat-plate flows under a zero-pressure gradient [4–10]. However, these limited datasets are typically for moderate Reynolds numbers ($Re_x \sim 10^5$) and very high inlet free-stream turbulence intensities (Tu_{in}) ≥ 3%. This is primarily because for low Tu_{in} transition occurs at large Re_x that require significantly large flow domain and grid sizes.

An alternative to the spatial approach is the "temporally developing" approach. In this approach, the simulation is started with an initial condition and periodic boundary condition is applied along the directions. This allows the simulation domain to move along with the flow. It is expected that the solution at any instant is a realization of an infinitesimal section of the flat-plate

boundary layer. Such simulations require a smaller streamwise domain compared to the spatially developing counterparts, and thus are expected to be less computationally expensive by one to two orders of magnitude for high Re_x flows. Further, they allow for straightforward application of the numerically accurate pseudo-spectral solvers, especially fast Fourier transform (FFT). The approach has been commonly applied for DNS/ large eddy simulation (LES) of plane channel, mixing layer and jet flows [11–13]. However, studies have mostly focused on either quasi-steady state or slowly developing turbulent regimes. The approach has also been applied for unsteady Reynolds averaged Navier-Stokes (URANS) simulation [14]. Temporally developing direct numerical simulation (T-DNS) also do not require additional numerical approximations unlike the spatially developing and non-developing approaches. However, to ensure their predictive accuracy, particularly for bypass transition flows that involves regimes with variable growth and decay gradients, certain numerical issues need to be investigated further.

Currently available general-purpose transition sensitive RANS turbulence models can be loosely classified as either correlation-based [15] or physics-based [16]. Correlation-based models typically solve for an intermittency transport equation, which is the fraction of time the flow is turbulent during the transition phase and is used as a turbulent eddy viscosity multiplier. Several studies have reported that the intermittency distribution shows a universal behavior upon normalization [17]. The transition onset location is either specified explicitly based on empirical correlations or solved for using additional transport equations. These models rely directly on empirical correlations to specify model parameters.

Physics-based models [16] though still highly empirical in nature, aim for a more generalized approach wherein the evolution of turbulent fluctuations is predicted in the pre-transitional and transitional regions. Development of such models require: (1) a proper

understanding of turbulence production processes such as entrainment of freestream turbulence, development of fluctuations in the pre-transitional regions including turbulence damping (shear sheltering), boundary layer breakdown (turbulent spot formation), turbulent energy production dynamics, and overshoot of turbulent fluctuations in the post transition region; and (2) evaluation and/or identification of flow parameters that can be used as a marker for turbulence onset/growth in low-fidelity RANS simulations. Previously documented LES and DNS studies have helped in highlighting some of the underlying transitional flow physics [7,9,18] to address the above requirements. Studies agree that freestream disturbances induce low-frequency streamwise vortices or streaks in the pre-transitional region (referred to as Klebanoff modes), which lift from the wall causing ejection events. Transition occurs due to the formation of turbulent spots, which are associated with multiple head hairpin-type vortices with U- or Λ-shaped structures underneath them. However, the energy transfer pathway from freestream disturbances to pre-transitional (non-turbulent) fluctuations to turbulent fluctuations remains somewhat unclear.

Walters et al. [16,19] developed a physics based model building on the physics of Klebanoff mode growth identified in LES/DNS studies, as discussed above. In this model, the growth of the pressure-strain was assumed to correspond to the energy transfer during transition from pre-transitional fluctuations (Klebanoff modes) to boundary layer turbulence. It was approximated that the transition occurs when the ratio of molecular diffusion time-scale ($T_{d,W}$) to pressure-strain time-scale ($T_{r,W}$) increases to a critical value. The critical time-scale ratio used in the model was calibrated using numerical simulations of flat-plate and turbine cascade test cases.

Mayle and Schultz [20] identified the pressure-diffusion terms as the driver of the growth of Klebanoff modes from freestream disturbance, and pressure-strain terms as the driver of the energy redistribution from the Klebanoff modes to the other components. The latter is also

supported by Lardeau et al. [21], wherein it was indicated that unlike the fully developed turbulent region, the pressure-strain terms are negligible in the pre-transition regime. Walters et al. [19] hypothesized that the absence of the pressure-strain inhibits nonlinear turbulence breakdown, and is closely related to shear-sheltering, as proposed by Jacobs and Durbin [6,22].

Evaluation/identification of a relevant marker for transition onset location is an open question. Ideally, for use in transition-sensitive RANS models, a marker could be identified based solely on local statistical flow variables available in a RANS simulation. Several studies have reported peak streamwise velocity fluctuations u'/U_∞ as a transition onset marker, where U_∞ is the free-stream mean velocity [23–25]. Praisner and Clark [17] identified that transition onset occurs when the ratio of laminar diffusion time-scale ($T_{d,PC}$) to local, energy-bearing turbulent fluctuation time-scale (T_r) reaches a critical value. The time-scale was found to be nearly constant over a wide range of flow field conditions.

Our current hypothesis for development of pre-transitional fluctuations in the developing boundary layer focuses on the suppression of the "return-to-isotropy" (i.e. slow) pressure-strain terms in the Reynolds stress transport equations so that they have no significant impact on the production dynamics. This is consistent with results in the literature that show these terms to be near zero.

The goal then is to find a physically meaningful transition onset marker to determine when the breakdown to 3D turbulence begins. Our supposition is that this corresponds to the sudden growth in magnitude of the pressure-strain terms. Furthermore, since transition is known to be an inherently nonlinear process, it is assumed that it is the slow pressure strain terms that are responsible for the transition onset (breakdown to 3D turbulence). Since these terms are known to redistribute energy from highly energetic components to lower energetic components (i.e. "return-

to-isotropy") this makes sense conceptually. The physics-based transition marker, thus, should be related to the slow pressure strain terms in a meaningful way.

1.2 OBJECTIVES AND APPROACH

The overall objective of this study is to develop a physics-based transition onset marker (**end goal**), and analysis/evaluation of its potential efficacy in RANS simulations of transitional and turbulent flow (**future work**). To achieve this, temporally developing DNS (T-DNS) are performed using a pseudo-spectral solver for free-stream turbulence induced bypass transition flow over a flat-plate under zero, favorable, and adverse pressure gradients. First part of the research focuses on validation of T-DNS as a viable numerical approach for bypass transition simulations. Next, characteristics/criteria for a viable transition onset marker are established and several large-scale flow parameters are investigated based on heuristic premises as potential transition onset markers. Finally, the role of pressure-strain correlation specifically the return and rapid terms in transition onset are evaluated and the acquired phenomenological reasoning is used to develop a physics-based transition onset criterion. The key tasks performed in this research are elaborated below.

Task #I: Validate T-DNS as a viable approach for bypass transition flows. This task involves the following sub-tasks.

Subtask I.1: Demonstrate the capability of T-DNS to accurately predict both the growth/decay of boundary layer and decay of free-stream turbulence simultaneously.

Subtask I.2: Prediction errors for the temporal momentum integral boundary layer equation and boundary layer parameters are assessed to estimate the optimal domain size required for T-DNS.

Subtask I.3: Develop a formulation for the domain translation velocity and compare directly with spatial DNS results.

Subtask I.4: Improve the T-DNS results validation for flat-plate boundary layer bypass transition.

Subtasks I.1 and I.2 will perform T-DNS for flat plate boundary layer (FPBL) under zero pressure gradient on five different domain lengths $L = 20\delta_0, 5\delta_0, 30\delta_0, 40\delta_0$, and $50\delta_0$ for $Tu_{in} = 3.5\%$, where δ_0 is the initial boundary layer thickness and validate it against spatial-DNS [6] and experimental data [26]. Grid resolutions of 192×193×192 and 256×257×256 (finer grid) cells along x, y, and z directions, respectively were used.

Subtasks I.3 will perform T-DNS using three different time step sizes $\Delta t = 3.33\times10^{-4}$, 5×10^{-4}, and $7.5\times10^{-4} L/U_0$, where U_0 is the free-stream velocity, on $L = 20\delta_0$ for $Tu_{in} = 3.5\%$.

Subtask I.4 will perform window averaging of the second and higher order statistics for improved validation of the T-DNS results for flat-plate boundary layer bypass transition and publish the results from Task #1 in a peer-reviewed journal (Physics of Fluids).

Task #II: Identify large scale parameters and develop criteria for their viability to be used as a transition onset marker. This task involves the following sub-tasks.

Subtask II.1: Develop criteria for a large-scale parameter for use as a viable transition onset marker. Identity/study various large parameters on heuristic premises for use as a transition onset marker.

Subtask II.2: Publish the results from Task #II in a peer-reviewed journal.

Subtask II.1 will performs T-DNS for channel flow at $Re_\tau = 180$ ($Re_H = 3300$) and 590 ($Re_H = 12656$), and a flat-plate boundary layer flow under zero pressure gradient (FP), with different initial $Tu_{in} = 1 - 5\%$.

Task #III: Evaluate the role of pressure-strain terms in transition onset and use the acquired phenomenogical reasoning to develop a physics-based transition onset criterion. This task involves the following sub-tasks.

Subtask III.1: Study the evolution of all the three components of pressure strain in the pre-transitional boundary layer.

Subtask III.2: Determine the relation between the evolution of the slow part of the pressure strain correlation and transition onset location in the flow.

Subtask III.3: Determine the role of the source terms in the pressure Poisson equation if they can act as effective surrogates for the pressure strain terms themselves.

Subtask III.4: Develop a large-scale transition onset marker terms based on simple scaling arguments for use in URANS simulations.

Subtasks III.1 though II.4 will perform T-DNS for FPBL under zero, adverse, and favorable pressure gradient on the domain size of $L = 40\delta_0$ for $Tu_{in} = 1 - 7\%$ with a grid resolution of 256×257×256. The evolution of the rapid, slow, and stokes components of the pressure strain correlation will be analyzed.

CHAPTER II

LITERATURE REVIEW

2.1 TRANSITION MODELS

Transition from laminar to turbulent flow is important in many engineering applications, including aerospace, automotive, biomedical, heating and cooling, power generation, marine systems and chemical processing[1]. Transition in attached boundary layers is typically categorized as either natural or bypass. Engineering applications often involve bypass transition, which occurs due to the presence of strong disturbances (high free-stream turbulence, large wall roughness elements, flow separation, pressure gradient effects etc.) [18,27]. Among all the factors, free stream turbulence intensity and pressure gradient are usually considered the two most important parameters for engineering systems. Hence, models are usually calibrated/validated to account for these effects [28–30]. A review of the literature shows that available transition models are applied either as standalone transition correlation[42-44] or integrated into the turbulence models themselves[6-8,45-51].

2.1.1 EMPIRICAL MODELS

Empirical correlations are usually developed from statistical analysis of experimental data for simplified geometries, and therefore often lack universality. In addition, they are difficult to implement for complex configurations, as determination of relevant geometrical parameters (e.g. streamwise dimension x), or integral quantities (e.g. momentum thickness θ) can be difficult in general-purpose solvers. Transition-sensitive turbulence models provide the

potential for more universal applicability and can be loosely classified as either correlation-based[45-48] or physics-based[6-8,49-50]. Correlation-based models typically solve for an intermittency (γ) transport equation, which is the fraction of time flow is expected to be turbulent and is used as a turbulent eddy viscosity multiplier. The transition onset location is either specified explicitly based on empirical correlations[45-47] or solved using an additional transport equation[48]. One of the most successful correlation-based models is Menter et al.[48,52,53] $\gamma - \widetilde{Re}_{\theta t}$ model. This model requires solution of two transport equations, one for γ and other for $\widetilde{Re}_{\theta t}$. One of the critical inputs to this model is $Re_{\theta T}$, which is transition onset location parameter, and is provided as an empirical correlation estimated based on relevant experimental datasets.

2.1.2 PHYSICS BASED-MODELS

Physics-based models[6-8] use a more generalized approach for predicting the evolution of turbulent fluctuations in the pre-transitional and transitional regions. The model solves an additional transport equation for laminar kinetic energy, k_L along with turbulent kinetic energy k_T as below:

$$\underbrace{\frac{D}{Dt}\rho k_L}_{\text{Advection}} = \underbrace{P_{kL}}_{\text{Production}} - \underbrace{R_{BP} + R_{NAT}}_{\text{Transition rate}} - \underbrace{D_L}_{\text{Destruction}} + \underbrace{\frac{\partial}{\partial x_j}\left[\nu \frac{\partial k_L}{\partial x_j}\right]}_{\text{Diffusion}} \tag{2.1}$$

$$\underbrace{\frac{D}{Dt}\rho k_T}_{\text{Advection}} = \underbrace{P_{kt}}_{\text{Production}} + \underbrace{R_{BP} + R_{NAT}}_{\text{Transition rate}} - \underbrace{\omega k_T}_{\text{Dissipation}} - \underbrace{D_T}_{\text{Destruction}} + \underbrace{\frac{\partial}{\partial x_j}\left[\left(\nu + \frac{\alpha_T}{\sigma_k}\right)\frac{\partial k_T}{\partial x_j}\right]}_{\text{Diffusion}} \tag{2.2}$$

The key aspects of the above model are: (a) generation of pre-transitional fluctuation modes as laminar kinetic energy production P_{kL}; and (b) transfer of energy from pre-transitional ("laminar") modes to turbulent velocity fluctuations via the transition rate terms R_{BP} (for bypass

transition) and R_{NAT} (for natural transition). As expected, these terms appear as a sink in the k_L equation and as a source in the k_T equation. The modeling of production P_{kL} and evaluation of associated coefficients requires understanding of the development of fluctuations in the pre-transitional regions including turbulence damping (shear sheltering), and correlation of pre-transitional fluctuation growth with free stream low-frequency wall-normal turbulent fluctuations. These aspects of flow physics are fairly well understood[8]. The R_{BP} term is expected to be triggered at transition onset, which requires specification of a transition onset parameter and threshold value. In the absence of proper understanding of boundary layer breakdown mechanisms and availability of a universal onset marker, the model relies on empirical correlations for transition onset similar to the $\gamma - \widetilde{Re}_{\theta t}$ model. The empirical correlations work very well for simple cases, but caution must be exercised when they are extended to more complex flow conditions.

2.2 TKE AND STRESS BUDGET

The stress budget terms are computed as:

$$\frac{\partial \tau_{ik}}{\partial t} + \underbrace{\overline{u_j}\frac{\partial \tau_{ik}}{\partial x_j}}_{C} = \underbrace{-\left(\tau_{kj}\frac{\partial \overline{u_\iota}}{\partial x_j} + \tau_{ij}\frac{\partial \overline{u_k}}{\partial x_j}\right)}_{P} + \underbrace{\overline{\frac{p'}{\rho}\left(\frac{\partial u_k'}{\partial x_\iota} + \frac{\partial u_\iota'}{\partial x_k}\right)}}_{Q} - \underbrace{\frac{\partial\left(u_i'u_j'u_k'\right)}{\partial x_j}}_{PT} - \underbrace{\frac{1}{\rho}\frac{\partial\left(p'u_k'\delta_{ij} + p'u_i'\delta_{kj}\right)}{\partial x_j}}_{T} + \underbrace{\nu\frac{\partial^2 \tau_{ik}}{\partial x_j \partial x_j}}_{D} - \underbrace{2\nu\overline{\frac{\partial u_i'}{\partial x_j}\frac{\partial u_k'}{\partial x_j}}}_{\varepsilon} \tag{2.3}$$

where, *C, P, Q, ε, D, T,* and *PT* represent the turbulent convection, turbulent production, pressure strain, viscous dissipation, viscous diffusion, turbulence diffusion, and the pressure transport terms respectively. Note that the averaged values in this study are obtained using averaging in the xz plane.

The trace of $Q_{ij} = \overline{\frac{p'}{\rho}\left(\frac{\partial u_k'}{\partial x_\iota} + \frac{\partial u_\iota'}{\partial x_k}\right)} = 0$ and consequently does not appear in the turbulent kinetic energy equation (TKE).

2.3 PRESSURE-STRAIN CORRELATION

The pressure-strain correlation, $Q_{ij} = \overline{\frac{p'}{\rho}\left(\frac{\partial u_k}{\partial x_\iota} + \frac{\partial u_\iota}{\partial x_k}\right)}$ serves to redistribute energy amongst the Reynolds stresses.

2.3.1 PRESSURE POISSON EQUATION

Some insight into the pressure-rate of strain tensor correlation can be gained by examining the Poisson equation for the fluctuating pressure. The governing equation for the pressure fluctuation is given as:

$$\underbrace{\frac{1}{\rho}\nabla^2 p'}_{\frac{1}{\rho}\nabla^2 p^{(r)} + \frac{1}{\rho}\nabla^2 p^{(s)}} = \underbrace{-2\frac{\partial u_j'}{\partial x_i}\frac{\partial \overline{U}_i}{\partial x_j}}_{Rapid\ Term} - \underbrace{\frac{\partial}{\partial x_i \partial x_j}\left(u_i u_j - \overline{u_i u_j}\right)}_{Slow/Return\ Term} \tag{2.4}$$

Therefore, the rapid and slow pressure are governed by the following equations:

$$\frac{1}{\rho}\nabla^2 p^{(r)} = -2\frac{\partial u_j}{\partial x_i}\frac{\partial \overline{U}_i}{\partial x_j} \tag{2.5}$$

And

$$\frac{1}{\rho}\nabla^2 p^{(s)} = -\frac{\partial}{\partial x_i \partial x_j}\left(u_i u_j - \overline{u_i u_j}\right) \tag{2.6}$$

Solve Eq.'s (2.5) and (2.6) to get the rapid and slow pressure

Harmonic/Stokes/Wall contribution to the pressure fluctuation does not have a source from Eq. (1) since it satisfies Laplace's equation exactly

$$\nabla^2 p^{(h)} = 0 \tag{2.7}$$

$p'$is determined from the DNS data for flat plate bypass transition

Since,

$$p' = p^{(r)} + p^{(s)} + p^{(h)} \tag{2.8}$$

From Eq. (2.8) $p^{(h)}$ can be determined

Corresponding to $p^{(r)}$, $p^{(s)}$, and $p^{(h)}$, the pressure-rate of strain tensor can also be decomposed into three contributions, $R_{ij}^{(r)}$, $R_{ij}^{(s)}$, and $R_{ij}^{(h)}$ with the following definitions

$$R_{ij}^{(r)} = \langle \frac{p^{(r)}}{\rho}\left(\frac{\partial u_i}{\partial x_j} + \frac{\partial u_j}{\partial x_i}\right)\rangle \tag{2.9}$$

$$R_{ij}^{(s)} = \langle \frac{p^{(s)}}{\rho}\left(\frac{\partial u_i}{\partial x_j} + \frac{\partial u_j}{\partial x_i}\right)\rangle \tag{2.10}$$

$$R_{ij}^{(h)} = \langle \frac{p^{(h)}}{\rho}\left(\frac{\partial u_i}{\partial x_j} + \frac{\partial u_j}{\partial x_i}\right)\rangle \tag{2.11}$$

2.4 TRANSITION ONSET MARKERS (STATE OF THE ART)

Mayle[31] proposed a correlation for the onset of steady bypass transition in attached boundary flow:

$$Re_\theta \geq Re_{\theta_t} = 400Tu^{-.625} \tag{2.12}$$

where, Re_{θ_t} is the critical value for start of transition.

The correlation of Abu-Ghannam and Shaw[32] for natural and bypass transition at low free-stream turbulence intensities is given as:

$$Re_{\theta t} = 163 + exp\left(F(\lambda_\theta) - \frac{F(\lambda_\theta)}{6.91}Tu\right) \tag{2.13}$$

with

$$F(\lambda_\theta) = \begin{cases} 6.91 + 12.75\lambda_\theta + 63.64\lambda_\theta^2, & for\ \lambda_\theta \leq 0 \\ 6.91 + 2.48\lambda_\theta - 12.27\lambda_\theta^2, & for\ \lambda_\theta \geq 0 \end{cases} \tag{2.14}$$

where, $\lambda_\theta = (\theta^2/\nu)(dU/ds)$ is the pressure-gradient parameter; dU/ds is the acceleration along the streamwise direction, determined at the edge of the boundary layer, $\frac{dU}{ds} = \frac{u}{U}.\frac{dU}{dx} + \frac{v}{U}.\frac{dU}{dy}$. For bypass transition in a flat-plate boundary layer under a zero-pressure gradient (ZPGFPBL), $\lambda_\theta = 0; F(\lambda_\theta)$=1.

Suzen and Huang[33] proposed a correlation for the onset of transition as:

$$Re_{\theta t} = \left(120 + 150Tu_{\infty,t}^{-2/3}\right)coth[4(0.3 - 10^5 K_t)] \tag{2.15}$$

where, $K_t = \left(\nu/U_{\infty,t}^2\right)(dU_\infty/dx)$ is the acceleration parameter closely related to the pressure gradient parameter. For ZPGFPBL, $K_t = 0$.

Lodefier et al's[15] correlation for the onset of steady bypass transition in attached boundary flow is based on the correlation of Mayle, given above and is given as:

$$Re_\theta \geq Re_{\theta_t} = 420Tu^{-.69} \tag{2.16}$$

The intermittency based transition model using only local variables by Menter and Langtry[34] uses the following transition onset criterion which even though was not disclosed in the original paper owing to proprietary information, but was later reconstructed by Suluksna et al.[35].

$$Re_{\theta t} = 803.72(Tu + 0.6067)^{-1.027} F(\lambda_\theta, K) \tag{2.17}$$

with

$$F(\lambda_\theta) = \begin{cases} 1 - \left[-10.32\lambda_\theta - 89.47\lambda_\theta^2 - 265.51\lambda_\theta^3\right] exp[-Tu/3.0], & for\ \lambda_\theta \leq 0 \\ 1 + [0.0962(K.10^6) + 0.148(K.10^6)^2 + 0.0141(K.10^6)^3] \\ (1 - exp[-Tu/1.5]) + 0.556[1 - exp(-23.9\lambda_\theta)]exp(-Tu/3.0), & for\ \lambda_\theta > 0 \end{cases} \tag{2.18}$$

and K is the acceleration parameter given as, $K = (\nu/U^2)(dU/ds)$.

The Langtry and Menter[36] further improved their transition model and proposed a correlation which is completely empirical and is currently the most widely used one currently for attached bypass and natural transition under the influence of free-stream turbulence:

$$Re_{\theta t} = \begin{cases} [1173.51 - 589.428Tu + 0.2196Tu^{-2}]F(\lambda_\theta), & for\ Tu \leq 1.3 \\ 331.50[Tu - 0.5658]^{-0.671} F(\lambda_\theta), & for\ Tu > 1.3 \end{cases} \tag{2.19}$$

with

$$F(\lambda_\theta) = \begin{cases} 1 - \left[-12.986\lambda_\theta - 123.66\lambda_\theta^2 - 405.689\lambda_\theta^3\right] exp\left[\left(\frac{Tu}{1.5}\right)^{1.5}\right], & for\ \lambda_\theta \leq 0 \\ 1 + 0.275[1 - exp(-35.0\lambda_\theta)] exp\left(-\frac{Tu}{0.5}\right), & for\ \lambda_\theta > 0 \end{cases} \quad (2.20)$$

Included are some limitations for numerical robustness:

$$-0.1 \leq \lambda_\theta \leq 0.1, Tu \geq 0.027, Re_{\theta t} \geq 20 \quad (2.21)$$

CHAPTER III

NUMERICAL METHOD AND SIMULATION SETUP

3.1 NUMERICAL METHOD

DNS requires solution of the Navier-Stokes (N-S) equations for incompressible flow:

$$div\, u = 0 \tag{3.1}$$

$$\frac{\partial u}{\partial t} + (u.\, grad)u = -\frac{1}{\rho} grad\, p + \nu div(grad(u)) \tag{3.2}$$

In a DNS of inhomogeneous turbulence, pseudo-spectral methods [37,38](developed by Orszag et al. (1972) and Rogallo (1981)) are the most preferred numerical approach because of the greater accuracy and ease of parallelization. The solution domain is a cube of L and the velocity field $u(\boldsymbol{x}, \boldsymbol{t})$ is represented as a series of finite Fourier modes.

$$u(\boldsymbol{x}, \boldsymbol{t}) = \sum_{\kappa} e^{ik.x} \hat{u}(\boldsymbol{\kappa}, \boldsymbol{t}) \tag{3.3}$$

A total of N^3 wavenumbers are represented, where N is an even number which determines the size of the simulation. The lowest non-zero wave number and the largest wave number in each direction are represented as:

$$\kappa_0 = \frac{2\pi}{L}$$
$$\kappa_{max} = \frac{1}{2} N\kappa_0 = \frac{\pi N}{L} \tag{3.4}$$

The N^3 wavenumbers represented are

$$\boldsymbol{\kappa} = \kappa_0 \boldsymbol{n} = \kappa_0 (e_1 n_1 + e_2 n_2 + e_3 n_3) \tag{3.5}$$

The discrete Fourier transform gives a one-to-one mapping between the velocities in physical space $u(\boldsymbol{x}, \boldsymbol{t})$ and the Fourier modes $\hat{u}(\boldsymbol{\kappa}, \boldsymbol{t})$. In pseudo-spectral approach the non-linear terms in the N-S equations are evaluated in a different manner. The velocity field is transformed into physical spaces for calculation of the non-linear terms ($u_i u_j$) which are then transformed back into wavenumber spaces. This avoids the summing of the triad interactions in the N-S equation in wavenumber space. Hence, the pseudo-spectral method requires an order of $N^3 logN$ operations instead of N^6.

The spectral methods involve advancing the Fourier modes in small time steps Δt according to the N-S equations in wavenumber space. The main numerical/computational issues as such involving pseudo-spectral methods are the time-stepping approach, minimizing aliasing errors, and parallelization of the algorithm. Applying DNS to a developing boundary layer requires non-Fourier representation in the direction of inhomogeneity.

The incompressible N-S equations (Eq. 3.1 and 3.2) were discretized using FFT along the streamwise (x) and spanwise (z) directions, and Chebyshev polynomials in the wall normal (y) direction. The discretized equations were solved using a three-step fractional step method. Refer

to Bhushan et al. for more details [39]. The first step marches the convective term using the third-order Adams Bashforth method,

$$u^{(1)} = u^{(N)} - \delta t\left[\frac{23}{12}\left(u^{(N)}.grad\right)u^{(N)} - \frac{16}{12}\left(u^{(N-1)}.grad\right)u^{(N-1)} + \frac{5}{12}\left(u^{(N+1)}.grad\right)u^{(N+1)}\right] \tag{3.6}$$

The second step is the pressure correction step which enforces incompressibility. The equations solved in this step are:

$$\begin{aligned} u^{(2)} &= u^{(1)} - \frac{\delta t}{\rho} grad\ p \\ divu^{(2)} &= 0 \end{aligned} \tag{3.7}$$

Taking the Fourier transform along x and z for a variable φ, the transform is defined as:

$$\mathcal{F}_x\mathcal{F}_z[\varphi(x,y,z)] = \acute{\varphi}(\kappa_x, y, \kappa_z) \tag{3.8}$$

Eq. 3.7 in wavenumber space κ_x, y, κ_z reduces to the following four sub-steps (Solve for $\grave{u}_2{}^{(2)}$, solve the pressure-Poisson equation to get $\grave{p}$, solve for $\grave{u}_1{}^{(2)}$, and $\grave{u}_3{}^{(2)}$:

$$\begin{aligned} \frac{\partial^2 \grave{u}_2{}^{(2)}}{\partial {x_2}^2} - (\kappa_x^2 + \kappa_z^2)\grave{u}_2{}^{(2)} &= -(\kappa_x^2 + \kappa_z^2)\grave{u}_2{}^{(1)} - i\left[\kappa_x \frac{\partial \grave{u}_1{}^{(1)}}{\partial x_2} + \kappa_z \frac{\partial \grave{u}_3{}^{(1)}}{\partial x_2}\right] \\ \frac{\delta t}{\rho}\grave{p} &= -\frac{1}{\kappa_x^2 + \kappa_z^2}\left[i\kappa_x \grave{u}_1{}^{(1)} + i\kappa_z \grave{u}_3{}^{(1)} + \frac{\partial \grave{u}_2{}^{(1)}}{\partial x_2}\right] \\ \grave{u}_1{}^{(2)} &= \grave{u}_1{}^{(1)} - i\kappa_x\left(\frac{\delta t}{\rho}\grave{p}\right) \\ \grave{u}_3{}^{(2)} &= \grave{u}_3{}^{(2)} - i\kappa_z\left(\frac{\delta t}{\rho}\grave{p}\right) \end{aligned} \tag{3.9}$$

The third step incorporates the viscous stresses; in wave number space it is represented as:

$$\frac{\delta t}{Re}\frac{\partial^2 \grave{u}_l^{(N+1)}}{\partial {x_2}^2} - \left[\frac{\delta t}{Re}\left(\kappa_x^2 + \kappa_y^2\right) + 1\right]\grave{u}_l^{(N+1)} = -\grave{u}_l^{(2)} \tag{3.10}$$

where, $l = 1,2,3$

The calculation of highlighted term in Eq. (3.6) involves convolution in the wave number space which is complicated to perform. Hence its computed in physical space using the 3/2 dealiasing rule, thereby the solver is called "pseudo-spectral." This procedure requires inverse FFT and FFT computations of 3 velocity and 6 derivative components to move data from wave number to physical space and back to wave number space for the calculation of the convective (or stress) terms. The FFT's are performed using FFTW subroutines version 3.3 (Frigo and Johnson, 2011) [40].

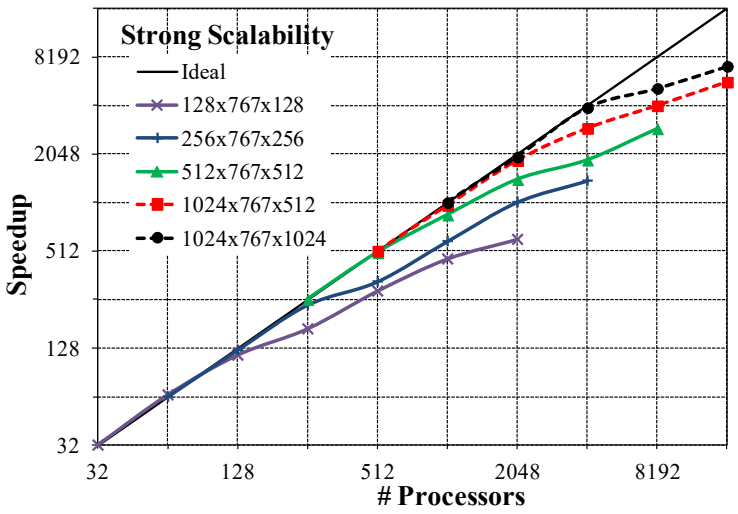

Figure 3.1 Strong scalability of parallel pseudo-spectral solver, ParaSpectra. Scalability study was performed on Oakridge National Lab HPC system, Titan.

3.2 PARALLEL PSEUDO-SPECTRAL SOLVER (PARSPECTRA)

The DNS simulations in this research will be performed using the parallel pseudo-spectral solver, *ParSpectra*, developed by Bhushan[41]. The high performance computing capability of the solver includes shared memory OpenMP thread parallelization for the FFT calculations using the FFTW multi-thread library [40] and message passing interface (MPI) parallelization along the x_2-direction using influence matrix method as discussed in [39].

The solver is parallelized using hybrid OpenMP/MPI approach to effectively utilize the distributed and shared memory across and within nodes of HPC systems. The solvers scale up to 16K processors on up to 1 billion grid points (Fig. 3.1). The solver has been extensively validated for LES of channel, mixing layer and jet flows [41–43], and recently for DNS of channel flow at $Re_\tau = 180$ and 590 [44], using Moser et al. DNS results[45].

3.2.1 NUMERICAL ERRORS AND CONVERGENCE STUDY

Temporal and spatial convergence of the solver was studied for simple 2D laminar flows. The test cases included: (1) simulation of traveling wave in a doubly periodic domain; and simulation of thick shear layer vortex roll-up in a (2) 2D doubly periodic and (3) streamwise periodic domains. 4) Test case of DNS of plane channel flow at $Re_\tau = 180$ and 590 was used to determine the effect of aliasing error on the simulations in order to determine the optimal dealiasing approach for DNS. The spatial accuracy of the solver for turbulent flow simulations as well as the scalability study and predictive capability was also undertaken using the plane channel flow simulations.

The solver shows second-order temporal accuracy, and spatial order of accuracy of 6.8 and 3.6 for 2D laminar and turbulent flow simulations, respectively. The solver displays reasonable scalability up to 8K processors on grids with 800M grid points, and it is estimated

that the best computational performance is achieved for simulations using 100–400Kgrid points per processor on systems with 2GB memory per processor. The mean and turbulent channel flow predictions, including higher order statistics and TKE and stress budgets, compare within 0.5% of the available benchmark results.

3.3 TEMPORAL DIRECT NUMERICAL SIMULATION (T-DNS)

3.3.1 FLAT PLATE BOUNDARY LAYER

The simulations were performed using a cubic domain $L_x = L_y = L_z = L$, where L is the domain length. Periodic boundary condition was used along the x and z directions. A no-slip boundary condition was used at the bottom wall $y = 0$, and a Neumann boundary condition was used at the top $y = L$ plane as below:

$$\frac{\partial u}{\partial y} = \frac{\partial w}{\partial y} = 0; \frac{\partial v}{\partial y} = -\left(\frac{\partial u}{\partial x} + \frac{\partial w}{\partial z}\right) \tag{3.11}$$

where, u is the streamwise velocity, v is the wall normal velocity, and w is the spanwise velocity.

As summarized in Table 1, four sets of simulations were performed. Set #1 included simulations for $Tu_{in} = 3.5\%, Re_{\ell_0} = 1476.7$, where Re_{ℓ_0} is the Reynolds number based on free-stream turbulence length scale ℓ_0, on five different cubic domains with lengths $L = 20\delta_0$, $25\delta_0, 30\delta_0, 40\delta_0$, and $50\delta_0$, where δ_0 is the initial boundary layer thickness. Set #2 included simulations for $Tu_{in} = 3.5\%, Re_{\ell_0} = 1476.7$ using three different time step sizes $\Delta t = 3.33\times10^{-4}$, 5×10^{-4}, and $7.5\times10^{-4}L/U_0$, where U_0 is the free-stream velocity, on $L = 20\delta_0$. Set #3 included simulations for $Tu_{in} = 6\%$ using two different free-stream turbulence length scales

$Re_{\ell_0} = 1476.7$ and $Re_{\ell_0} = 8817.2$. The simulations using smaller and larger length scales are performed on $L = 30\delta_0$ and $L = 60\delta_0$, respectively. Set #4 included simulations for three Tu_{in} = 1.4%, 2.1% and 2.8% with $Re_{\ell_0} = 1476.7$ on $L = 30\delta_0$. An additional simulation was performed using $Tu_{in} = 0.01\%$ to simulate the laminar regime, and to verify the applicability of the domain translation velocity formulation for laminar flows.

The simulations for sets #1, 2 and 3 (i.e., for $Tu_{in} = 3.5\%$) were performed using initial mean flow conditions (i.e., streamwise velocity profile) obtained from the Blasius solution at $Re_{\delta 0} = 790.2$, $Re_{\theta 0} = 106$ or $Re_{x0} = 2.55\times10^4$. This resulted in free-stream turbulence length scale and initial boundary layer thickness ratio $\ell_0/\delta_0 = 1.85$. These initial conditions are same as the inflow conditions used by Jacob and Durbin S-DNS [6] (referred to as JD) for validation against T3A experiments [26] (Table 1). The flow conditions are also consistent with those of Nagarajan et al. [46] (referred to as NLF) S-DNS including leading-edge, wherein simulations were performed using $Tu_{in} = 3.5\%$ and 4.5% and $Re_{\ell_0} = 1476.7$ (Table 1). The smallest and largest domain sizes used herein corresponds to L/ℓ_0= 11 and L/ℓ_0= 27, respectively. Since $L/\ell_0 > 10$, the domain sizes are expected to be sufficiently large to accurately capture evolution of the isotropic free-stream turbulence.

The simulations for set #3 were performed using initial mean flow conditions corresponding to $Re_{\delta 0} = 384$, $Re_{\theta 0} = 51$ or $Re_{x0} = 5900$. The initial mean flow conditions were same as the inflow conditions used by S-DNS (JD) for validation against T3B experiments [26]. But differ in the Tu_{in} and Re_{ℓ_0} specification. S-DNS (JD) used $Tu_{in} = 7\%$ and $Re_{\ell_0} =$ 633.7 based on their estimates of the free-stream turbulence decay in the T3B experiments. However, their S-DNS predictions showed higher skin friction coefficients than Blasius solutions

(and experiments) in the pre-transition regime. It was reported that this could be possibly due to the use of smaller free-stream turbulence length scale and larger inlet intensity. Ovchinnikov et al. [47] (referred to OCP) estimated $Re_{\ell_0} = 8817.2$ in T3B experiments (Table 1), which is more than an order of magnitude larger than the estimates of JD. OCP performed S-DNS including leading-edge effects using $Tu_{in} = 6\%$ and $Re_{\ell_0} = 1448.6$ and $Re_{\ell_0} = 8817.2$ for validation against T3B experiments, where the smaller Re_{ℓ_0} corresponds to the values estimated for T3A experiments. Herein, the free-stream turbulence conditions are adopted based on the OCP study. Based on the initial conditions, the small turbulent length scale simulation involved $\ell_0/\delta_0 = 3.77$ and $L/\ell_0 \sim 8$. However, the large turbulent length scale simulation involved $\ell_0/\delta_0 = 23$ and $L/\ell_0 \sim 2.6$. OCP used a spanwise and wall normal domain size of $\sim 10\ell_0$ and $\sim 5\ell_0$ for small and large turbulent length scale cases, respectively. The domain size used for small ℓ_0 case seems reasonable, but the domain size is probably too restrictive for the evolution of the large ℓ_0 turbulence.

The boundary layer predictions for set #1 simulations are compared with S-DNS and experimental data in the boundary layer coordinates, i.e., with respect to Re_θ, to validate T-DNS results. In addition, the prediction errors for the temporal momentum integral boundary layer equation and boundary layer parameters are assessed to estimate an optimal domain size required for T-DNS. Simulations in set #1 and #2 are used to develop and validate a formulation for the domain translation velocity. To validate the V_D formulation, the T-DNS boundary layer and free-stream decay predictions are compared with S-DNS and experimental data in plate coordinates, i.e., with respect to Re_x. The boundary layer predictions for a range of Tu_{in} in set #3 are compared with analytic profiles to demonstrate the robustness of V_D formulation and T-DNS predictions.

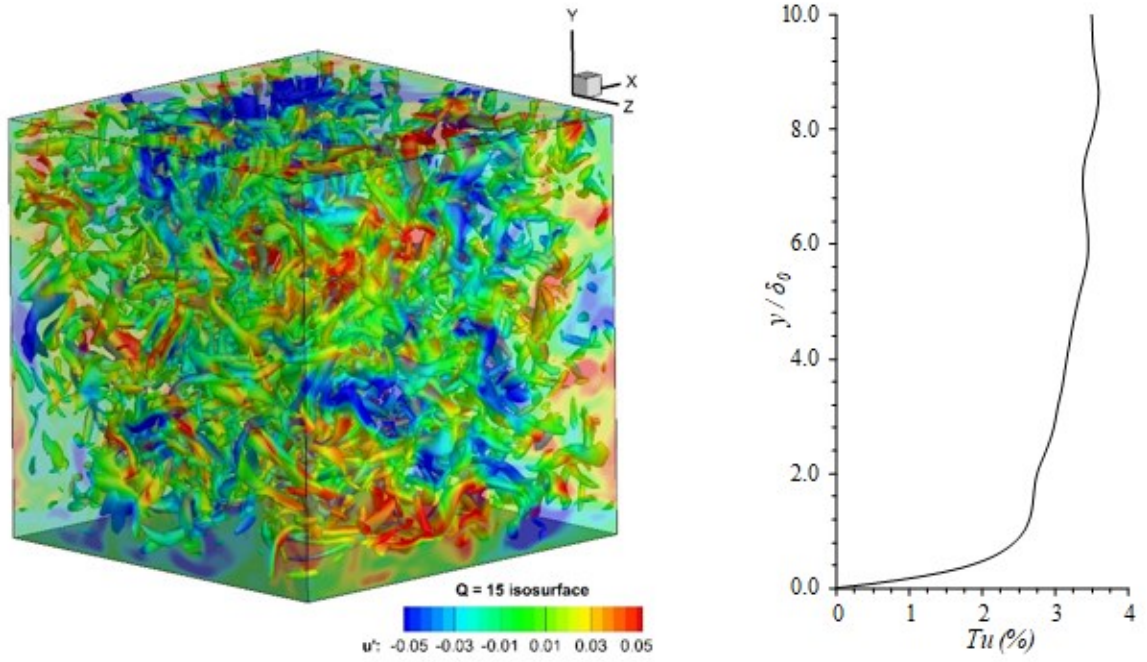

(a) (b)

Figure 3.2 (a) Turbulence structures in the initial condition are shown using isosurfaces of $\lambda_2 = -2$ colored with u'. (b) Variation of Tu with wall distance y/δ_0 for $Tu_{in} = 3.5\%$.

Table 3.1 Summary of numerical simulations performed in the study, including details of the domain size, grid and temporal resolutions, and simulation objectives.

Case		Tu_{in}	Domain Size ($L_x \times L_y \times L_z$)	Grid Resolution ($N_x \times N_y \times N_z$)	Grid spacing[iii]			$\Delta t \times U_0/L$ ($\times 10^{-4}$)	Δt^+ ($\times 10^{-2}$)	Objectives
					$\Delta x^+/\Delta z^+$	Δy^+_{min} ($\times 10^{-2}$)	Δy^+_{max}			
1	a	3.5%	$20\delta_0 \times 20\delta_0 \times 20\delta_0$	192×193×192	4.0	1.7	7.9	5	1.8	• Validation of T-DNS predictions in boundary layer coordinates using S-DNS[5,6] and experimental data[21]. • Estimation of errors due to streamwise correlation and boundary layer growth. • Evaluation of optimal domain size for T-DNS. • Development and validation of V_D formulation, including validation of T-DNS predictions in plate coordinates.
	b		$25\delta_0 \times 25\delta_0 \times 25\delta_0$		4.8	2.1	9.6		2.1	
	c		$30\delta_0 \times 30\delta_0 \times 30\delta_0$	192×193×192	5.9	2.5	11.5		2.5	
	d			256×257×256	4.5	1.4	8.8			
	e		$40\delta_0 \times 40\delta_0 \times 40\delta_0$	192×193×192	8.0	3.4	16.0		3.5	
	f			256×257×256	5.9	1.7	11.7			
	g		$50\delta_0 \times 50\delta_0 \times 50\delta_0$	192×193×192	10	4.2	19.5		4.3	
2	a	3.5%	$20\delta_0 \times 20\delta_0 \times 20\delta_0$	192×193×192	4.0	1.7	7.9	3.33	1.2	• Assessment of the effect of domain acceleration on domain translation.
	b[i]							5	1.8	
	c							7.5	2.6	
3	a[ii]	3.5%	$30\delta_0 \times 30\delta_0 \times 30\delta_0$	192×193×192	5.9	2.5	11.5	5	2.5	• Demonstrate the robustness of the T-DNS predictions and V_D formulation for a range of Tu_{in}.
	b	2.8%								
	c	2.1%								
	d	1.4%								
	e	0.01%								

[i]Same as case 1(a).
[ii]Same as case 1(c).
[iii]The values in the wall units are estimated using averaged C_f in the turbulent region and the same value is used for all the cases

Table 3.2 Summary of: domains, grids, and turbulence intensities used in the simulations; transformation factors used for the conversion of the predictions from temporal to spatial coordinates, and critical value of the large-scale transition onset parameters.

Case #	Flow	Domain $L_x \times L_y \times L_z$	Grid	Grid Resolution	Time step size		Tu_{in}	Transformation factors	Transition onset parameter critical value						
					Δt	Δt^+			u'/U_∞%	u_{2D}'/U_∞%	u'/u_τ	u_{2D}'/u_τ	$k/\nu\omega$	$k_{2D}/\nu\omega$	$\sqrt{k}y/\nu$
1	Channel (Re180) Re_τ=180 (Re_H = 3300)	$4\pi \times 2 \times 4\pi/3$	128×129 ×128	Δx^+=17.7;Δz^+=5.9; Δy^+_{min}=0.06;Δy^+_{max}=4.5	0.001 H/U_{c0}	0.01	1%	$Re_{x0} = 10000$ $Re_{\theta 0} = 67$ $V_D = 0.5$	15.3	2.4	4.87	0.75	70.1	14.3	130
2							2.5 %		15.4	3.2	4.54	0.95	80.7	17.3	147.7
3							5%		11.3	4.3	3.35	1.29	55.1	18	110.7
4	Channel (Re590) Re_τ=590 (Re_H=12656)	$2\pi \times 2 \times \pi$	384×257 ×256	Δx^+=9.7;Δz^+=7.2; Δy^+_{min}=0.1;Δy^+_{max}=7.2	0.00025 H/U_{c0}	0.007	1%	$Re_{x0} = 25000$ $Re_{\theta 0} = 104$ $V_D = 0.75$	16.5	2.3	8.33	1.07	135	26.7	166
5							2%		13.5	3.1	4.29	1.24	109	20.3	134.9
6							3%		12.9	3.5	4.27	1.26	102.1	21.6	160.2
7							5%		12.3	4.8	4.2	1.4	115.1	22.8	163.8
8		$4\pi \times 2 \times \pi$	512×257 ×256	Δx^+=14.5;Δz^+=7.2; Δy^+_{min}=0.1;Δy^+_{max}=7.2			2%		13.5	3.1	4.29	1.24	109	20.3	140.6
9	Flat-plate at zero pressure gradient (FP)	$30\delta_0 \times 30\delta_0 \times 30\delta_0$	192×193 ×192	Δx^+=6.2;Δz^+=6.2; Δy^+_{min}=0.03;y^+_{max}=12.4	0.015 δ_0/U_∞	0.03	2.1 %	$Re_{x0} = 25500$ $Re_{\theta 0} = 106$ $V_D = 0.5$	14.8	2.9	5.07	0.8	145.3	23.5	181.6
10							2.8 %		15.4	2.4	4.7	0.72	147.7	16.8	144.3
11							3.5 %		15.2	3.3	4.31	0.83	135.7	20.4	142.9
Average ± Standard deviation									14.3±12 %	3.2±26%	4.8±28 %	1±25%	110±30 %	20±18 %	148±17 %
Average ± Standard deviation without channel at Re_τ=180									14.4±11 %	3.1±27%	5±30%	1±27%	127±14 %	22±14 %	156±10 %

3.3.2 CHANNEL FLOW

For channel flow cases, Reynolds number Re_τ is defined based on mean friction velocity $u_{\tau 0} = \sqrt{\tau_{w0}/\rho}$ in the fully developed turbulence region, where τ_{w0} is the mean wall shear stress and ρ is density. Re_H is defined based on initial centerline velocity U_{c0} and half channel height H. As summarized in Table 3.2, channel flow Re180 simulations (i.e. $Re_\tau = 180$) are performed for $Tu_{in} = 1\%$, 2.5% and 5% (cases 1-3), channel flow Re590 simulations are performed for $Tu_{in} = 1\%$, 2%, 3% and 5% (cases 4-8), and the flat plate (FP) simulations are performed for $Tu_{in} = 2.1\%$, 2.8% and 3.5% (cases 9-11). In the channel flow simulations, a body force term f_x is applied in the x-direction to balance the momentum loss via wall friction expected in the fully developed turbulent region, i.e., $f_x = \tau_{w0}/\rho$.

The domain size and grid resolution used for Re180 is identical to the DNS study of Moser et. al. [11] (M-DNS). The Re590 domain size is also equivalent to M-DNS, except for case #8, for which the streamwise domain extent (L_x) is 2 times larger. The grid resolutions for case #8 are therefore coarser than M-DNS but are close to satisfying the DNS grid spacing requirements, $\Delta x^+ \leq 12$ and $\Delta z^+ \leq 6$ Case #8 is performed using a larger domain to investigate the effect of streamwise periodic boundary conditions on the pre-transitional flow.

The channel flow simulations are started with a fully developed mean turbulent velocity profile, expected for the flow, superimposed with turbulence fluctuations. Fig. 3.2 shows the converged initial turbulence and Tu_{in} variation along the wall normal direction for Re590, $Tu_{in} = 2\%$.

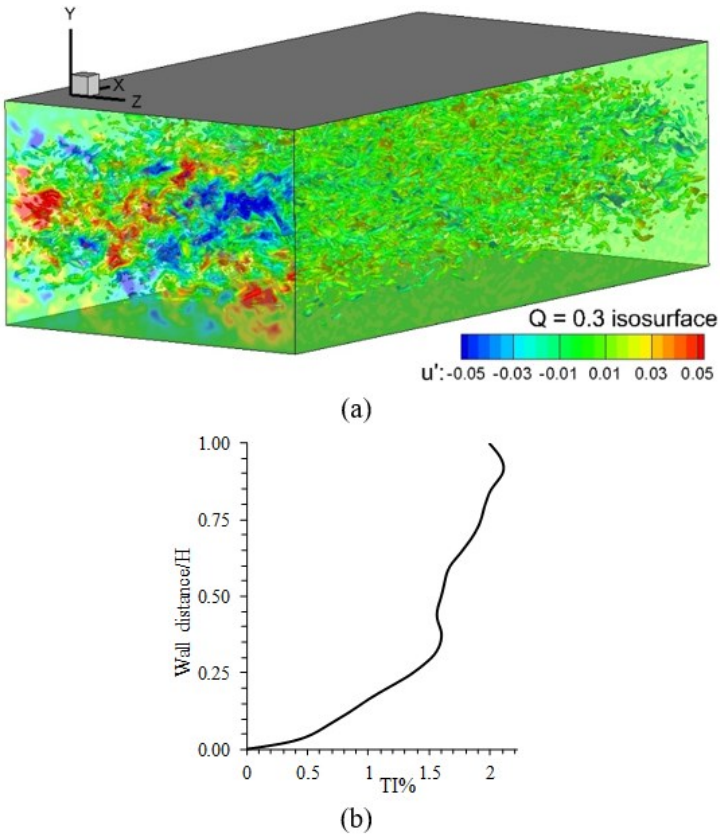

Figure 3.3 Initial turbulence for $Re_\tau = 590$, $Tu_{in} = 2\%$ simulation is shown using: (a) isosurface of $Q = 0.3$, colored using streamwise velocity fluctuation (u'), and (b) variation of planar-averaged Tu_{in} with wall distance.

Bhushan et al. [48] provides detailed validation of the channel flow simulations in the fully developed turbulent region using M-DNS, and Muthu and Bhushan [49] provides detailed validation of the FP transition flow predictions using JD-DNS and experimental data [50]. Therefore, only key validation results are presented herein. The discussion below first focuses on analysis of transient flow in the channel to evaluate similarities with FP bypass transition, followed by an analysis of large scale turbulence structures in the channel and FP simulations to identify appropriate potential transition onset markers for use in RANS modeling.

CHAPTER IV

VALIDATION OF TEMPORAL DIRECT NUMERICAL SIMULATION FOR FLAT-PLATE BOUNDARY LAYER BYPASS TRANSITION

Bypass transition from laminar to turbulent flow conditions is important in many engineering applications and impacts important flow quantities such as drag or heat transfer. It entails strongly nonlinear phenomena and involves the rapid amplification of perturbations within the boundary layer, which can be attributed to various external factors such as high free-stream-turbulence, large wall roughness elements, flow separation, pressure gradient effects etc.[51]. A review of the literature shows that its modeling in general is not mature enough to accurately predict flow behavior over a wide range of complex geometries and flow conditions[52]. Direct numerical simulation (DNS) of canonical flows such as flat-plate boundary layers are very useful in understanding the transition flow physics. DNS have typically been performed for spatially developing flat-plate flows under a zero-pressure gradient[4,6,7,53,54,10,5,8,55]. However, these datasets are typically limited to moderate Reynolds number ($Re_x \sim 10^5$) and high free-stream turbulence intensity (Tu_{in}) $\geq$ 3% flows. This is primarily due to the significantly large streamwise domain size requirements for low Tu_{in}/large Re_x flows.

Temporally developing simulations are a computationally inexpensive alternative to the spatially developing approach as they are expected to require one to two orders of magnitude smaller domain size/grid resolution for high Re_x flows. They are started from an initial condition

and a periodic boundary condition is applied along the streamwise direction. It is expected that the domain moves along with the flow, and the solution at any instant is a realization of an infinitesimal section of the spatially developing flow as illustrated in Figure 1(a). Additionally, the temporal approach allows for straightforward application of the numerically accurate pseudo-spectral solvers, especially high-fidelity fast Fourier transforms (FFT) in the streamwise direction. The smaller streamwise domain size allows for smaller input/output file sizes but requires more frequent input/output when compared to the spatially developing approach. Temporal approach may also have limitations in estimating ensemble averaged quantities.

The temporal approach has been widely used for simulation of non-developing flows such as isotropic decaying turbulence[56] and plane channel flows[57,58]. For such flows, the mean flow is frozen and only the turbulent structures evolve, and the use of a periodic boundary condition in the streamwise direction is justified if the domain size is larger than the turbulence correlation length. Spalart[59] proposed numerical approximations to freeze the boundary layer growth at a specific momentum-thickness (θ) based Reynolds number Re_θ, and performed temporal simulations for flat plate boundary layers with zero pressure gradient at four stations between $Re_\theta = 225$ to 1410. Guarini et al.[60], Maeder at al.[61], and Ostoich et al.[62] extended the approach to study the supersonic boundary layer for three different Mach numbers with a fixed Re_θ. These studies assumed that the boundary layer grows very slowly (thus no numerical approximations were applied), and the turbulence was regarded as homogeneous in the streamwise direction. Note that non-developing flow simulations focus on the analysis of turbulent structures and a direct comparison with the spatial simulations (in terms of Re_x) is not required.

Researchers as early as 1980's have demonstrated that the temporal approach can provide reasonable predictions for various developing flows. For example, Wray and Hussaini[63] used the temporal approach to study the evolution of large-scale structures during natural transition, and reported good qualitative agreement with the spatially developing structures. Piomelli et al.[64] performed large eddy simulation (LES) to study stages of natural transition in a plane channel flow. Rogers et al.[65] compared the evolution of vortical structures in a mixing layer and determined them to be qualitatively and to an extent quantitatively similar to those predicted in spatially developing simulations. Akhavan et al.[66] performed LES to study the dynamics of subgrid-scale energy interactions in a planar turbulent jet. Note that the above studies focused on temporal analysis of the mean and turbulent structures and a direct comparison with the spatial simulations was not performed.

Recently, there has been a renewed interest in the temporal approach for developing flows, and efforts have been made to perform a direct comparison between temporal and spatial predictions. He and Seddighi[24] performed temporally developing DNS (T-DNS) of transient flow behavior in a channel, wherein flow accelerates from a Reynolds number based on friction velocity of $Re_\tau = 180$ to 420. Their results illustrated that the flow undergoes transition process similar to the bypass transition induced by free-stream-turbulence for a flat-plate boundary layer. Simulation time was translated to the streamwise distance (Re_x) along the boundary layer using a domain velocity V_D. The latter was determined by best-fitting the early response of the transient flow with the Blasius solution, which led to $V_D = 0.74U_b$. where U_b is the local bulk velocity. Turbulent statistics were obtained using a mixture of spatial averaging over the homogeneous flow directions and averaging over 10 repeated runs. T-DNS estimates of the skin friction coefficient, C_f and Re_θ against Re_x was compared with T3A[26] spatial experimental data for

bypass transition. Mathur et al.[67] extended the above study to perform LES and DNS to study the temporal acceleration of a turbulent channel flow from $Re_\tau = 180$ to 1200. The prediction of the C_f and Re_θ were compared with experimental data using $V_D = U_b$.

Bobke et al.[68] performed temporally developing LES to study the growth of a turbulent asymptotic suction boundary layer. They determined that the spanwise domain length was the critical domain parameter and the minimum required spanwise domain size to be twice the boundary-layer thickness (δ). The temporal predictions of δ and mean velocity profiles were compared to spatially developing results to estimate the domain velocity $V_D = 1.3U_0$, where U_0 is the free-stream velocity.

Kozul et al.[69] performed T-DNS to study the growth of turbulent flat-plate boundary layer induced by a moving plate. They estimated Re_x corresponding to their temporal simulations based on the temporal boundary layer equation and Cole's law of the turbulent boundary layer wake. They reported good agreement between the temporal and spatial approaches for C_f, mean and turbulent velocity profiles as well as scalar statistics. They used time-window averaging technique together with spatial averaging over the homogeneous flow directions to obtain smooth profiles of turbulent statistics. Zhang et al.[70] extended the above study for investigation of turbulent/ nonturbulent interfaces in a compressible boundary layer at Mach number 0.8 and 1.6. The research primarily focused on flow physics analysis and limited efforts were made for direct comparison between spatial and temporal results.

In summary, the temporal studies have focused primarily on the slowly developing turbulent region and validations have focused on the growth of boundary/shear layer, and their predictive capability has not been sufficiently challenged for flows with variable growth and

decay as expected in bypass transition flows. To ensure the accuracy of temporal approach for bypass transition flows the following computational issues need to be investigated:

1. Can the temporal simulations accurately predict both the growth of boundary layer and the decay of free-stream turbulence? This is critical since the transition onset is dictated by the interaction between free-stream turbulence and the boundary layer. Note that none of the temporally developing studies in the literature have validated the decay of free-stream turbulence together with boundary layer growth.
2. What is the appropriate domain size along the streamwise direction? This aspect eventually dictates the numerical expense of the approach and prediction error due to streamwise periodicity. The domain size should be large enough to ensure that the turbulent structures are de-correlated, and small enough such that the growth of boundary layer within the domain is negligible to justify the periodic boundary condition. Further note that the de-correlation length depends on the flow regime, e.g., near-wall structures in the pre-transition regime are more elongated than those in the turbulent regime[71]. Note that temporal studies in the literature have estimated appropriate domain size based on the de-correlation length of the turbulent structures and have not estimated the errors in the predictions due to the streamwise periodicity assumption.
3. How to estimate spatial translation of the domain from the simulation time for direct comparison with spatially developing simulations/experiments? Most studies in the literature have assumed/estimated the domain velocity in fully turbulent regime in terms of mean/free-stream velocities. Local mean velocity as an approximate estimate for the domain velocity is valid for frozen turbulence[72,73]. But several researchers have pointed out that for developing flows domain velocity is a function of wavenumber, distance from wall etc. Overall, a

formulation for the domain translation velocity that encompasses the laminar, transition, and turbulent regimes is not available.

The overarching objective of this research thus is to validate T-DNS as a viable approach for bypass transition flows by ascertaining to what extent the T-DNS approximates the spatial evolution of the flow while allowing for meaningful predictions of the mean and turbulent flow statistics. To achieve this, T-DNS are performed using a pseudo-spectral solver for free-stream turbulence induced flat-plate boundary layer bypass transition under zero-pressure gradient, and above three issues are investigated. Simulations are performed using different domain and time step sizes, grid resolutions, and free-stream turbulence intensities $Tu_{in} = 0.01\%\ to\ 3.5\%$. The predictions of the overall transition flows pattern and streak breakdown mechanisms are analyzed and qualitatively compared with available spatial DNS results[74]. The prediction errors for the temporal momentum integral boundary layer equations are estimated to obtain the optimal domain size for T-DNS. A formulation for the domain translation velocity is derived from the spatial momentum integral boundary layer equations. Finally, the predictions of mean and 2nd and higher order turbulent quantities and budgets are validated against spatially developing DNS (referred to as S-DNS henceforth)[6,10,75] for bypass transition, boundary layer flows as well as channel flow DNS[76] results and T3A[26] bypass transition experiments.

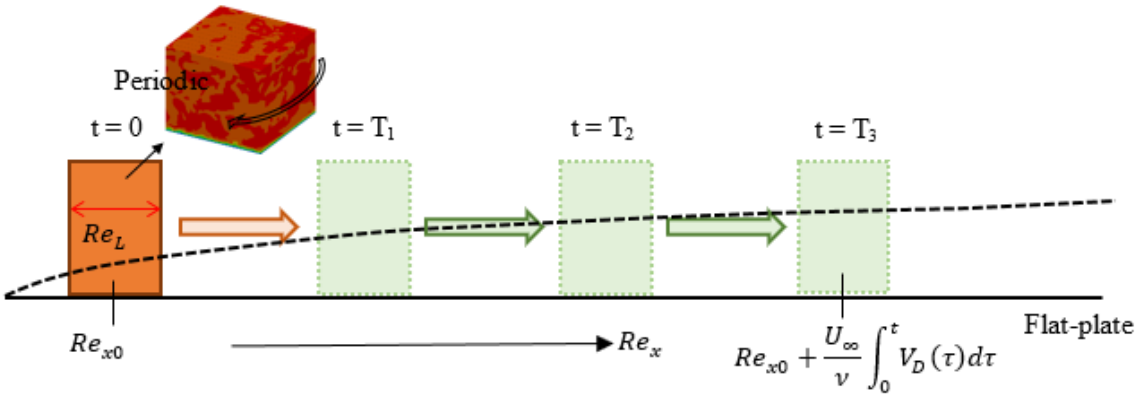

Figure 4.1 Schematic diagram demonstrating the translation of the domain with velocity V_D during a temporally developing simulation.

4.1 OVERALL FLOW STRUCTURES AND INSTABILITIES

Figure 4.2(a) shows the contours of instantaneous streamwise velocity, u/U_0 at the spanwise center plane $z = 0$ every 2000-time steps or $\Delta t = 1U_0/L$ side-by-side. The contours provide a visual inspection of the boundary layer growth. As evident, boundary layer grows steadily in the laminar regime. The growth is rapid in the transition regime, and the velocity in the near-wall region is higher than those in the laminar region due to the generation of turbulent fluctuations. The near-wall low velocity region in the turbulent regime is thinner than those in the laminar regime. This is expected as the former involves sharper near-wall gradients than the latter. The growth of the boundary layer agrees qualitatively well with those expected for flat-plate.

Figures 4.2(b) and 4.2(c) show contours of the streamwise and wall-normal velocity in the $x - z$ plane close to the wall at $y = 0.015$, respectively. Figure 2(d) shows the near-wall vortical structures using the second largest eigen value, λ_2, of the rate-of-strain tensor. Flow in the laminar regime shows alternate high- and low-speed longitudinal streaks aligned along the

streamwise direction. The spanwise spacing of the streaks are estimated to be around $1 - 1.2\delta$, where δ is the local boundary layer thickness. The streaks extend up to breakdown and are accompanied by counter-rotating longitudinal vortical structures. The u' for the longitudinal streaks increase with the progression and the peak u' is observed at $y \sim (0.3 - 0.35)\delta$ or $(0.9 - 1)\delta^*$ (shown in Fig. 6d), where δ^* is the local displacement thickness.

The streaks show initiation of breakdown in the pre-transition regime. Breakdown results in generation of vertical velocity and ejection of the streaks from the surface. The ejection events transfer energy from the near-wall region to outer region causing the growth of log-layer. This results in an isolated turbulent patch (or spot) within the laminar regime. The breakdown events quickly multiply in the transition regime and small-scale coherent structures start to form. Eventually the entire domain is filled with small-scale turbulent structures. The turbulent structures consist primarily of counter-rotating quasi-streamwise vortices and limited hair-pin structures. Counter rotating quasi-streamwise vortical structures are generated because of sinuous-like breakdown and hair-pin structures are generated because of varicose-like breakdown. The predominance of quasi-streamwise vortices over hair-pin structures suggest that the sinuous-like breakdown is more common than varicose-like breakdown.

Figures 4.3 and 4.4 provide an analysis of sinuous- and varicose-like breakdown, respectively. Subset figures (a) and (b) show 3D instantaneous vortical structures depicting the onset and progression of the vortical structures. Subset figures (c) and (d) show the flow pattern in $y - z$ planes depicting the interaction between the vortices. Results show that sinuous-like breakdown occurs as counter-rotating vortices are generated from either side of the low-speed streaks in a staggered pattern. Thus, when the streak is generated from one side ejects from the surface, i.e., v' is positive, the streaks from other side is almost at its peak location around

$y/\delta \sim 1$ and starts to come down, i.e., v' is negative. This results in antisymmetric positive and negative v' distribution. On the other hand, the distribution of spanwise fluctuating velocity, w' is symmetric. Thus, the structures generated from both the sides move in the same direction. Overall, the sinuous-like breakdown results in overlapping and wavy vortical structures that leaves behind alternate tilting of the low-speed streak. The average wavelength, λ of the low-speed streak is found to $\lambda = 4\delta$ or $11.6\delta^*$.

Varicose-like breakdown occurs when counter-rotating vortices are generated from either side of the low-speed streaks in a symmetric pattern. The vortices on both the side are ejected from the surface simultaneously resulting in a symmetric v' distribution. The vortices move towards each other resulting in anti-symmetric w' distribution. The vortices are driven normal to the surface by wall-normal shear and eventually merge to form Λ/Ω shaped hair-pin structure at the edge of boundary layer. The length-scale of the hair-pin structures is around $\sim 1\delta$, which is 4 times smaller than the length-scales of the sinuous-like breakdown.

Table 4.2 Summary of vortical structures and instabilities in pre-transition and transition onset regions.

Vortical structures and instabilities		***Current study***	***Literature***[6,35,43]
Pre-transition streaks	Structure	Alternate high- and low-speed longitudinal streaks	
	Spanwise spacing	$1 - 1.2\delta$	$\sim 1.2\delta$
	Core wall normal location	$\sim(0.3 - 0.35)\delta$ or $(0.9 - 1)\delta^*$	$\sim 0.4\delta$ (or $1.3\delta^*$)
	Length-scale, l	$\sim x_{onset}$	$\sim x_{onset}$
Sinuous instability	Vortical structures	Antisymmetric interaction between counter-rotating structures formed between high- and low-speed streaks around low-speed streak.	
	Wavelength, λ	4δ or $11.6\delta^*$	$7 - 11\delta^*$
Varicose instability	Structure	Symmetric interaction of counter-rotating vortices generated from either side of the low-speed (or high-speed) streaks	
	Wavelength, λ	1δ or $0.35\delta^*$	-

As summarized in Table 4.2, the structure, spacing and core location of the pre-transition streak is same as those of Klebanoff modes. The length scale of the streak is proportional to the distance along the plate as reported by S-DNS[6] and by Praisner and Clark[17] using experimental datasets for bypass transition over a turbine cascade. The sinuous- and varicose-like breakdown mechanism and associated wavelength is similar to those reported by Brandt et al.[74] and Schlatter et al.[53].

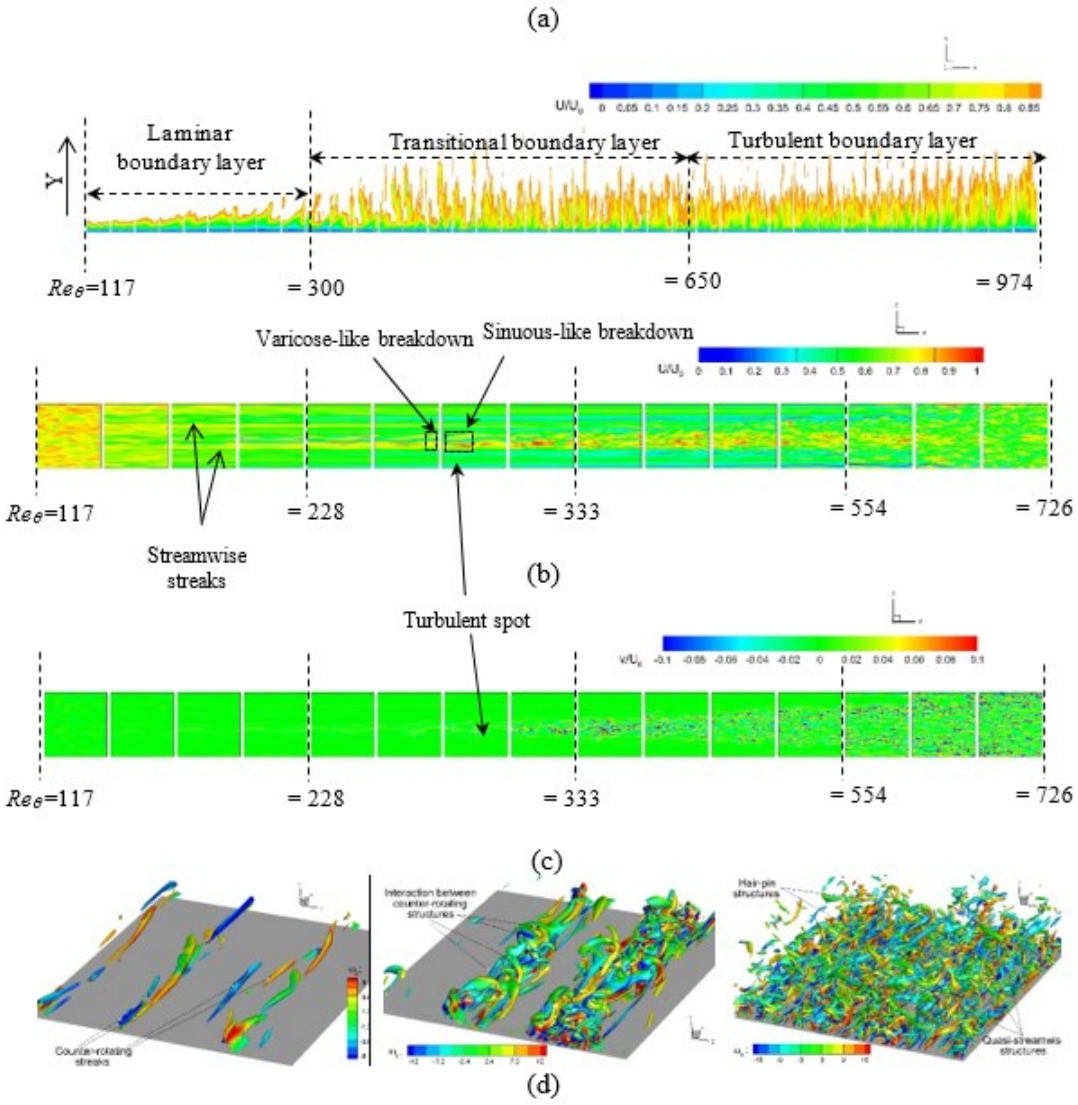

Figure 4.2 (a) Contours of instantaneous streamwise velocity at the spanwise center plane z = 0 obtained every 2000 time-steps (or $1U_0/L$) are shown side-by-side. Contours of: (b) streamwise velocity and (c) wall-normal velocity shown in x-z plane close to the wall at $y = 0.015$ obtained every 4000 time-steps (or $2U_0/L$) are shown side-by-side. The broken boxes in subfigure (b) show the sinuous- and varicose-like breakdown analysis region performed in Figs 4.3 and 4.4, respectively. (d) Turbulent coherent structures are visualized using isosurfaces of λ_2 colored by ω_x in laminar $Re_\theta = 222$ (LEFT), transition $Re_\theta = 412$ (MIDDLE) and turbulent $Re_\theta = 1092$ (RIGHT) regimes. Isosurfaces are shown for $\lambda_2 = -4$, -10 and -20 in laminar, transition, and turbulent regimes, respectively. Results are shown for T-DNS obtained for $Tu_{in} = 3.5\%$ on $30\delta_0$ domain using $\Delta t = 5\times10^{-4}L/U_0$.

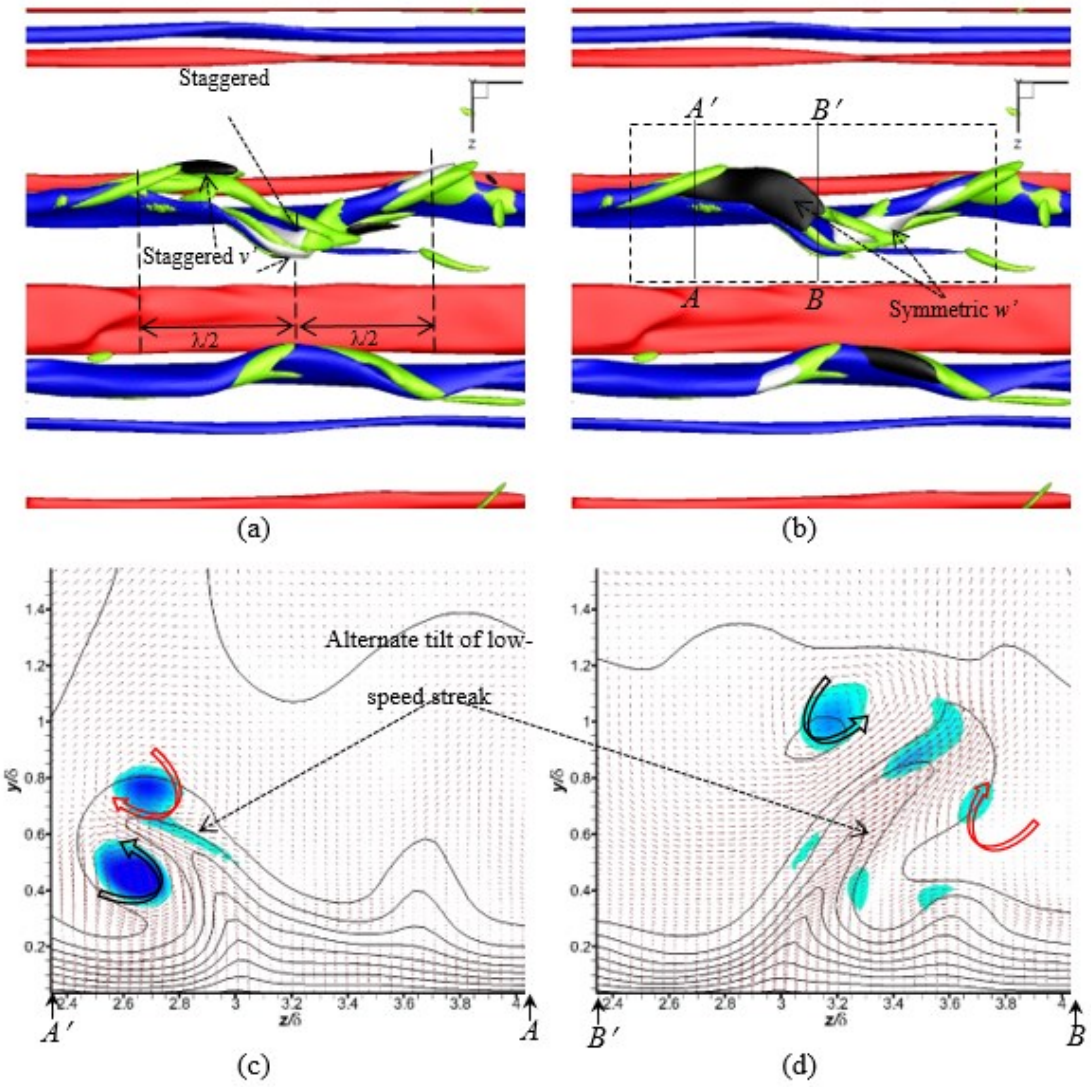

Figure 4.3 Analysis of sinuous-like breakdown of a streamwise streak around $Re_\theta = 280 - 300$ as marked in 1(b). Subfigures (a) and (b) show isosurfaces of $\lambda_2 = -6$ (GREEN), $u' = 0.15$ (RED) and $u' = -0.15$ (BLUE). Subfigure (a) also show isosurfaces of $v' = 0.07$ (WHITE) and $v' = -0.07$ (BLACK). Subfigure (b) also show isosurfaces of $w' = 0.07$ (WHITE) and $w' = -0.07$ (BLACK). Subfigures (c) and (d) show the flow pattern in *y*-*z* plane at $x = 0.2$ (A-A′) and $x = 0.55$ (B-B′), respectively. The streamwise locations are indicated in subfigure (b). Plots show contour lines of constant streamwise velocity from 0.05 to 0.95 with a spacing of 0.1 (BLACK), planar velocity vectors using v' and w', and flooded contour of $\lambda_2 \leq -4$ (BLUE).

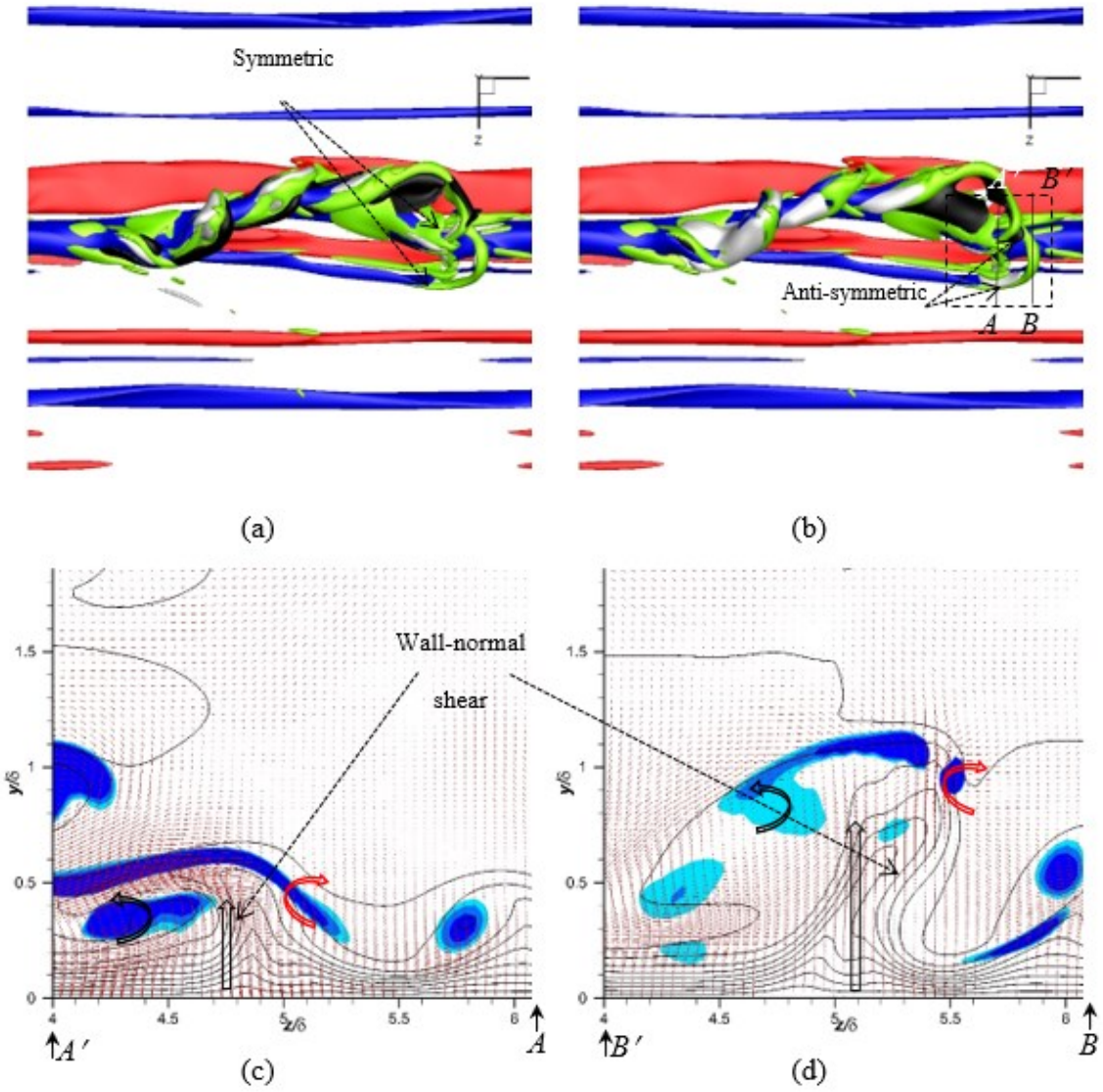

Figure 4.4 Analysis of varicose-like breakdown of a streamwise streak around $Re_\theta = 250 - 270$ as marked in 1(b). Subfigures (a) and (b) show isosurfaces of $\lambda_2 = -6$ (GREEN), $u' = 0.15$ (RED) and $u' = -0.15$ (BLUE). Subfigure (a) also show isosurfaces of $v' = 0.07$ (WHITE) and $v' = -0.07$ (BLACK). Subfigure (b) also show isosurfaces of $w' = 0.09$ (WHITE) and $w' = -0.09$ (BLACK). Subfigures (c) and (d) show the flow pattern in *y*-*z* plane at $x = 0.7$ (A-A′) and $x = 0.8$ (B-B′), respectively. The streamwise locations are indicated in subfigure (b). Plots show contour lines of constant streamwise velocity from 0.05 to 0.95 with a spacing of 0.1 (BLACK), planar velocity vectors using v' and w', and flooded contour of $\lambda_2 \leq -6$ (BLUE).

However, the present study differs from Schlatter et al.[53] for the evolution of the vortical structures in the fully developed turbulent regions. Schlatter et al.[53] reported that the quasi-streamwise vortices should eventually evolve into hair-pin like structures aligned with the spanwise direction. T-DNS does not predict such structures, probably because of the distortion of the structures due to streamwise periodic boundary condition as pointed out by Wu and Moin[54].

4.2 VALIDATION IN BOUNDARY LAYER COORDINATES

4.2.1 BOUNDARY LAYER PREDICTIONS

The predictions of key boundary layer parameters namely the skin friction coefficient C_f, displacement thickness δ^* and shape parameter $H = \delta^*/\theta$ for $Tu_{in} = 3.5\%$ are presented in boundary layer coordinates, Re_θ in Fig. 4.5. Note that the above boundary layer growth parameters are obtained from a planar average (in the $x - z$ plane) of the instantaneous solution. The C_f profile shows laminar regime up to $Re_\theta \leq 330$, transition regime for $330 < Re_\theta \leq 670$, and turbulent regime for $Re_\theta > 670$. The predictions on all the domains compare qualitatively well with the S-DNS, experimental data, and analytic profiles. However, they show some quantitative differences as discussed below.

In the laminar regime, C_f is overpredicted by 11% compared to S-DNS/experiment on $20\delta_0$ and predictions improve with the increase in the domain size such that error is 6% and 2% on $30\delta_0$ and $50\delta_0$, respectively. Grid refinement for $30\delta_0$ domain significantly improves the predictions and results agree within 2% of the S-DNS. However, no significant improvement is observed for the $40\delta_0$ domain. Analysis of the streamwise velocity fluctuation in Fig. 6(d) shows that the overprediction of C_f is correlated with the streamwise turbulent fluctuations

associated with the streaks. Results on $20\delta_0$ domain show significantly higher values, whereas results on both $30\delta_0$ (Fine) and $50\delta_0$ domains show similar lower levels.

In the transition regime, domain size and grid resolution does not show a significant effect on the C_f and Re_{δ^*} predictions, but H improves with the increase in the grid resolution. Results obtained using both the $30\delta_0$ and $40\delta_0$ domains on finer grid compares best with S-DNS. In the turbulent regime, all the simulations show similar predictions with unsteady C_f. Note that the T-DNS results show unsteadiness in the C_f profile, whereas S-DNS is steady. This is because the latter reports the ensemble-averaged values. For both $30\delta_0$ and $40\delta_0$ domains the unsteadiness increases with the increase in grid resolution. On the other hand, predictions on $50\delta_0$ shows the least unsteadiness, possibly due to the coarser grid resolution.

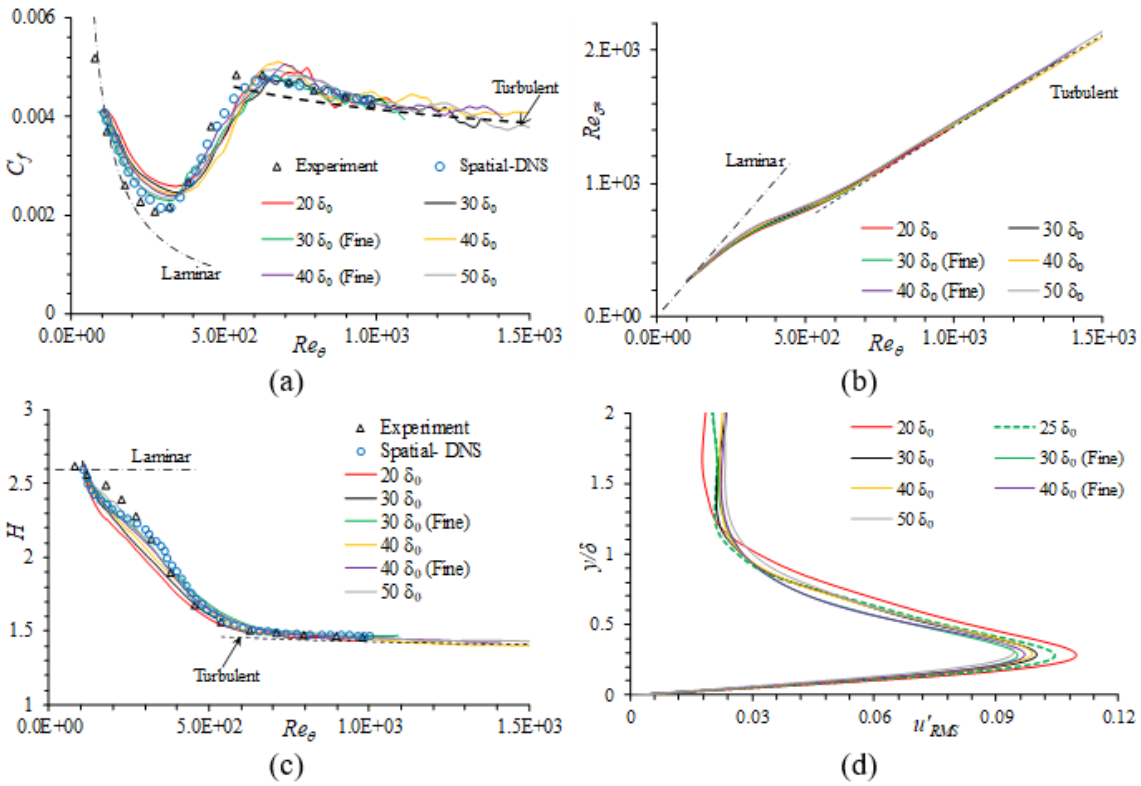

Figure 4.5 T-DNS predictions of: (a) C_f; (b) displacement thickness-based Reynolds number Re_{δ^*}; and (c) shape factor H in boundary layer coordinates obtained on different domain sizes for $Tu_{in} = 3.5\%$. Results are compared with S-DNS[5], experimental data[21], and analytic profiles[26]. (d) Profile of u'_{RMS} in the laminar regime at $Re_\theta = 250$.

4.2.2 EFFECT OF STREAMWISE DOMAIN SIZE

The optimal streamwise domain size for T-DNS is dictated by the streamwise periodicity errors, which is introduced through streamwise boundary layer growth on large domain or through turbulent structures correlation on small domains. Figure 4.6 shows the contours of the two-point correlation of the streamwise velocity fluctuation, $R_{uu} = \langle u'(x)u'(x + r/\delta)\rangle$ normalized using peak $\langle u'^2\rangle$ in the laminar, transition and turbulent regimes obtained on $30\delta_0$ domain for $Tu_{in} = 3.5\%$. Note that the maximum r/δ corresponds to half domain length $L_x/2$ and local boundary layer thickness, δ. As expected, the peak correlation occurs for $r = 0$, and the correlation decreases with the increase in r. The peak R_{uu} location is located at $y/\delta =$

$0.3, 0.2$ and 0.04 in the laminar, transition onset and turbulent regimes, respectively. In the laminar region, the peak location corresponds to the core of the Klebanoff modes. The peak location moves closer to the wall as the flow transition to the turbulent regime, since the near-wall streaks gets embedded in the buffer-layer in the turbulent regime. For the maximum separation length, the correlation decays to $0.2\langle u'^2\rangle$, $0.45\langle u'^2\rangle$ and $< 0.1\langle u'^2\rangle$ in the laminar, transition onset and turbulent regimes, respectively. A high correlation length at the transition onset is expected as Klebanoff modes extend up to breakdown, as discussed above.

The periodicity error introduced in the simulations is estimated from the temporal boundary layer growth. The momentum integral boundary layer equation for temporally developing simulations is derived following Kozul et al.[69] as below (refer to Appendix for details).

$$\frac{\partial \delta^*}{\partial t} - \frac{1}{\rho U_0}\tau_w = -U_0 \frac{\partial}{\partial x}(\theta - U') \tag{4.1}$$

where, $U' = \frac{1}{{U_0}^2}\int_0^\delta \langle u'^2\rangle dy$. Note that the momentum integral boundary equations derived in the appendix use ensemble averaged quantities, whereas here planar averaged quantities are used. For an exact temporal simulation, the spatial growth of the boundary layer is expected to be negligible, i.e., the term on the right-hand side is expected to be zero and any deviation can be attributed to periodicity errors. The terms on the left-hand side of Eq. 4.1 are obtained from T-DNS predictions as shown in Fig. 4.7(a), and used for the estimation of averaged percentage errors as:

$$E_1 = \left\{\frac{1}{(\theta_2 - \theta_1)}\int_{\theta_1}^{\theta_2}\left|1 - \frac{\partial \delta^*}{\partial t} \Big/ \frac{1}{2}U_0 C_f\right| d\theta\right\} \times 100 \tag{4.2}$$

where, θ_2 and θ_1 are the lower and upper-bound of momentum thickness of the flow regime.

As shown in Fig. 4.7(b) for all the three flow regimes errors decrease sharply from $20\delta_0$ to $30\delta_0$ domains and increase for larger domains. Note that the only exception is the results for the turbulent regime on $50\delta_0$ domain, which shows a lower error than those for the $40\delta_0$ domain. This is because the former predicts lower turbulent unsteadiness than the latter. Further, predictions in the laminar regime show larger errors than those in the transition and turbulent regimes. This is expected as the Klebanoff modes extend beyond the domain size and are more susceptible to periodicity effects. The errors reduce with grid refinement, and the least errors are obtained on $30\delta_0$ domain with finer grid.

Overall, both $30\delta_0$ and $40\delta_0$ domains show reasonable periodicity error $E_1 \leq 4\%$ for all three flow regimes. However, the $30\delta_0$ domain allows finer grid resolution for similar domain sizes. Thus, $30\delta_0$ is identified to be the optimal domain size for $Tu_{in} = 3.5\%$ simulations. This domain results in a local domain size of $\sim 8.3\delta$ in the streak breakdown region. The turbulent spots have wavelength of $\lambda \sim 4\delta$ (as discussed above), thus this domain size is sufficiently large to resolve the turbulent spots. The domain is also sufficiently large in the turbulent region, as the turbulent structures are well de-correlated and boundary layer growth is very gradual. However, the temporal simulations may have limitations in the pre-transition regions as Klebanoff modes show strong two-point correlation.

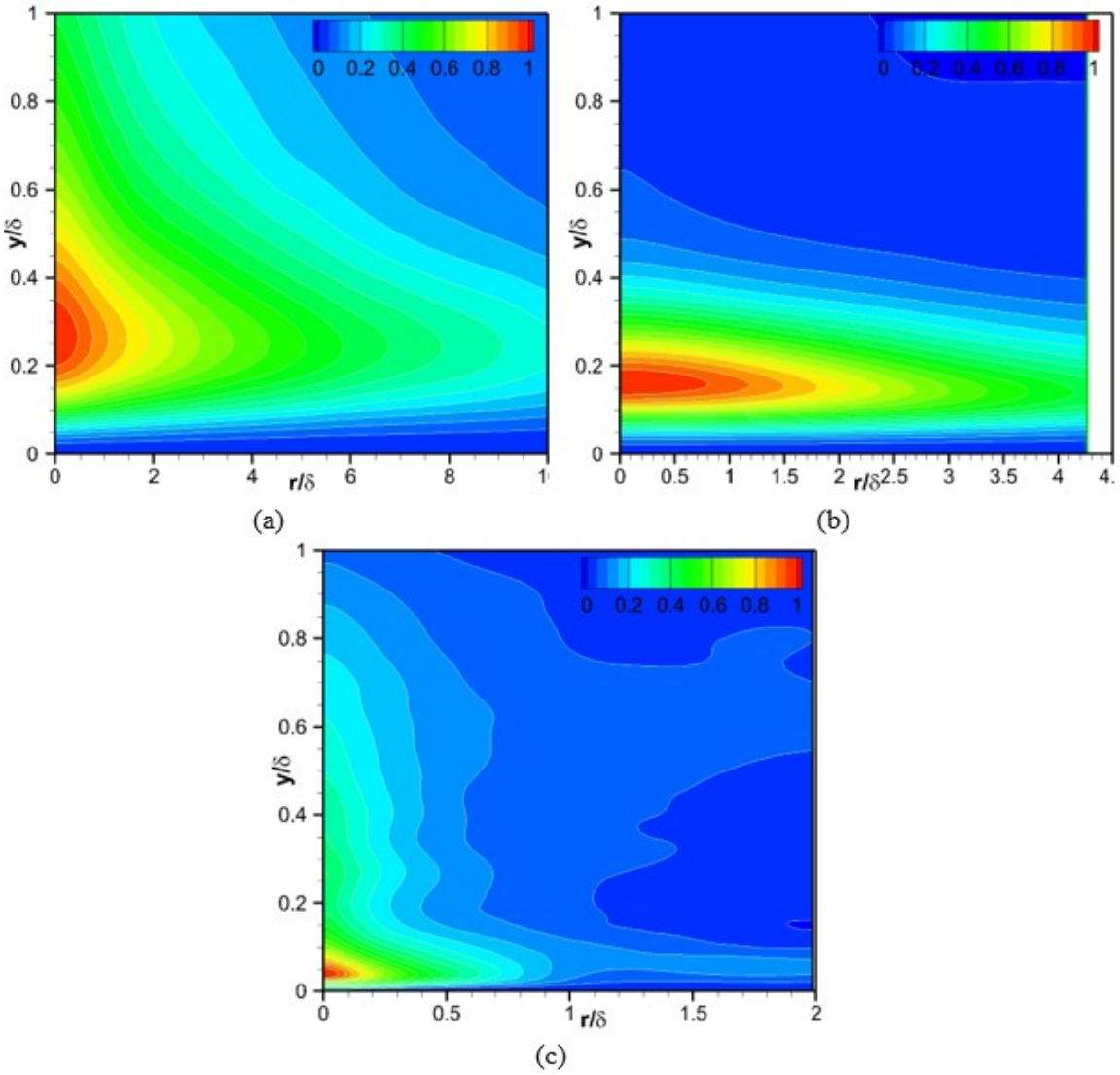

Figure 4.6 Contour of two-point correlation of streamwise velocity fluctuation (R_{uu}) normalized by peak $\langle u'^2 \rangle$ in the (a) laminar regime ($Re_\theta = 252$), (b) transition regime ($Re_\theta = 350$), and (c) turbulent regime ($Re_\theta = 1036$). The abscissa shows the two-point separation length normalized by boundary layer thickness.

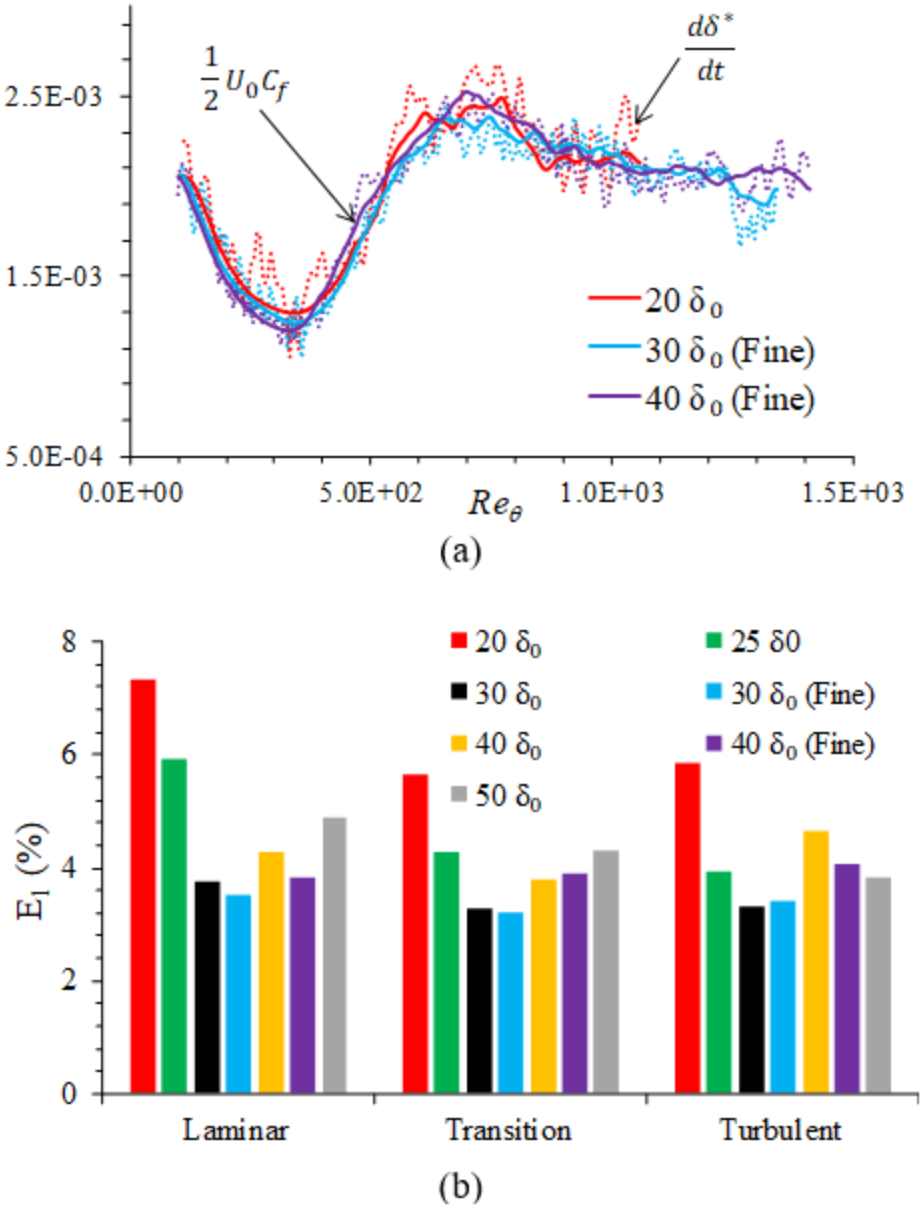

Figure 4.7 (a) Variation of $\frac{d\delta^*}{dt}$ (dotted lines) and $\frac{1}{2}U_0C_f$ (solid lines) in boundary layer coordinates. (b) Temporal momentum integral boundary layer equation prediction errors in laminar ($106 \leq Re_\theta \leq 330$), transition ($330 < Re_\theta \leq 670$), and turbulent ($670 < Re_\theta \leq 1500$) regimes. Results are shown for $Tu_{in} = 3.5\%$ on different domain sizes.

Results discussed hereafter for $Tu_{in} = 3.5\%$ are using those on $30\delta_0$ domain using fine grid. The $30\delta_0$ domain is also used for smaller Tu_{in}. The local domain size in the streak breakdown region

is estimated to be $\sim 6\delta$, 5.5δ, and 3.8δ for $Tu_{in} = 2.8\%, 2.1\%,$ and 1.4% respectively. Thus, the domain may not be sufficiently large for the smallest Tu_{in} to resolve the turbulent spot.

4.2.3 MEAN FLOW AND SECOND ORDER TURBULENT STATISTICS

The averaged mean and turbulent flow profiles presented in this section are obtained using planar averaging in the $x - z$ plane along with time window averaging and are represented by $\bar{}$. The window averaging period is selected to be $\alpha\delta/u_\tau$, where $\alpha = 0.5$, following Kozul et al.[69].The mean velocity and Reynolds stress predictions normalized using local friction velocity, u_τ in the laminar, transition and turbulent regions are compared with S-DNS and experimental data in Figs. 4.8 and 4.9.

The mean velocity, $U^+ = \bar{u}/u_\tau$ profile shows a large sub-layer in the laminar region, growth of the log-layer in the transition region, and a well-defined log-layer in the turbulent region. The streamwise velocity fluctuations, $u^+ = \sqrt{\overline{u'^2}}/u_\tau$ shows rapid growth of in the pre-transition region with peak around $y^+ \sim 20$, the peak value overshoots close to the transition onset, and is transported away from the wall during transition resulting in a somewhat flatter profile in the turbulent region. The other two velocity fluctuations, $v^+ = \sqrt{\overline{v'^2}}/u_\tau$; $w^+ = \sqrt{\overline{w'^2}}/u_\tau$ and shear stress, $uv^+ = \overline{u'v'}/u_\tau^2$ show a steady growth after the transition onset and are transported away from the wall similar to the streamwise component. The profile of the root-mean-square value of the streamwise fluctuating velocity $u_{rms}/u_{rms,max}$, where $u_{rms} = \sqrt{\overline{u'^2}}$, in the pre-transition region shows a self-similar behavior as shown in Fig. 4.10. The growth of the streaks compares well with the linear optimal streak computed by Andersson et al.[77], S-

DNS of Brandt et al.[74] and experimental profiles reported by Westin et al.[78]. Overall, the mean and turbulent flow predictions compare reasonably well with both the S-DNS and experiment data.

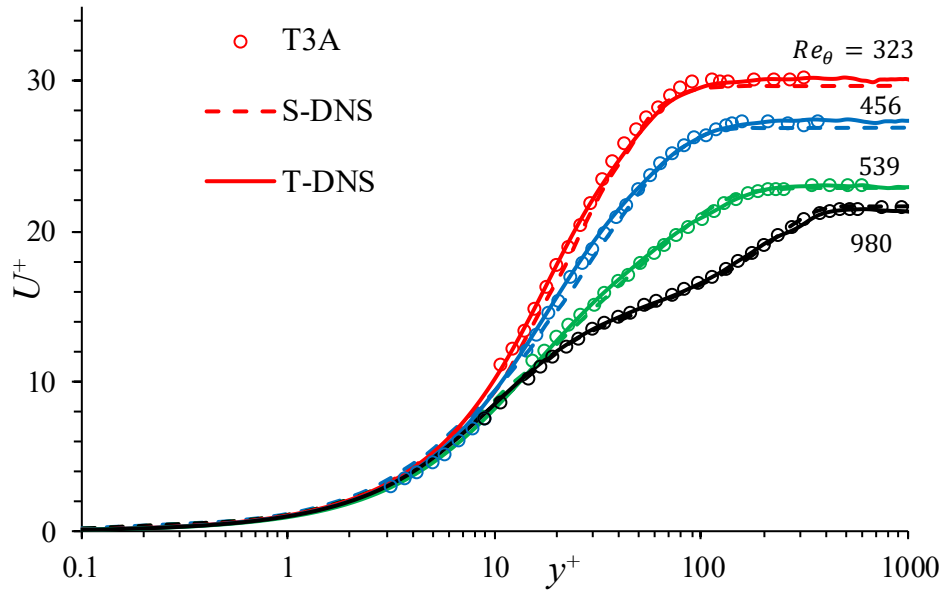

Figure 4.8 Mean velocity profiles predicted by T-DNS in laminar, transition, and turbulent regimes are compared with S-DNS[6] and T3A bypass transition experiments[26]. Re_θ locations for the respective profiles are as indicated on the figure.

4.2.4 BUDGETS AND HIGHER ORDER STATISTICS

As shown in Fig. 4.11, the turbulent kinetic energy ($TKE = \frac{1}{2}\tau_{ii}$) budget (both normalized by ν/u_τ^4) in the fully developed boundary layer ($Re_\theta = 1100$) are in reasonable agreement with S-DNS of Jimenez et al.[75] and channel flow ($Re_\tau = 590$) DNS of Moser et al.[76].

The predictions for the skewness and kurtosis of the streamwise velocity fluctuations in the fully developed turbulent flat-plate boundary layer ($Re_\theta = 1000$) are compared against S-

DNS of Schlatter et al.[10] and channel flow DNS[76] at $Re_\tau = 590$ in Figure 4.12. T-DNS predictions agree reasonably well with S-DNS for both skewness and flatness, except for some differences in the outer boundary layer region ($y^+ > 200$).

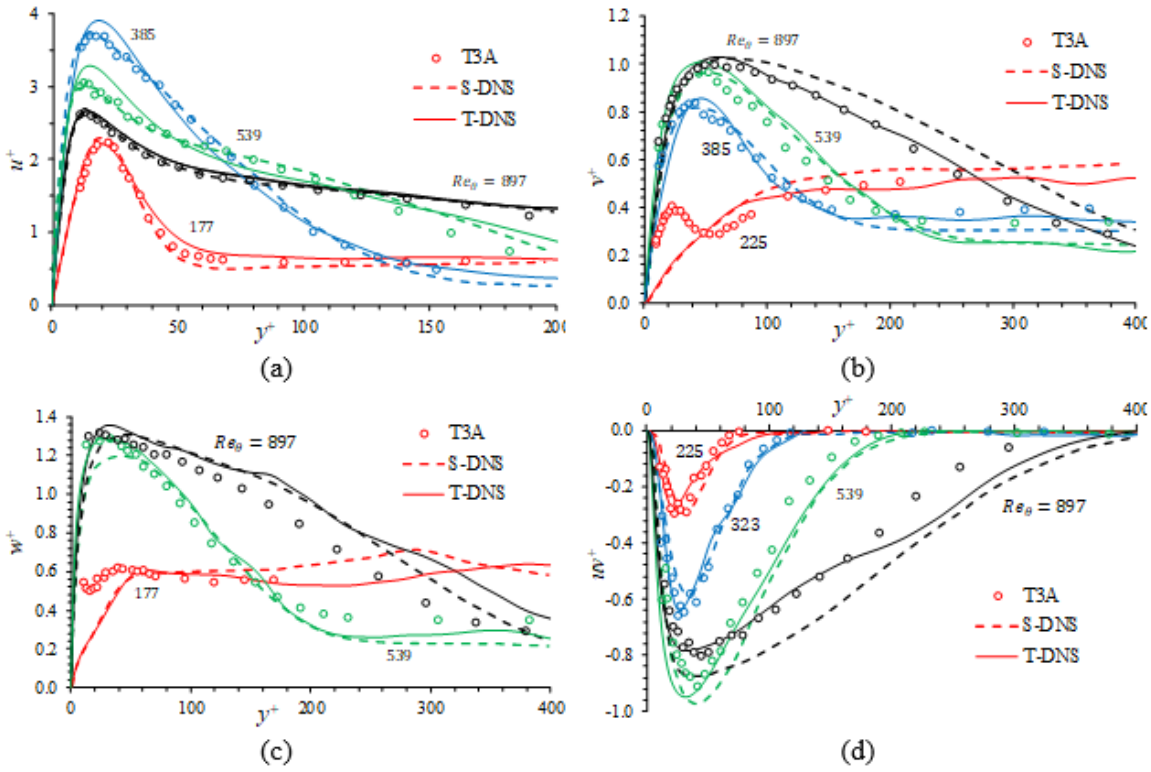

Figure 4.9 Evolution of Reynolds stress components, a) streamwise $u^+ = \sqrt{\overline{u'^2}}/u_\tau$; b) wall-normal $v^+ = \sqrt{\overline{v'^2}}/u_\tau$; c) spanwise, $w^+ = \sqrt{\overline{w'^2}}/u_\tau$; and d) shear stress $\overline{u'v'}/u_\tau^2$ predicted by T-DNS in laminar, transition, and turbulent regimes compared with S-DNS[6] and T3A bypass transition experimental data[26]. Re_θ locations for the respective profiles are as indicated on the figure.

The flat plate skewness and kurtosis predictions compare well with those of the channel flow up to $y^+ \sim 100$, but shows divergence for higher y^+ as the boundary layer transitions from the inner to outer layer. One key difference between the two is the flatness values in the sublayer,

which could be due to difference in Re_τ. The divergence in the skewness and flatness in the outer layer region suggest that the streamwise turbulent fluctuations are primarily dominated by deficit events and occur over a wider length-scale compared to those in the log-layer.

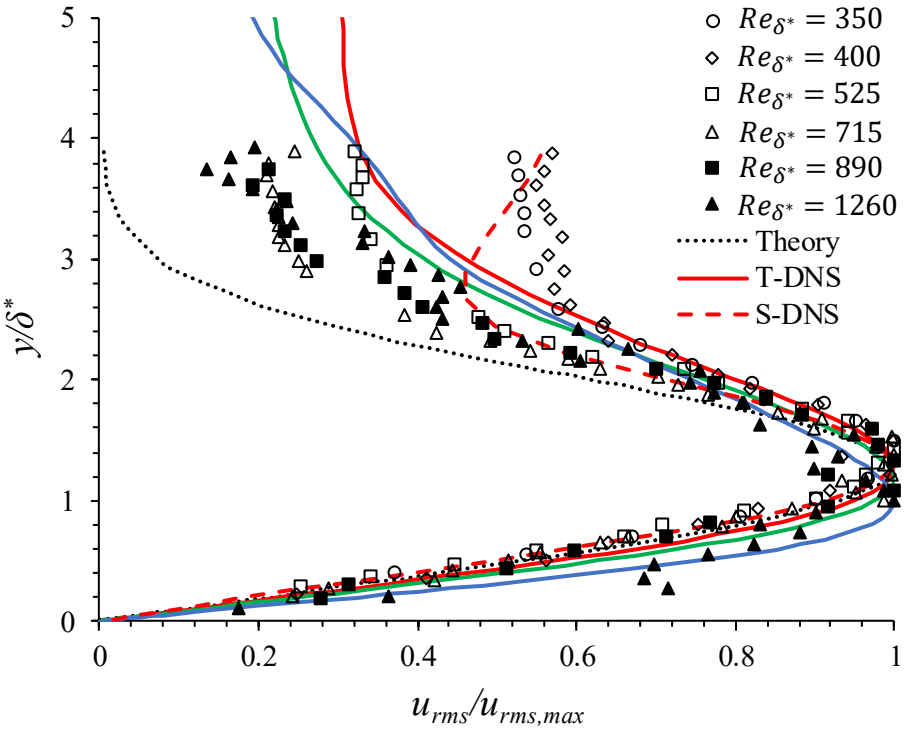

Figure 4.10 a) Wall-normal profiles of $u_{rms}/u_{rms,max}$ at $Re_\theta = 177$ (red solid line), $Re_\theta = 225$ (green solid line), and $Re_\theta = 323$ (blue solid line). Sold lines represent T-DNS results. Dashed line indicates S-DNS data of Brandt et al. [74]; Dotted line indicates transient growth theory of Andersson et al.[77]; Symbols indicate experiments of Westin et al. [78].

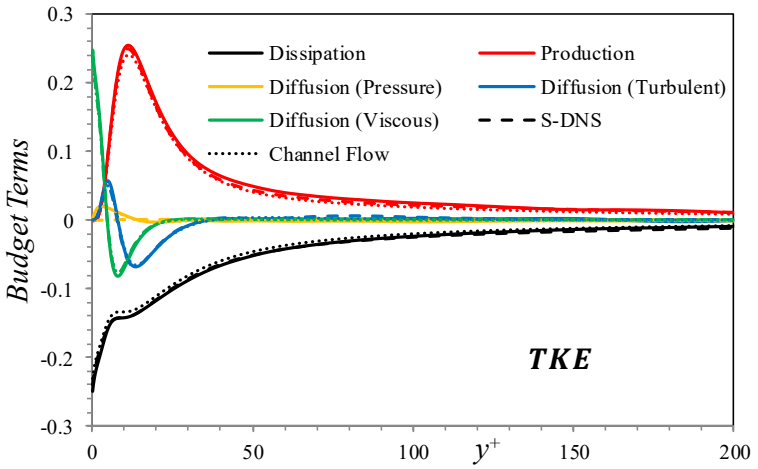

Figure 4.11 TKE budget in the fully developed turbulent regime ($Re_\theta = 1100$) are compared with S-DNS data of Jimenez et al.[75] and channel flow DNS of Moser et al.[76] ($Re_\tau = 590$). All budget terms are normalized by ν/u_τ^4.

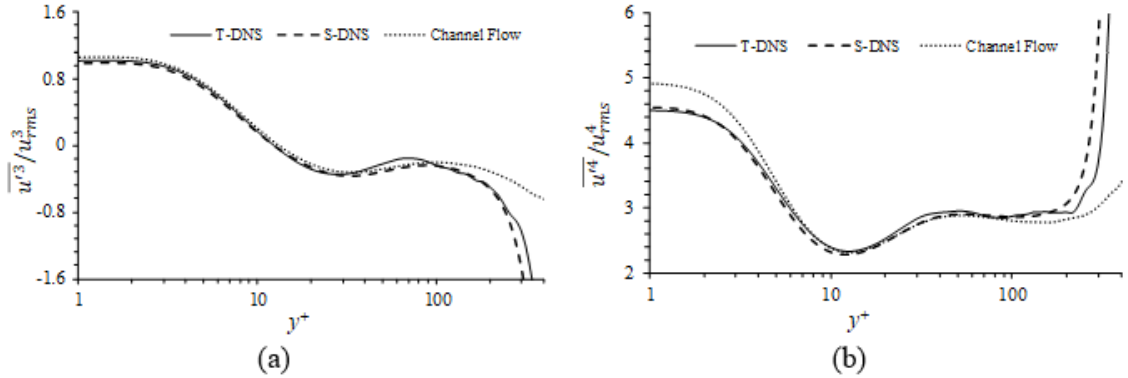

Figure 4.12 T-DNS predictions of: (a) streamwise skewness; and (b) streamwise flatness in the fully developed turbulent regime ($Re_\theta = 1000$) are compared with S-DNS data of Schlatter et al.[10] of the fully developed turbulent boundary layer and channel flow DNS of Moser et al.[76] ($Re_\tau = 590$).

4.3 VALIDATION IN PLATE (Re_x) COORDINATES

The temporal evolution of the flow needs to be transformed into spatial coordinates for direct comparison with the S-DNS. The spatial location can be estimated as:

$$Re_x(t) = Re_{x0} + \frac{U_\infty}{\nu}\int_0^t \delta x(t) \tag{4.3}$$

where, x_0 is the initial plate location. For an accelerating system, the domain translation can be represented in terms of domain translation velocity $V_D(t)$ and acceleration $a(t)$ as:

$$\delta x(t) = V_D(t)\delta t + \frac{1}{2}a(t)\delta t^2 \tag{4.4}$$

Figure 4.13(a) compares Re_x estimates obtained using $V_D = U_0$ and $a(t) = 0$ for three different time step sizes, where the largest to smallest time step ratio is 2.3. The results show a reasonable collapse in all the flow regimes. This suggests that the domain translation varies linearly with time and does not depend significantly on its acceleration,

i.e.,

$$\delta x(t) = V_D(t)\delta t \tag{4.5}$$

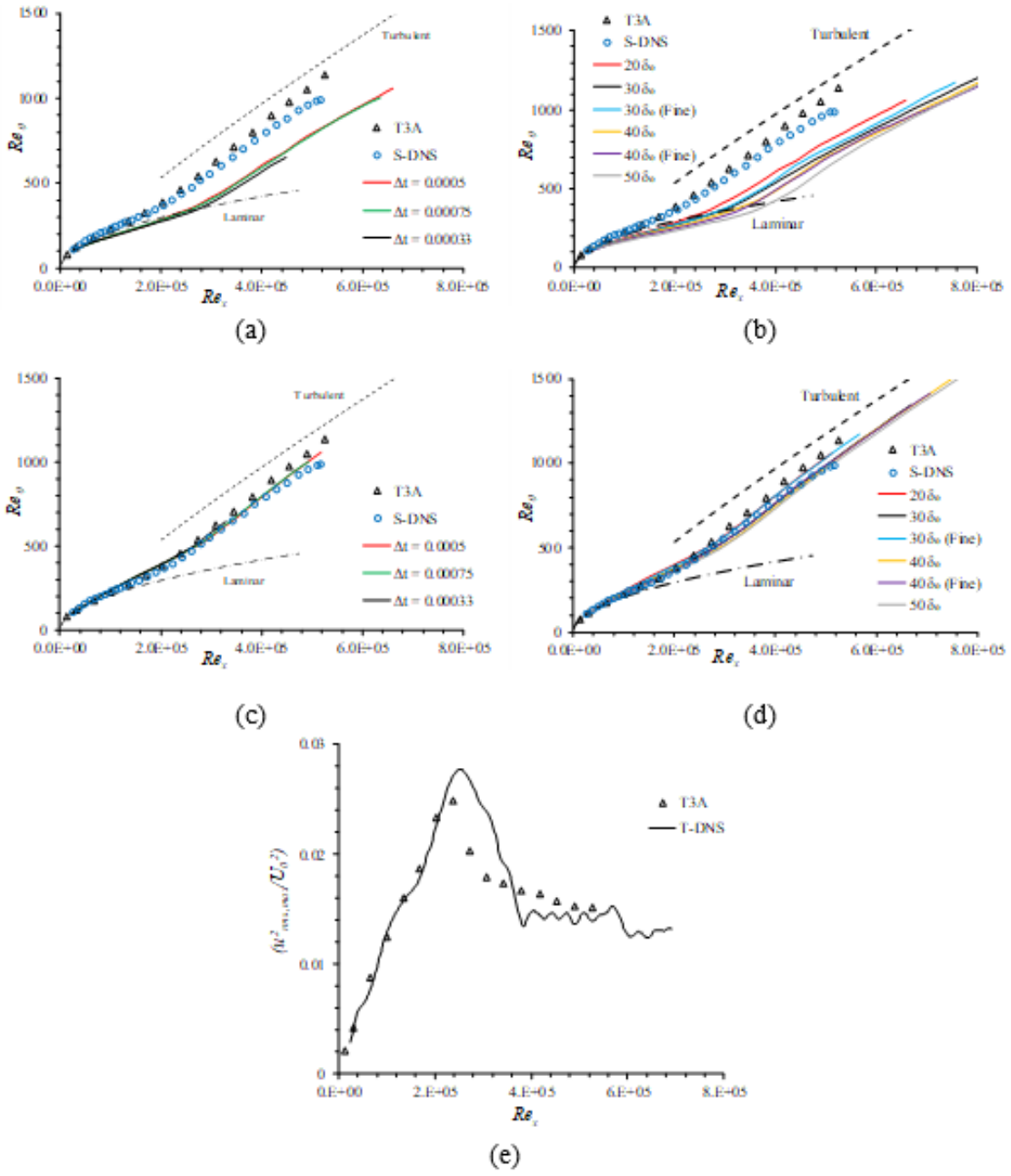

Figure 4.13 T-DNS predictions of Re_θ growth in plate coordinates obtained using domain velocity $V_D = U_0$ with different (a) time step sizes and (b) domain sizes. Re_θ growth in plate coordinates using domain velocity $V_{D,MI}$ with different (c) time step sizes and (d) domain sizes. (e) Growth of $u^2_{rms,max}/U_0^2$ with Re_x compared with S-DNS[6], T3A[26] bypass transition experimental data, and analytic profiles[79].

Next, $V_D = U_0$ is used for Re_x estimates on different domain sizes. As shown in Fig. 4.13(b) the predictions show significant variation on domain size. Thus, V_D is expected to be a function of the boundary layer parameters.

The domain translation velocity is estimated from the momentum integral boundary layer equation assuming negligible temporal growth of the displacement and boundary layer thickness (refer to Appendix for details) as below:

$$V_{D,MI}(t) = \frac{d}{dt}\{\theta(t) - U'(t)\}/\frac{1}{2}C_f(t) \tag{4.6}$$

As shown in Figs. 4.13(c) and (d), the Re_x estimates using $V_{D,MI}$ provides a good collapse between the results obtained using different time step and domain sizes, and they agree well both with the S-DNS and experimental data. The growth of $u^2_{rms,max}/U_0^2$ with Re_x obtained using $V_{D,MI}$ in Fig. 4.13(e) shows a linear increase in the pre-transition and transition regions followed by a rapid decrease once the transition is completed, and eventually quasi-steady fully developed region is achieved. The predictions are in good agreement with T3A experimental results[26].

The variation/evolution of the domain velocity, $V_{D,MI}$ for different domain sizes is shown in Fig. 4.14. The average $V_{D,MI} \sim 0.55U_0$ in the laminar region. $V_{D,MI}$ starts to increase towards the end of the laminar regime, keeps increasing somewhere in the middle of the transition regime, then starts decreasing until the transition is completed, and eventually achieves a quasi-steady value of around $V_{D,MI} = 0.75U_0$ in the turbulent region.

The decay of free-stream turbulence intensity Tu/Tu_{in} and turbulence length scale ℓ/δ along the plate length are compared with S-DNS in Fig. 4.15. Similar to the boundary layer predictions, the predictions on different domain sizes show a scatter in the results when Re_x is

computed using $V_D = U_0$ (figure not shown), but they show a reasonable collapse when Re_x is computed using $V_{D,MI}$. The results compare reasonably well with S-DNS and analytic profiles for both the parameters. Among the results, the best prediction is obtained on $30\delta_0$ with fine grid resolution closely followed by $40\delta_0$ on fine grid as well. Both the $20\delta_0$ and $40\delta_0$ domains with coarser grid resolution show largest errors.

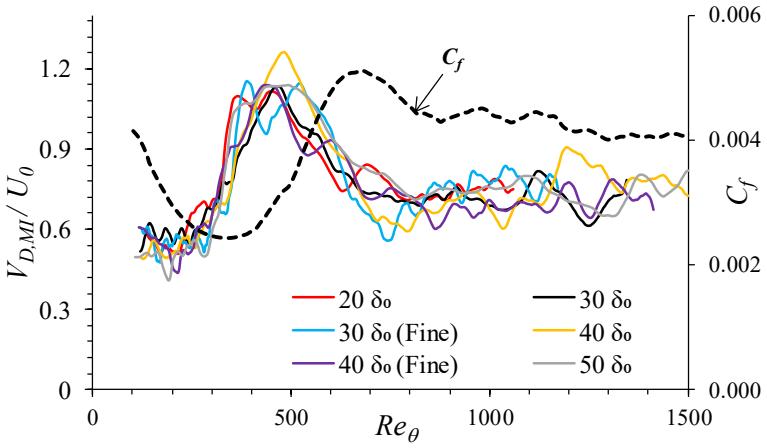

Figure 4.14 Primary axis shows the variation of $V_{D,MI}$ for $Tu_{in} = 3.5\%$ obtained on different domain sizes. C_f variation is shown in the secondary axis to depict how domain velocity varies in the laminar, transition, and turbulent regimes.

Figures 4.16(a) and (b) compares the predictions in boundary layer coordinates for Tu_{in} ranging from 1.4% to 3.5%, including laminar predictions for a very low $Tu_{in} = 0.01\%$ in boundary layer coordinates. As expected, the transition onset is delayed and the C_f growth rate in the transition regime increases with the decrease in Tu_{in}. In addition, growth of Re_{δ^*} in the laminar and turbulent regimes compares well with the analytic profiles. Figure 4.16(c) shows the Re_θ growth in plate coordinates using $V_D = U_0$. As evident, predictions show significant deviation from the analytic profile in the laminar region, and the slope in the turbulent region is

larger compared to the analytic profiles. Whereas, the estimation of the plate coordinates using $V_{D,MI}$ in Fig. 17(d) provides a good agreement with the laminar and turbulent analytic profiles. The growth of Re_{δ^*} computed using $V_{D,MI}$ in Fig. 4.16 (e) also compares well with the analytic profiles in both the laminar and turbulent regimes.

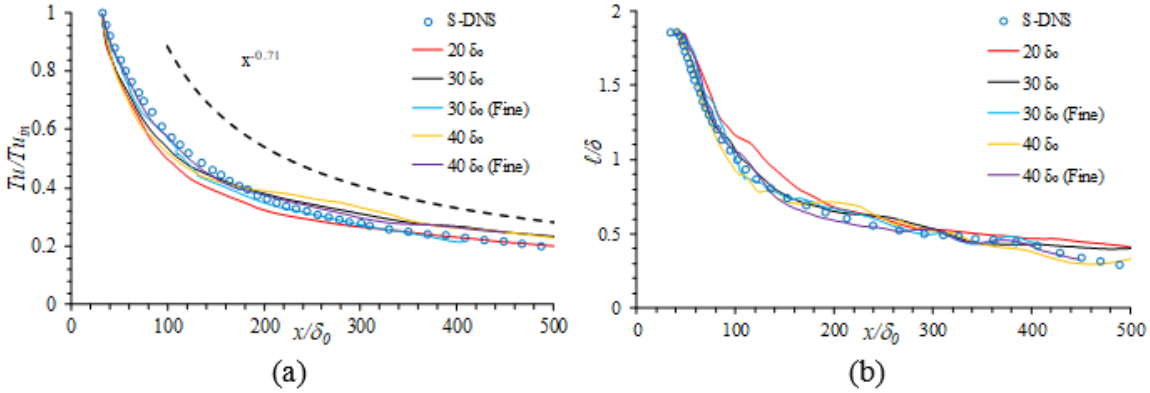

Figure 4.15 T-DNS predictions of: (a) free-stream turbulence intensity Tu/Tu_{in}; and (b) turbulence length scale ℓ/δ decay along the plate length x/δ_0 computed using $V_{D,MI}$. Results are compared with S-DNS[6] and analytic profiles[79].

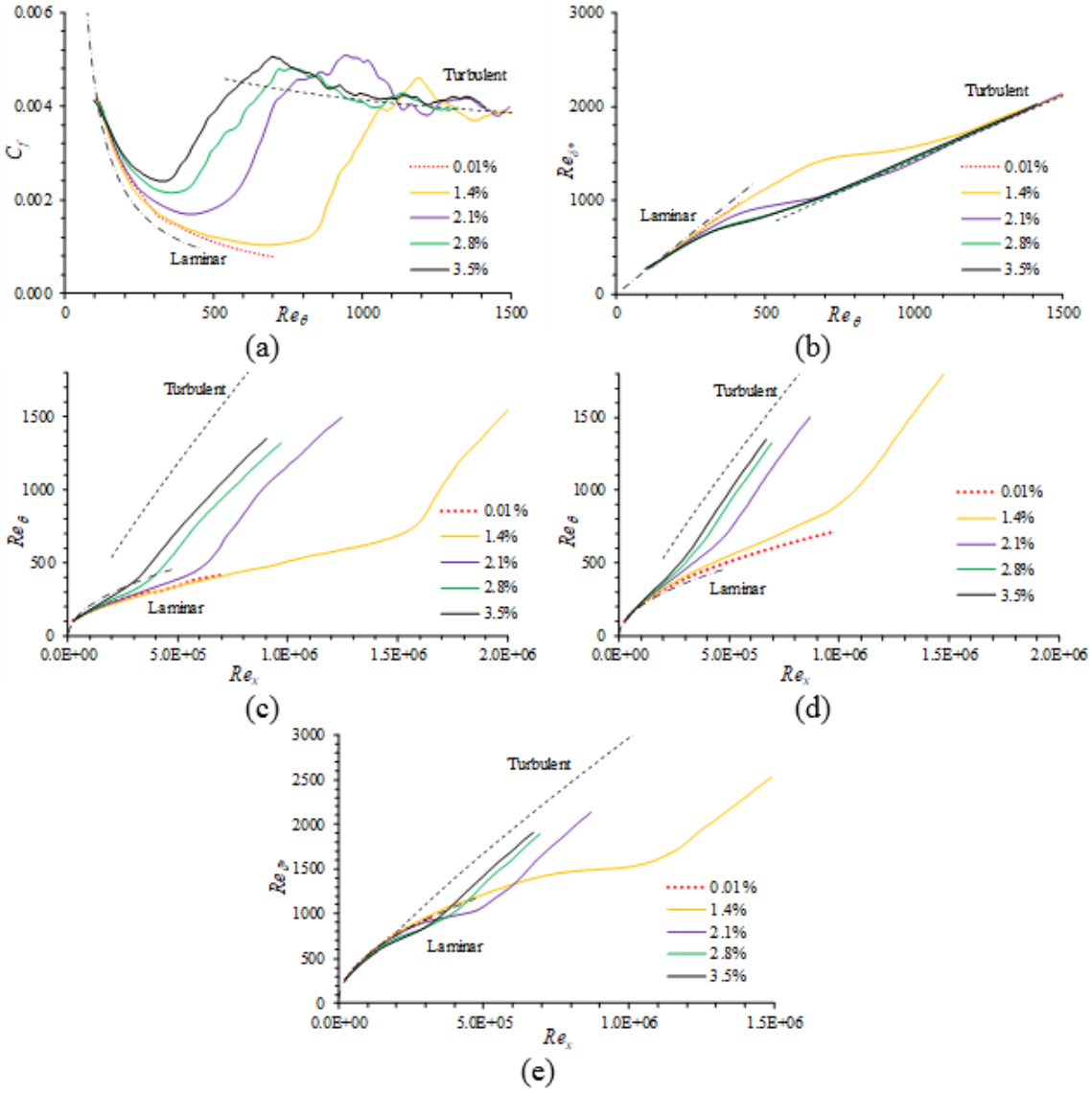

Figure 4.16 T- DNS predictions for different Tu_{in} are compared with analytic profiles[79]. Evolution of (a) C_f and (b) Re_{δ^*} in boundary layer coordinates. Growth of Re_θ in plate coordinates computed using: (c) $V_D = U_0$ and (d) $V_{D,MI}$. (e) Growth of Re_{δ^*} in plate coordinates computed using $V_{D,MI}$.

4.4 CONCLUSIONS AND FUTURE WORK

Computational issues associated with temporally developing simulations for bypass transition flow were investigated using DNS of flat-plate boundary layer under zero pressure

gradient. The temporal simulations predict the growth of near-wall Klebanoff modes in the laminar regime, their subsequent breakdown in the transition regime, and the generation of counter-rotating quasi-streamwise and hair-pin structures in the turbulent regime. The optimal domain size for T-DNS is dictated by streamwise periodicity errors due to spatial correlation on smaller domains and boundary layer growth on larger domains. A domain size of $30\delta_0$ is identified to be the optimal domain size for simulation with $Tu_{in} = 2.1\%$ to 3.5%, but larger domains are required for a lower Tu_{in}. A formulation of the domain translation velocity was derived from the momentum integral turbulent boundary layer equations. The domain velocity was found to be the same both for the boundary layer growth and free-stream decay and the formulation was found to be robust for a range of Tu_{in}.

The growth of mean and turbulent flow in the boundary layer and free-stream decay predictions compared well with the spatial DNS and experimental data in both boundary layer and plate coordinates. The temporal simulations required 20 times smaller streamwise domain size compared to spatial DNS for $Tu_{in} = 3.5\%$. The domain size requirements for the temporal approach are expected to be even smaller for lower Tu_{in}. Overall, results demonstrate that the temporal approach can accurately predict the interaction between the turbulent boundary layer and free-stream turbulence and is a viable inexpensive alternative to the spatial approach for bypass transition simulations focusing on flow physics analysis.

The temporally developing simulations involve the following two limitations. (1) They may have limitations in accurately resolving the near-wall Klebanoff streaks, as they extend up to breakdown, and periodicity assumption is not applicable. However, for sufficiently large domains the above limitation does not significantly affect the prediction. (2) The simulation does not allow for ensemble averaging similar to spatially developing simulations. The time-window

averaging along with planar averaging over homogenous directions does significantly improve the convergence of turbulent statistics. The T-DNS simulations are intended for evaluation of transition onset markers[80], and for such cases planar and window averaging is sufficient. However, the most accurate way to achieve ensemble averaging is to perform multiple simulations with different initial conditions. The use of multiple simulations though is expected to increase the computational expense of the temporal approach, and adversely affect the advantages of the temporal approach over spatial approach. Future work will focus on application of T-DNS simulation for bypass transition for different free-stream turbulence length scales to study its effect on transition onset following Brandt et al.[74].

CHAPTER V

IDENTIFICATION OF BYPASS TRANSITION ONSET MARKERS USING DIRECT NUMERICAL SIMULATION

Currently available general-purpose transition sensitive RANS turbulence models can be loosely classified as either correlation-based [15] or physics-based [16]. Correlation-based models typically solve for an intermittency transport equation, which is the fraction of time the flow is turbulent during the transition phase and is used as a turbulent eddy viscosity multiplier. Several studies have reported that the intermittency distribution shows a universal behavior upon normalization [17]. The transition onset location is either specified explicitly based on empirical correlations or solved for using additional transport equations. These models rely directly on empirical correlations to specify model parameters.

Physics-based models [16] though still highly empirical in nature, aim for a more generalized approach wherein the evolution of turbulent fluctuations is predicted in the pre-transitional and transitional regions. Development of such models require: (1) a proper understanding of turbulence production processes such as entrainment of freestream turbulence, development of fluctuations in the pre-transitional regions including turbulence damping (shear sheltering), boundary layer breakdown (turbulent spot formation), turbulent energy production dynamics, and overshoot of turbulent fluctuations in the post transition region; and (2) evaluation and/or identification of flow parameters that can be used as a marker for turbulence onset/growth in low-fidelity RANS simulations. Previously documented large eddy simulation (LES) and

direct numerical simulation (DNS) studies have helped in highlighting some of the underlying transitional flow physics [7,9,18] to address the above requirements. Studies agree that freestream disturbances induce low-frequency streamwise vortices or streaks in the pre-transitional region (referred to as Klebanoff modes), which lift from the wall causing ejection events. Transition occurs due to the formation of turbulent spots, which are associated with multiple head hairpin-type vortices with U- or Λ-shaped structures underneath them. However, the energy transfer pathway from freestream disturbances to pre-transitional (non-turbulent) fluctuations to turbulent fluctuations remains somewhat unclear. Mayle and Schultz [20] identified the pressure-diffusion terms as the driver of the growth of Klebanoff modes from freestream disturbance, and pressure-strain terms as the driver of the energy redistribution from the Klebanoff modes to the other components. The latter is also supported by Lardeau et al. [21], wherein it was indicated that unlike the fully developed turbulent region, the pressure-strain terms are negligible in the pre-transition regime. Walters et al. [19] hypothesized that the absence of the pressure-strain inhibits nonlinear turbulence breakdown, and is closely related to shear-sheltering, as proposed by Jacobs and Durbin [6,22].

Evaluation/identification of a relevant marker for transition onset location is also an open question. Ideally, for use in transition-sensitive RANS models, a marker could be identified based solely on local statistical flow variables available in a RANS simulation. Several studies have reported peak streamwise velocity fluctuations u'/U_∞ as a transition onset marker, where U_∞ is the free-stream mean velocity. For example, Mandal et al. [23] analyzed experimental measurements of flat-plate boundary layer bypass transition for free-stream turbulence intensities

(Tu_{in}) = 1, 1.8 and 3.8% and reported a critical value[1] of $u'/U_\infty \sim 9\%$. He and Seddighi [24] performed DNS of transient flow in a channel, wherein flowrate was increased such that the Reynolds number rapidly increased from $Re_\tau = 180$ to $Re_\tau = 420$. The flow development showed pre-transition and transition phases similar to bypass transition, and it was reported that transition onset occurred at a critical value of $u'/U_\infty \sim 14\%$. The DNS study of Vaughan and Zaki [25] reported a critical value of $u'/U_\infty \sim 10 - 15\%$ for bypass transition over a flat-plate. Sharma et al. [81] used u'/u_τ as the transition onset marker and reported a critical value of ~ 3 based on the analysis of turbine airfoil bypass transition experimental data. Praisner and Clark [17] developed a correlation for the transition onset using a dataset of 104 turbine cascade experiments. It was identified that transition onset occurs when the ratio of laminar diffusion time-scale ($T_{d,PC}$) to local, energy-bearing turbulent fluctuation time-scale (T_r) reaches a critical value. The boundary layer diffusion time-scale was defined based on the momentum thickness (θ) of the boundary layer and kinematic viscosity (ν), and the turbulent time-scale was estimated from the root mean square (RMS) of streamwise velocity fluctuations (u') and their integral length-scale (λ), to yield the transition criterion:

$$T_{c,PC} = \frac{T_{d,PC}}{T_{r,PC}} = \left(\frac{\theta^2}{\nu}\right)\left(\frac{u'}{\lambda}\right) = 0.07 \pm 16\% \tag{5.1}$$

The time-scale was found to be nearly constant over a wide range of flow field conditions. Substituting the Blasius solution[2], the critical time-scale ratio gives:

[1]The parameter value at the transition onset is referred to as the critical value.

[2]$\delta = 5\sqrt{\frac{\nu x}{U_\infty}}$ and $\theta = 0.133\delta$, where δ is the boundary layer thickness, and x is distance from the plate leading edge.

$$\frac{u'}{U_\infty} = \{0.16 \pm 16\%\}\frac{\lambda}{x} \tag{5.2}$$

Jacobs and Durbin [6] reported that the near-wall streamwise streaks (Klebanoff modes) extend throughout the transition region, i.e., $\lambda \sim x$, therefore the Praisner and Clark [17] transition onset parameter is potentially consistent with the u'/U_∞ parameter used in other studies.

Walters et al. [16,19] developed a physics based model building on the physics of Klebanoff mode growth identified in LES/DNS studies, as discussed above. In this model, the growth of the pressure-strain was assumed to correspond to the energy transfer during transition from pre-transitional fluctuations (Klebanoff modes) to boundary layer turbulence. It was approximated that the transition occurs when the ratio of molecular diffusion time-scale ($T_{d,W}$) to pressure-strain time-scale ($T_{r,W}$) increases to a critical value. The molecular diffusion time-scale was estimated as:

$$T_{d,W} = \frac{k_T}{\nu\omega^2} \tag{5.3}$$

where k_T is the local entrained turbulent kinetic energy and ω is the local mean vorticity magnitude. The time-scale associated with the rapid pressure strain mechanisms was estimated as:

$$T_{r,W} = 1/\omega \tag{5.4}$$

The critical time-scale ratio used in the model was calibrated using numerical simulations of flat-plate and turbine cascade test cases, which resulted in:

$$T_{c,W} = \frac{T_{d,W}}{T_{r,W}} = \frac{k_T}{\nu\omega} = 1.2 \tag{5.5}$$

The objective of this study is to investigate the transition onset markers discussed above and analyzed to evaluate their potential efficacy as transition onset criteria in RANS simulations of transitional and turbulent flow. Temporally developing DNS are performed for channel flow at $Re_\tau = 180$ ($Re_H = 3300$) (Re180 henceforth) and 590 (Re_H=12656) (Re590 henceforth), and a flat-plate boundary layer flow at zero pressure gradient (FP), with different initial $Tu_{in} =$ 1% to 5%.

5.1 IDENTIFICATION OF TRANSITION ONSET MARKERS

A viable large-scale transition onset parameter for use in RANS transition-sensitive turbulence models should satisfy the following key criteria:

1) The dimensionless transition onset marker should be a function of local, statistical quantities that are available within the framework of Reynolds-averaged simulations, e.g. mean velocity gradient, turbulent kinetic energy, fluid viscosity, etc.
2) It should show a well-defined peak in the near wall region. A well-defined peak is essential, so that the onset parameter can be easily identified during simulations. The location of the peak is expected to coincide with the developing lower log layer or buffer region, where significant energy transfer from streamwise fluctuations to other components is expected via the action of the pressure strain terms.

3) The peak value should monotonically increase when the flow transitions from laminar to turbulent flow. A monotonic trend is important for modeling purposes so that there is no ambiguity regarding the continuity of the transition process from onset to fully turbulent flow. Likewise, the marker should obtain a value well above the critical value over most of the fully turbulent boundary layer, with values below the critical value only appearing in the viscous dominated region very close to the wall.
4) The critical value of the transition marker should be independent of Re and Tu_{in}, so that the onset parameter is generally applicable over a relatively wide range of flow conditions.

Key indicators of transition onset are: (a) a local minimum in the wall shear stress or friction velocity u_τ; (b) rapid growth of streamwise turbulence fluctuations u'; and (c) transfer of energy to other components v' and w'. As discussed above, studies have identified u'/U_∞, u'/u_τ, $\left(\frac{\theta^2}{\nu}\right)\left(\frac{u'}{\lambda}\right)$, and $\frac{k}{\nu\omega}$ as potential markers that obtain universal peak values at locations corresponding to these indicators. In this study, each of these except $\left(\frac{\theta^2}{\nu}\right)\left(\frac{u'}{\lambda}\right)$, along with their streamwise normal planar counterparts u'_{2D}/U_∞, u'_{2D}/u_τ, $k_{2D}/\nu\omega$, where $k_{2D} = \frac{1}{2}\left(v'^2 + w'^2\right)$ and $u'_{2D} = \sqrt{2k_{2D}}$, and local turbulent Reynolds number $\sqrt{k}y/\nu$ are investigated. The Praisner and Clark [17] formulation is not investigated due to the ambiguity in estimating the relevant local turbulence length scale.

The critical values of the onset parameters are summarized in Table 1, and their variation in pre-transition, transition and turbulent regimes are discussed below using key results in Fig. 5.5. The critical values of the parameters are identified using C_f and peak u' variation profiles. For FP, the local minimum of C_f and start of linear u'^2 growth was coincident. However, for

channel flows, u'^2 growth was found to be a better indicator of the transition onset than C_f as shown in Fig. 5.4a.

The value of u'/U_∞ showed a well-defined peak at y^+~40 for both pre-transition, transition and turbulent regions. The critical value was $u'/U_\infty \approx 14.3\pm12\%$ for both channel flow and FP simulations for the range of Tu_{in} investigated, which compares well with values reported in the literature. The marker satisfies criteria 1, 2 and 4 above, but fails to satisfy criterion 3, as its value in the turbulent region for low Tu_{in} cases is close to the critical value.

The value of u'/u_τ also shows a well-defined peak at $y^+\sim40$ in all the flow regimes like u'/U_∞. Its critical value decreases with the increase in Tu_{in} for both the channel flow and FP simulations. For Tu_{in} >2%, the critical value is $u'/u_\tau \approx 4.3$, somewhat higher that that reported by Sharma et al. [81]. In addition, its value falls below the critical value in the turbulent region. Therefore, u'/u_τ fails to satisfy criterion 3. It also fails to satisfy criterion 1 since u_τ is not easily obtained in general RANS simulations at locations away from the wall boundary.

Both u'_{2D}/U_∞ and u'_{2D}/u_τ show well defined peaks at $y^+\sim100$ close to the transition onset, and the peak moves to lower $y^+\sim60$ in the turbulent region. The peak magnitudes are small and start to grow almost exponentially at transition onset, increase monotonically throughout transition, and show quasi-steady values in the turbulent region. The values in the turbulent region are about 3 times as large as those at onset. These parameters satisfy criteria 2 and 3. But do not satisfy criterion 4, as the critical values increase with increasing Tu_{in} and show around 30% variation for the cases considered herein.

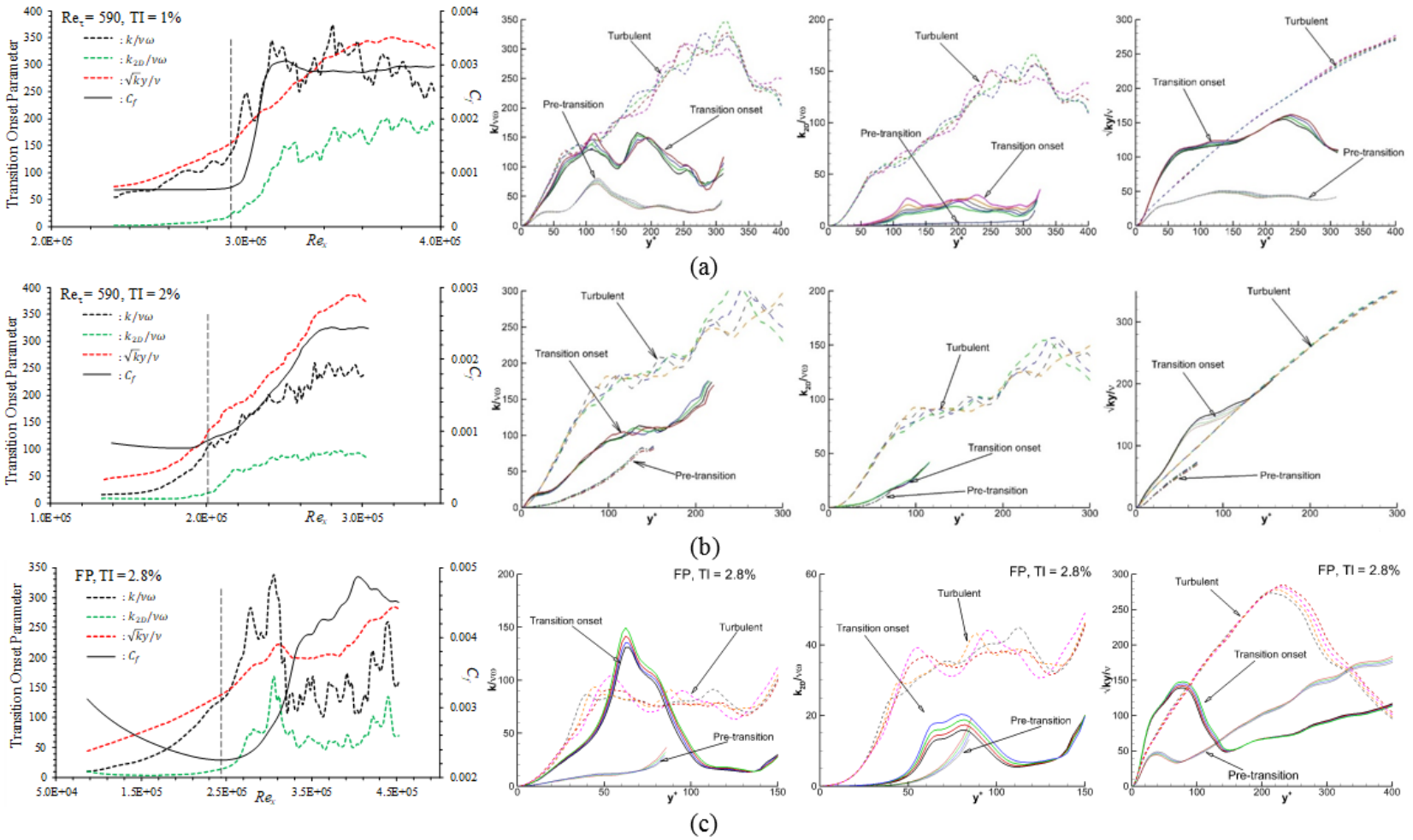

Figure 5.1 Evolution of parameters $k/\nu\omega$, $k_{2D}/\nu\omega$ and $\sqrt{k}y/\nu$ during transition (leftmost panel) and their near-wall profiles in pre-transition, transition onset, and turbulent regions. Results are presented for: (a) $Re_\tau = 590$, $Tu_{in} = 1\%$ (case #4), (b) $Re_\tau = 590$, $Tu_{in} = 2\%$ (case #5), and (c) flat-plate boundary layer, $Tu_{in} = 2.8\%$ (case #10) simulations.

The parameter $\frac{k}{\nu\omega}$ shows a well-defined peak around $y^+ \sim 60-80$ at transition onset and shows an almost constant value in the log-layer. The value increases sharply in the pre-transition region and shows quasi-steady values within $\pm 10\%$ of the critical value in the turbulent region. The critical value is $\frac{k}{\nu\omega} \approx 127 \pm 14\%$ for Re590 and FP but shows around 20% lower values for Re180. Thus, this parameter does not satisfy criterion 4 very well, and may have limitations for low-Re flows.

The peak location for the parameter $\frac{k_{2D}}{\nu\omega}$ is like that for $\frac{k}{\nu\omega}$. The peak value shows a sharp increase in the pre-transition/transition regions and shows quasi-steady values in the turbulent region that are 3-4 times larger than the critical value. The critical value of $\frac{k_{2D}}{\nu\omega} \approx 20 \pm 18\%$ for all the cases. Re180 shows somewhat smaller values than the other cases. Excluding Re180 case the critical value is $\frac{k_{2D}}{\nu\omega} \approx 22 \pm 14\%$. Overall, this parameter appears to satisfy all the criteria reasonably well but may have limitations for low-Re flows.

The parameter $\sqrt{k}y/\nu$ shows a well-defined peak at around $y^+ \sim 80$ in the pre-transition region, and the peak shifts to larger y^+ as the flow transitions. In the turbulent region, the peak is observed at $y^+ \sim 300$ for the flat-plate cases but occurs at the centerline (or peak y^+) for the channel flow cases. The critical value is $\sqrt{k}y/\nu \approx 148 \pm 18\%$ considering the average over all cases. The values are somewhat smaller for the Re180 case. Excluding Re180, the critical value is $\sqrt{k}y/\nu \approx 156 \pm 10\%$. The parameter shows a steady increase from the pre-transition to the turbulent region, where the values in the turbulent region are almost 3 times the critical value. However, the parameter only partially satisfies criterion 3, as it is apparent that values above

critical are only present in the fully turbulent boundary layer above $y^+ \sim 100$, as shown in Fig. 5.5.

Overall, all the transition onset parameters investigated satisfy some of the necessary criteria for use in RANS-based transition models. Only $\frac{k_{2D}}{\nu\omega}$ satisfies all the parameters, however even for the relatively limited set of cases tested here, there is up to 18% variation in its critical value, which may suggest limited universality over a wide range of conditions. The parameter u'/U_∞ showed the least variation in critical value for the different test cases and is consistent with transition markers that have been similarly used by several previous investigators, although its failure to satisfy criterion 3 suggests that it may be problematic for use in a single-point RANS model. Interestingly, these two parameters suggest fundamentally different mechanisms responsible for suppression of pressure-strain energy redistribution in the pre-transitional boundary layer, with the former indicating a viscous damping and the latter an inviscid effect perhaps related to wall blocking. It is recommended that future studies examine each of these parameters more closely and seek to tie their performance as a transition marker to sound phenomenological reasoning.

5.2 CONCLUSIONS

Efficacy of several large-scale flow parameters as transition onset markers was evaluated for boundary layer bypass transition using temporally evolving DNS. The reliability of the parameters as effective markers was judged based on the appearance of well-defined peaks, monotonicity of the value during transition, and independence on Tu_{in} and Re variations. Preliminary results identify parameters $\frac{k_{2D}}{\nu\omega}$ and u'/U_∞ to be potentially reliable transition onset markers. Their critical values were estimated to be $\frac{k_{2D}}{\nu\omega} \approx 22\pm14\%$ and $\frac{u'}{U_\infty} \approx 14.3\pm12\%$. Future

work will focus on investigating the underlying physical mechanisms represented by these parameters, as well as increasing the DNS database for intermediate and lower Tu_{in}, and for flows with pressure gradients. The eventual goal of the comprehensive effort is to incorporate one or more of the investigated transition markers into general-purpose physics-based RANS models for use in engineering CFD predictions of transitional flows.

CHAPTER VI

EVALUATION OF PRESSURE STRAIN IN DEVELOPING BOUNDARY LAYERS USING DNS AS A BASIS FOR PREDICTING TRANSITION ONSET

One of the open research questions for transition modeling is – how to specify or predict the onset of transition? In a previous study [82], the authors identified key important criteria a viable large-scale transition onset parameter should satisfy, and tested the ability of several heuristic large-scale markers to satisfy these criteria. The study is summarized in the following section. The study concluded that the identification of a robust transition onset marker should be based on sound phenomenological reasoning, focusing on the inspection of the upstream large-scale flow to identify traces that turbulence onset.

Mayle and Schultz [20] identified the pressure-diffusion terms as the driver of the growth of Klebanoff modes from freestream disturbance, and pressure-strain terms as the driver of the energy redistribution from the Klebanoff modes to the other components. The latter is also supported by Lardeau et al. [21], wherein it was indicated that unlike the fully developed turbulent region, the pressure-strain terms are negligible in the pre-transition regime. Walters et al. [19] hypothesized that the absence of the pressure-strain inhibits nonlinear turbulence breakdown, and is closely related to shear-sheltering, as proposed by Jacobs and Durbin [6,22].

Our current hypothesis for development of pre-transitional fluctuations in the developing boundary layer focuses on the suppression of the "return-to-isotropy" (i.e. slow) pressure-strain terms in the Reynolds stress transport equations so that they have no significant impact on the

production dynamics. This is consistent with results in the literature that show these terms to be near zero. In fact, the pressure-strain for the wall normal component should be negative (decreasing $\overline{v'^2}$) due to the kinematic wall blocking effect. Even without the presence of the wall, or in the outer region of the boundary layer, rapid distortion theory indicates that the rapid pressure strain term for the wall-normal component is negative in the limit of high shear rate. The consequence of this should be that $\overline{v'^2}$ decays very slowly after an initially rapid decay just downstream of boundary layer start, $\overline{u'v'}$ grows as approximately $Re_x^{1/2}$, and $\overline{u'^2}$ grows as Re_x. Also, the structure of the turbulence approaches single component (streamwise) as $Re_x \gg 0$. All of this corresponds very well to documented behavior of the Klebanoff modes (streaky structures) including the linear growth rate of energy.

The question we are now trying to answer is whether we can find a realistic, physically meaningful transition onset marker to determine when the breakdown to 3D turbulence begins. Our supposition is that this corresponds to the sudden growth in magnitude of the pressure-strain terms. Furthermore, since transition is known to be an inherently nonlinear process, we should assume that it is the slow pressure strain terms that are responsible. Since these terms tend to redistribute energy from highly energetic components to lower energetic components (i.e. "return-to-isotropy") this makes sense conceptually. The transition marker, then, should somehow be related to the slow pressure strain terms. Let us further assume that since transition occurs in the outer part of the boundary layer, any viscous wall effects play a limited role, i.e. transition initiation is inherently an *inviscid* phenomenon. In the outer part of the turbulent boundary layer (y+ > ~10), the rapid pressure strain terms have been shown to be negative for $\overline{v'^2}$, which is in agreement with the rapid distortion theory (RDT) result mentioned above. The

slow terms are positive in this region, dominating over the rapid terms, and are responsible for providing energy to the wall-normal component of the turbulence.

The overall objective of this study is to extend the previous research to identify a realistic, physically meaningful marker for bypass transition onset. This research specifically focuses on improving understanding of the correlation between mean and turbulence flow gradients that result in turbulent spot formation. The research builds on the hypothesis that transition initiates in the developing boundary layer at a location for which the slow part of the pressure strain term becomes more dominant than the rapid part of the pressure strain term. To achieve the objectives, temporally developing direct numerical simulation (T-DNS) are performed for bypass transition over a flat-plate at zero pressure gradients for a range of Tu_{in}. The analysis of the results focuses on: (a) validation of T-DNS predictions against spatial DNS; (b) stress budget analysis to evaluate the role of pressure-strain on transition, as identified by [20]; and (c) analyze the role of rapid and slow (return) pressure fluctuation sources on turbulence growth and redistribution to validate the research hypothesis.

6.1 ROLE OF PRESSURE STRAIN IN TRANSITION

T-DNS predictions of stress budgets for bypass transition over flat-plate boundary layer for $Tu_{in} = 3.5\%$ in the laminar, transition, and fully developed turbulent region are analyzed to understand the inter-component energy transfer.

As shown in Fig 6.1, the stress budgets in the fully developed turbulence region are similar to those from previous simulations of channel and flat-plate boundary layer flows [11,75]. The results show that $v'v'$ generation near the wall ($y^+ < 7$), or ejection events, are due to pressure-diffusion, and balanced by pressure-strain which tends to reorient wall normal fluctuations to the streamwise and spanwise directions. The turbulence energy is redistributed

from $u'u'$ to $w'w'$ and $v'v'$ via pressure-strain in the lower log-layer. Energy decay is mostly from $u'u'$ followed by $w'w'$ and least from $v'v'$. The budgets in the transition regime (not shown) show turbulence production and growth mechanisms similar to the turbulent flow. The stress budget in the laminar region (not shown) shows growth of u' fluctuations, which are the Klebanoff modes. The production of the fluctuations initiates from the interaction of the mean flow gradients with free-stream $v'v'$ to generate turbulent shear $u'v'$, and the latter further interacts with $u'v'$ to produce $u'u'$. Overall, the energy-transfer and distribution patterns emphasize that the growth of the pressure-strain term is critical for transition onset.

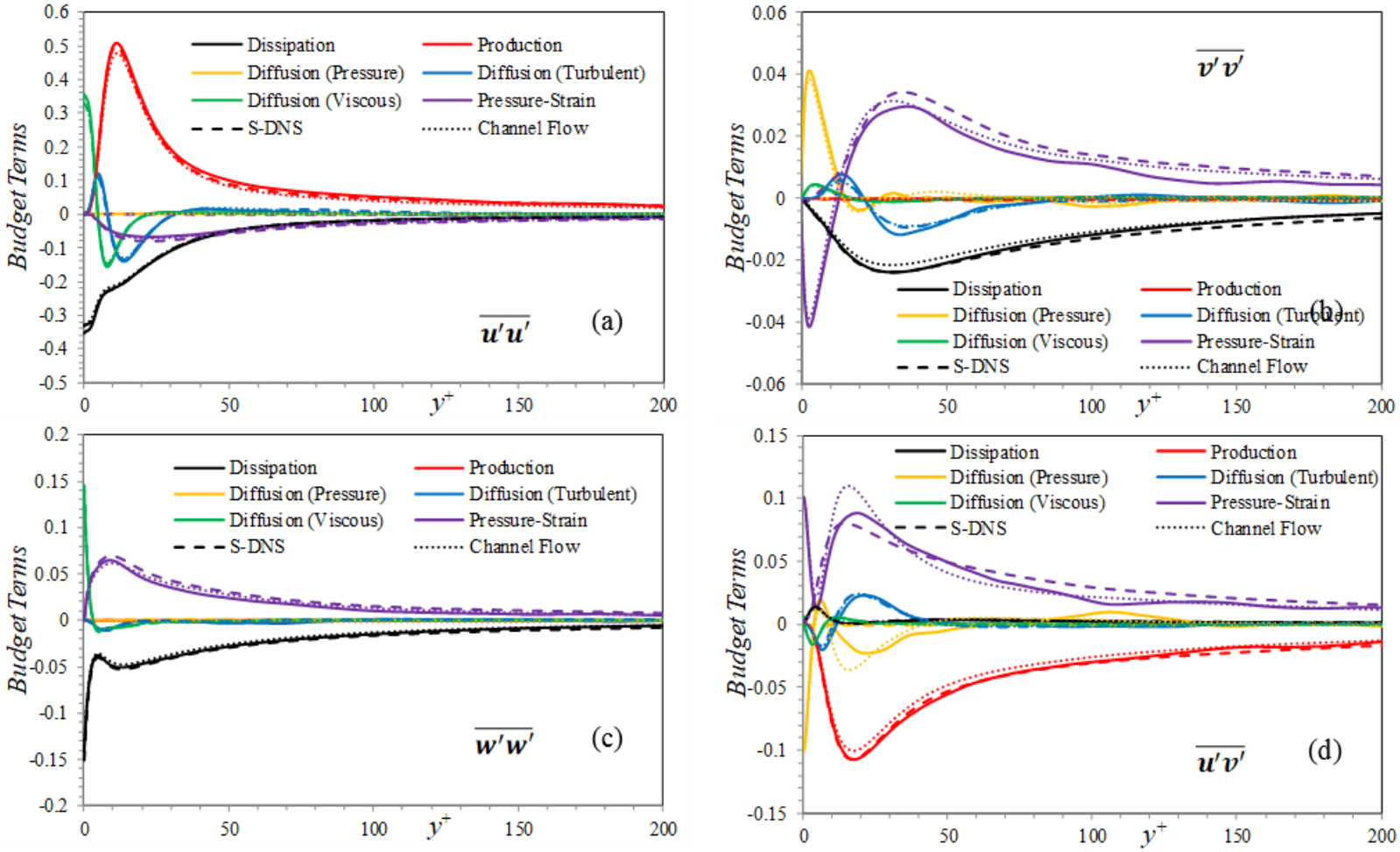

Figure 6.1 Stress budgets for: (a) $\overline{u'u'}$, (b) $\overline{v'v'}$, (c) $\overline{w'w'}$, and (d) $\overline{u'v'}$ in fully developed turbulent regime ($Re_\theta = 1100$) for flat-plate boundary layer are compared with flat plat boundary layer DNS data from Jimenez et al. [75] and channel flow DNS ($Re_\tau = 590$). All budget terms are normalized by ν/u_τ^4

The Reynolds-stress anisotropy is analyzed to emphasize the growth of three-dimensionality of turbulence during transition. The state of anisotropy is determined using the map of two variables ξ and η. The invariants ξ and η are determined from the normalized anisotropy stress tensor b_{ij} as below:

$$\begin{aligned} b_{ij} &= \frac{\langle u_i' u_j' \rangle}{2k} - \frac{1}{3} k \delta_{ij} \\ 6\eta^2 &= -2II_b = b_{ij} b_{ij} \\ 6\xi^2 &= III_b = b_{ij} b_{jk} b_{ki} \end{aligned} \tag{6.1}$$

where, $k = \frac{1}{2} \langle u_i' u_i' \rangle$

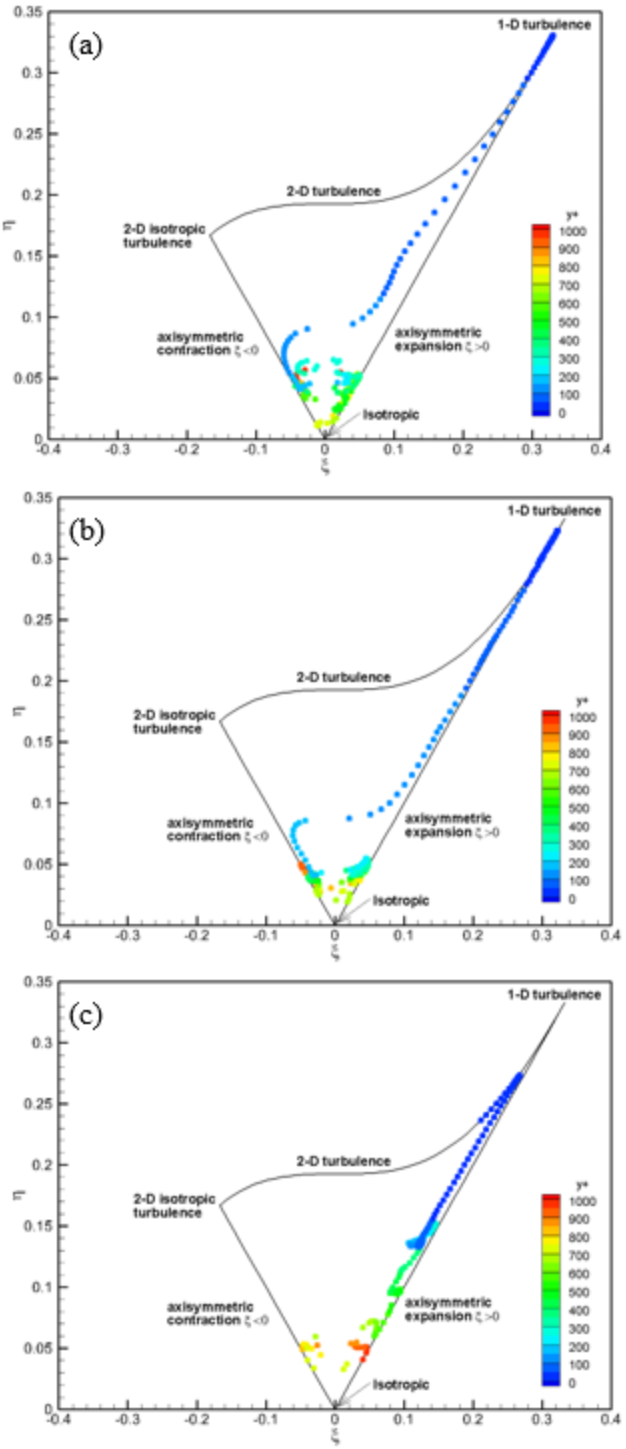

Figure 6.2 Reynolds stress invariant map of T-DNS data for bypass transition of flat plate boundary layer in the (a) laminar regime ($Re_\theta = 252$), (b) transition regime ($Re_\theta = 350$), and (c) turbulent regime ($Re_\theta = 1036$). The turbulence triangle uses the coordinate system (η, ξ) based on the second and third invariants, (II_b, III_b) of the normalized anisotropy tensor b_{ij}.

As shown in Fig. 6.2, the turbulence in the laminar region is either 1D in the boundary layer or 3D in the free-stream. The 1D nature of turbulence is because of the growth of the streamwise fluctuations. As the flow transitions, the turbulence anisotropy in the boundary layer is stretched along the axisymmetric expansion line, due to growth of the wall-normal and spanwise fluctuations. The fully developed regime shows that the turbulence is approaching isotropy in the log-layer. The invariant map in the fully developed turbulent region is consistent with those of channel flow DNS[83].

Stress budget terms for the streamwise component integrated over the entire boundary layer shed light on the effect of pressure strain terms in transition as shown in Fig. 6.3 (Primary axis). Results are shown for simulations with three different Tu_{in} ranging from 2.1 to 3.5%. Variation of C_f is shown on a secondary axis to depict the general area of transition onset. The results agree with the LES results of Voke and Yang [84] and Lardeau et al. [85] indicating that the pressure-strain term is negligible in the pretransition regime compared to the fully developed turbulent region and activates right around the transition onset location. Shear sheltering phenomenon suppresses the pressure-strain terms in the pretransitional regime. It can be further seen from Fig. 6.4. that the there is a positive pressure strain term contribution to $\overline{u'u'}$ close to the wall in the pretransitional regime which is presumed to be a wall reflection effect as it suppresses the $\overline{v'v'}$ component rather than increase it like it normally would. It is also clear from the Reynolds stress budgets that the dominant terms are mostly production and dissipation while pressure strain term is negligible except for the near-wall reflection of the wall-normal fluctuations up until its activation near the onset of transition.

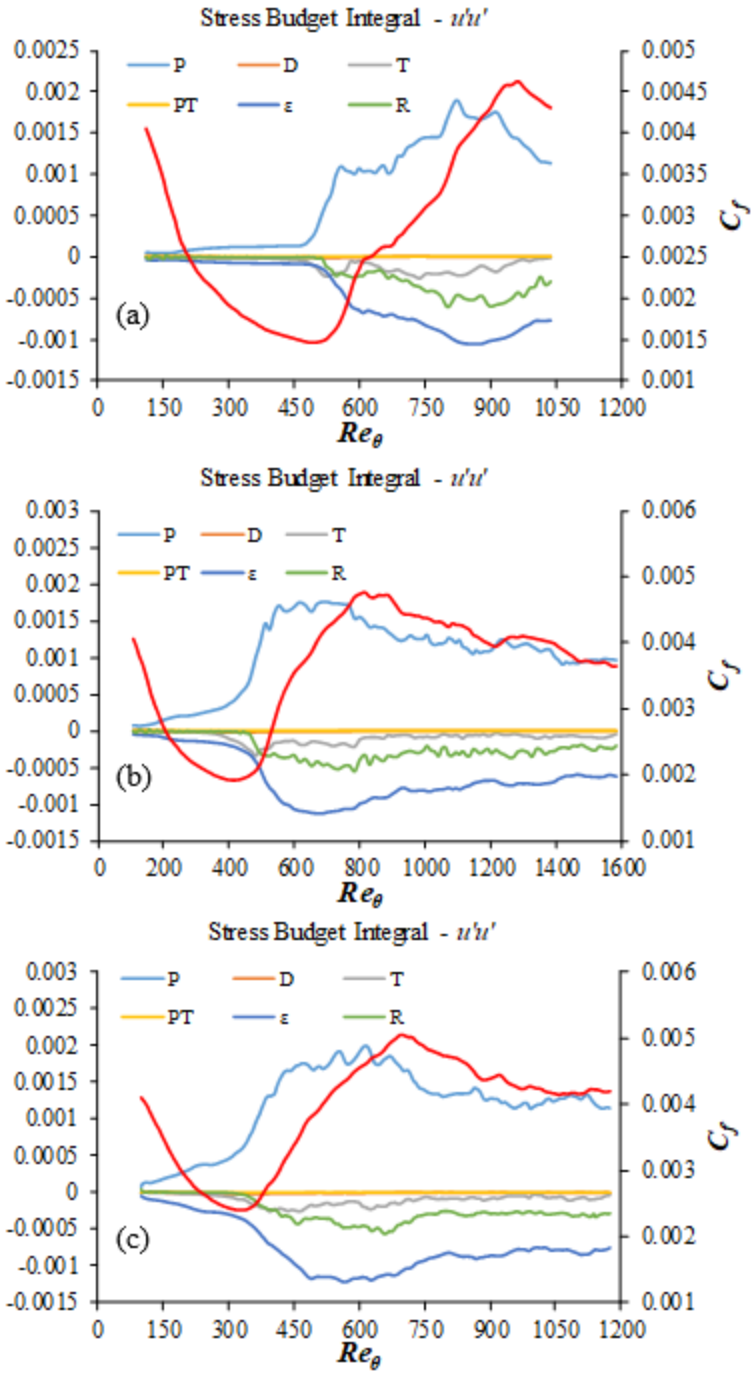

Figure 6.3 Integral of the Reynolds stress budget terms for: $\overline{u'u'}$ for flat-plate boundary layer with Tu_{in} = a) 2.1%, b) 2.8%, and c) 3.5% (Primary axis). Variation of C_f is also shown (Secondary axis).

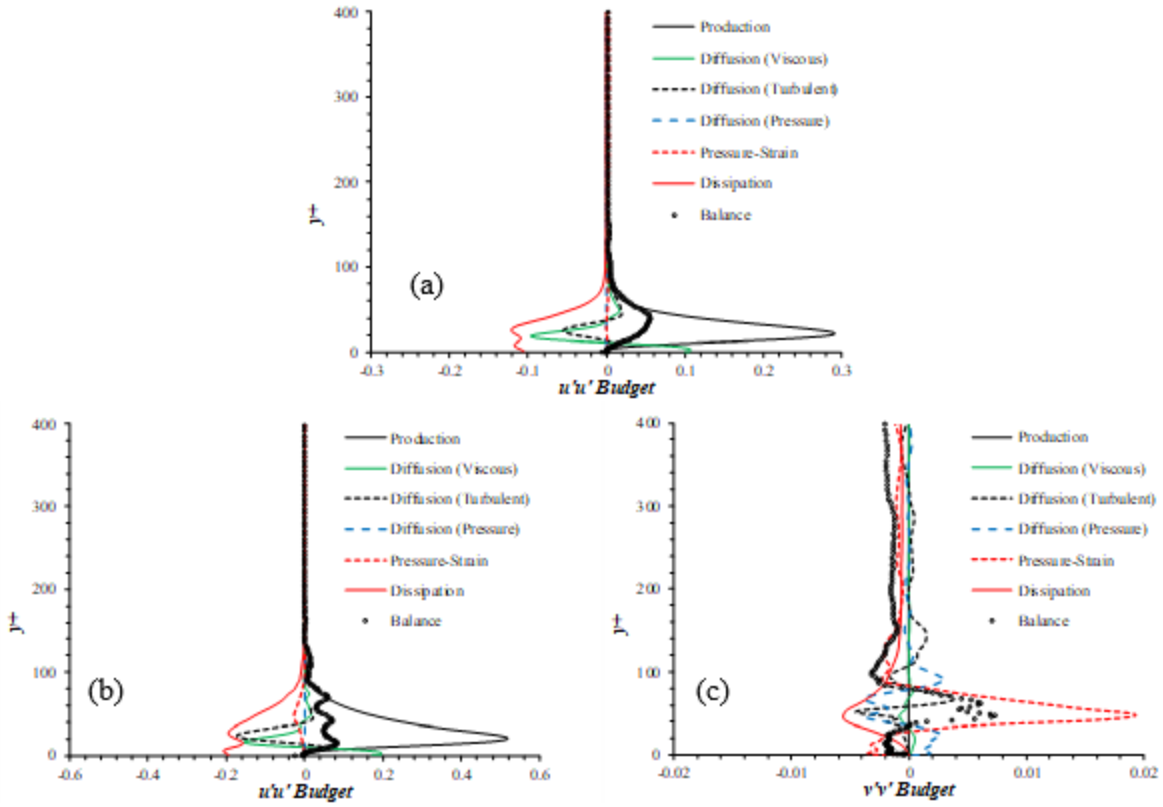

Figure 6.4 Stress budgets for a) $\overline{u'u'}$ in the pre-transitional regime $Re_\theta \approx 240$. Stress budgets for b) $\overline{u'u'}$ and c) $\overline{v'v'}$ at the onset of transition $Re_\theta \approx 330$ for flat-plate boundary layer T-DNS with $Tu_{in} = 3.5\%$.

Further examination of the integral of the streamwise and wall-normal components of the pressure strain terms shown in Fig. 6.5 for the $Tu_{in} = 3.5\%$ case shows that pressure strain terms start to become relevant right around the onset of transition as indicated by absolute minimum in the C_f also shown on the same plot. It can also be seen that the absolute magnitude of the streamwise pressure strain correlation is much larger (about two times) than the wall-normal component which is to be expected as most of the turbulent energy is in the streamwise component $u'u'$ which is then redistributed to the wall-normal, $v'v'$ and spanwise, $w'w'$ components. Also, the streamwise pressure strain correlation is negative while the wall-normal

pressure-strain correlation is positive which is also expected as energy transfer pathway is from streamwise to the wall-normal and spanwise components.

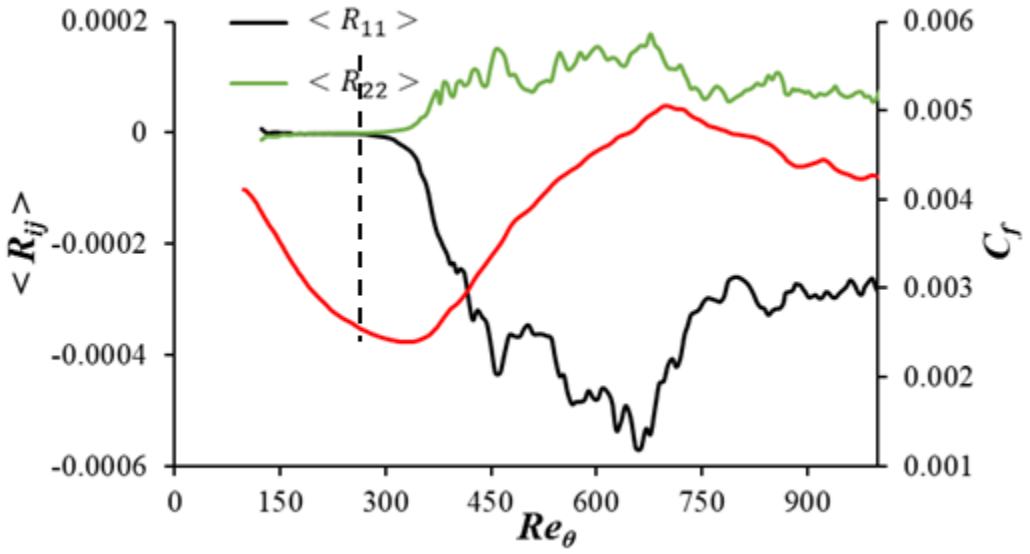

Figure 6.5 Integral of the streamwise and wall-normal pressure-strain terms for $Tu_{in} = 3.5\%$. Variation of C_f is also shown (Secondary axis) to clearly show the transition onset.

6.2 ROLE OF RAPID AND RETURN PRESSURE-STRAIN TERMS IN TRANSITION

The planar averaged values of the turbulent fluctuating velocities are analyzed in the laminar, transition, and turbulent regimes in Fig. 6.6. Results show that in the pre-transition regime nearly all the energy is oriented in the streamwise direction. The growth of the $\overline{u'_{RMS}}$ component is induced by interaction of the free-stream turbulence with the mean strain. At the onset of transition ($Re_\theta = 350$), energy is transferred from the streamwise component to the wall-normal and spanwise components. The peak $\overline{u'_{RMS}}$ occurs around $y^+ = 20$.

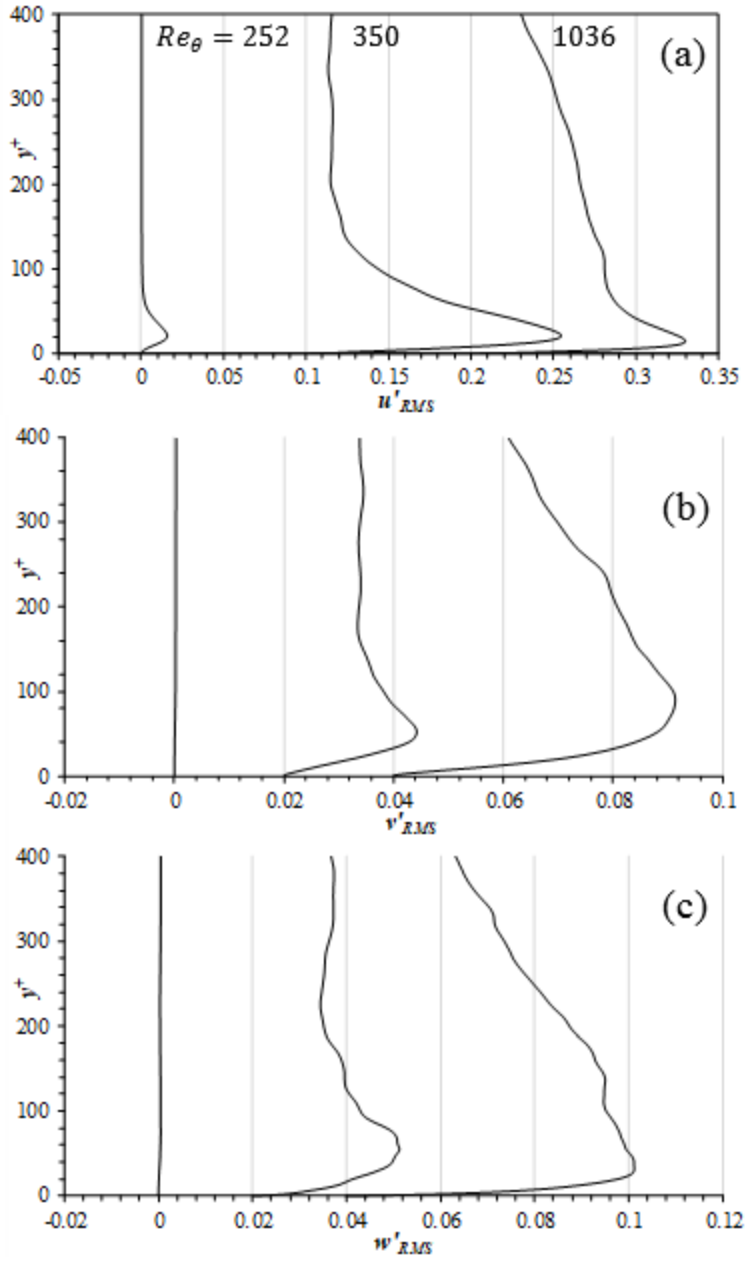

Figure 6.6 Variation of: (a) $\overline{u'_{RMS}}$, (b) $\overline{v'_{RMS}}$, and (c) $\overline{w'_{RMS}}$ versus y^+ in the laminar, transition, and turbulent regimes. Note that the plots for different Re_θ are shifted.

The governing equation for the fluctuating pressure is the Poisson equation derived from the Navier –Stokes equation for incompressible flow:

$$-\frac{1}{\rho}\nabla^2 p' = \underbrace{2\frac{\partial \bar{u}_i}{\partial x_j}\frac{\partial u_j'}{\partial x_i}}_{Rapid\ source\ term} + \underbrace{\frac{\partial^2\left(u_i'u_j'\right)}{\partial x_i \partial x_j} - \frac{\partial^2\left(\overline{u_i'u_j'}\right)}{\partial x_i \partial x_j}}_{Slow/Return\ source\ term} \tag{6.2}$$

The above equation is linear in pressure and can therefore be broken up into two parts, corresponding to the rapid and slow components. The rapid source term represents the interaction between the mean flow and the fluctuating turbulent velocity gradients and is the origin of the rapid fluctuating pressure. For the flat-plate case, when the mean flow is primarily along the streamwise direction and its gradient along the wall-normal direction is most significant, this term simplifies to $2\frac{\partial \bar{u}}{\partial y}\frac{\partial v'}{\partial x}$. The slow source term on the other hand represents the non-linear interaction between the turbulent fluctuation gradients and gives rise to the slow fluctuating pressure. For wall-bounded flows, these two parts of Eq. (6.2) is solved for with no source term and the homogeneous Neumann boundary condition at the wall, and an additional Laplace equation for the fluctuating pressure can be solved with the viscous boundary condition arising from asymptotic limiting of the Navier-Stokes equation, the solution of which are the so-called Stokes fluctuating pressure components. The solutions to each of these parts can then be superposed. We can thus express the splitting of the pressure as:

$$\begin{gathered} p' = p_r' + p_s' + p_{st}' \\ \nabla^2 p_r' = -2\rho\frac{\partial \bar{u}}{\partial y}\frac{\partial v'}{\partial x} \\ \nabla^2 p_s' = -\rho\frac{\partial}{\partial x_l \partial x_k}\left(u_k'u_l' - \overline{u_k'u_l'}\right) \\ \nabla^2 p_{st}' = 0 \end{gathered} \tag{6.3}$$

The profiles of the root-mean-square (RMS) of the rapid source term and the six slow source terms in the turbulent regime are shown in Fig. 6.6. The magnitude of $\frac{\partial v'}{\partial z}\frac{\partial w'}{\partial y}$ is the largest amongst the slow source terms and its peak is located at $y^+ \approx 18$ which coincides with the location of the centers of the streamwise vortices. The results are consistent with the observations of Chang et al. [86] and Kim [87].

The profiles of the RMS fluctuating pressure as determined by Eqs. (4-6) for the fully developed turbulent boundary layer ($Re_\theta = 1036$) are shown in Fig. 6.8.

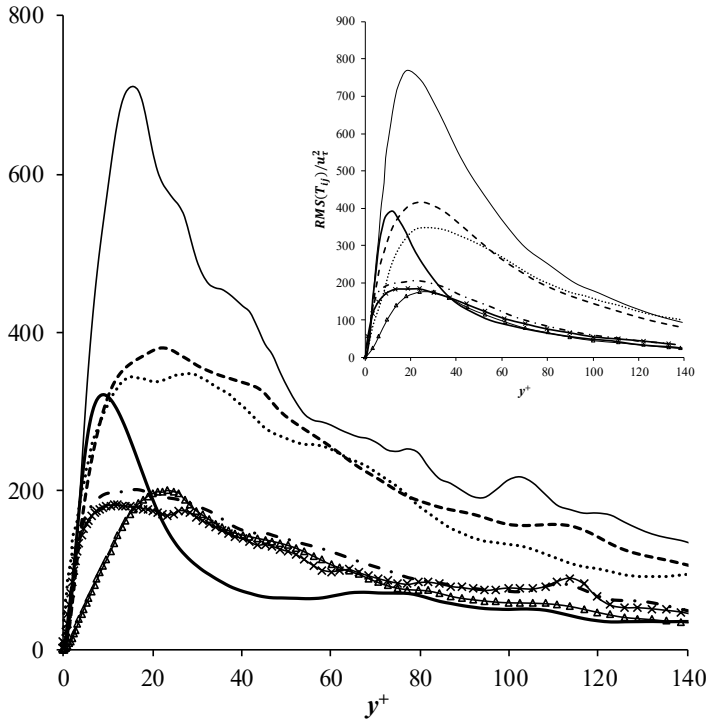

Figure 6.7 Profiles of the normalized RMS of the non-linear slow and the linear rapid source terms in the fully developed turbulent regime for flat-plate boundary layer ($Re_\theta = 1100/Re_\tau = 440$). Δ: $\left(\frac{\partial u'}{\partial x}\right)^2$; $\cdots$: $2\frac{\partial u'}{\partial y}\frac{\partial v'}{\partial x}$; ---: $2\frac{\partial u'}{\partial z}\frac{\partial w'}{\partial x}$; $\times$: $\left(\frac{\partial v'}{\partial y}\right)^2$; $-$: $2\frac{\partial v'}{\partial z}\frac{\partial w'}{\partial y}$; $-\,-$: $\left(\frac{\partial w'}{\partial z}\right)^2$; $-$: $2\frac{\partial \bar{u}}{\partial y}\frac{\partial v'}{\partial x}$. (Inset) Channel flow data of Chang et al. [86] for $Re_\tau = 180$ is also shown for comparison.

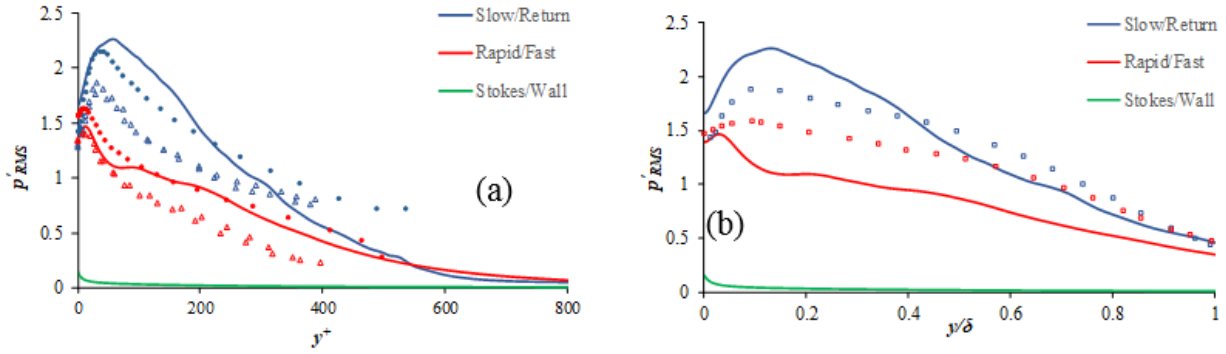

Figure 6.8 RMS of the slow, rapid, and stokes fluctuating pressure components of the pressure in the fully developed turbulent regime for flat-plate boundary layer ($Re_\theta = 1100/Re_\tau = 440$) a) v/s y^+ and b) v/s y/δ. Channel flow data of Kim [87] for $Re_\tau = 400$: Δ, Jiménez et al. [88] for $Re_\tau = 547$: ●, and turbulent boundary layer data of Hu et al. [89] for $Re_\tau = 2513$: □ are also shown for comparison.

It is quite clear from Fig. 6.8 that the Stokes part is negligible compared to the other two parts throughout the boundary layer including the near-wall region. The slow pressure is substantially higher than the rapid fluctuating pressure. The results are compared against the channel flow data of Kim [87] for $Re_\tau = 400$, Jimenez et al. [88] for $Re_\tau = 547$ and the turbulent boundary layer data of Hu et al. [89] for $Re_\tau = 2513$. It is apparent that the results fall between both of the channel flow results since $Re_\tau = 440$ for the fully developed turbulent boundary layer in the present study.

The RMS values of the slow, rapid source terms and the corresponding slow and rapid fluctuating pressure as well as the streamwise and shear stress components of the slow and rapid pressure-strain correlation are presented in the laminar, transition, and turbulent regimes in Figs. 6.9 and 6.10 to establish the role of pressure-strain terms on transition. Results show that both the slow and rapid pressure-strain terms are suppressed in the laminar/pretransition regime, start

growing near the transition onset, and are dominant throughout the transition and turbulent regimes. The peak of the slow source term at onset of transition is around $y^+ = 50$ and around $y^+ = 20$ in the fully developed turbulent region. In comparison the peak of the rapid source term at onset of transition is around $y^+ = 20$ and around $y^+ = 10$ in the fully developed turbulent region. The peak shifts as the boundary layer grows. The rapid term shows a complimentary behavior to the slow term. In the turbulent regime, the peak slow term occurs in the buffer layer.

Mean shear in the boundary layer prevents perturbation of the latter by small scales (high frequency components) in the free-stream turbulence. Viscous stresses in the buffeted boundary layer resist the free-stream perturbations and enable the boundary layer to remain laminar in the pre-transitional regime. The mean shear serves as a filter for the free-stream disturbances, ejecting the high frequency components while allowing only the low frequencies to infiltrate the boundary layer.

Freestream turbulence enters the boundary layer either at the leading edge or through diffusive transport of low frequency modes [7]. Only the $\overline{v'v'}$ component of this leads to the growth of the Klebanoff modes (pretransitional energy production) with no apparent growth of $\overline{v'v'}$ and $\overline{w'w'}$ itself. Production of one-dimensional streamwise fluctuation energy can be understood as interaction of the entrained free-stream turbulence with mean shear.

The role of pressure source terms on the initiation of the turbulent spots is studied using the 3D volume solutions. The flow in the laminar regime shows alternate high- and low-speed streaks aligned with the streamwise direction (figure not shown). These streaks were accompanied by counter-rotating longitudinal vortical structures, and the characteristics of the streaks (namely their spanwise spacing and peak wall normal location of the peak u'_{RMS}) are consistent with those of Klebanoff modes [69].

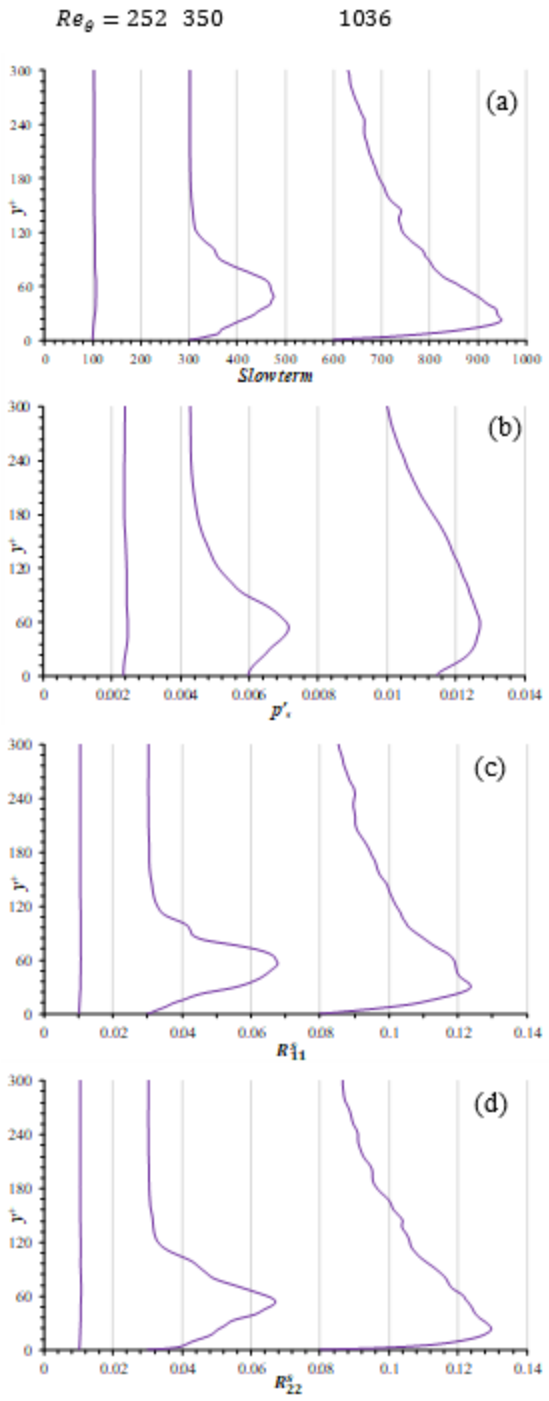

Figure 6.9 Variation of RMS of (a) slow source term (b) p'_s, (c) R^s_{11}, and (d) R^s_{22} versus y^+ in the laminar, transition, and turbulent regimes. Note that the plots for different Re_θ are shifted.

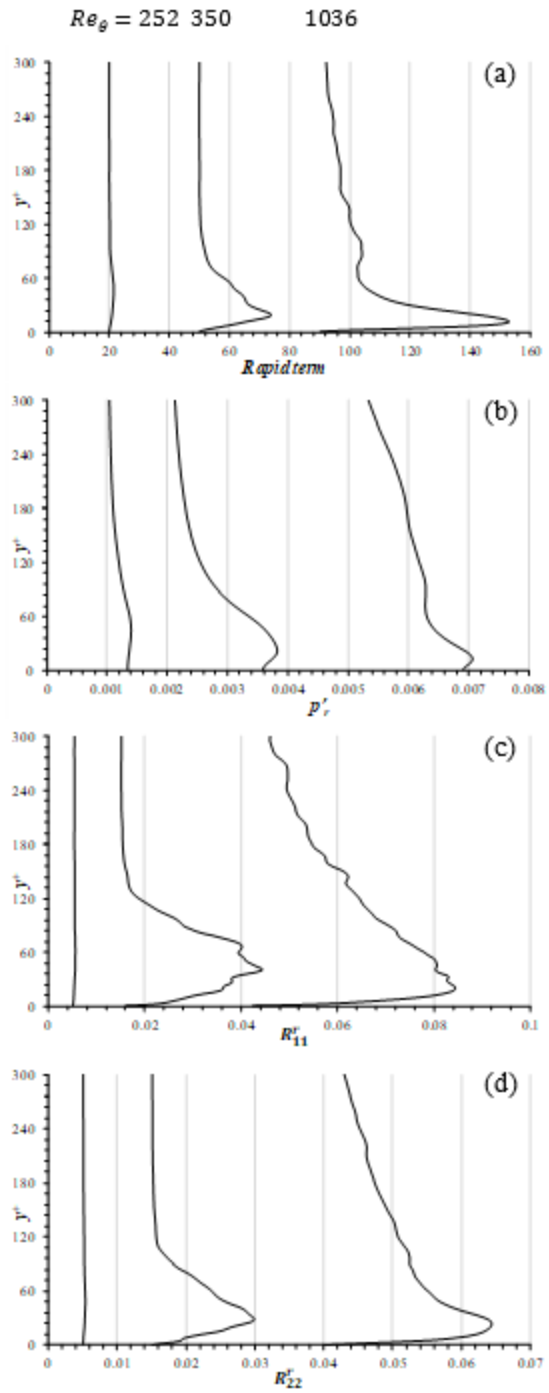

Figure 6.10 Variation of RMS of (a) rapid source term (b) p'_r, (c) R^r_{11}, and (d) R^r_{22} versus y^+ in the laminar, transition, and turbulent regimes. Note that the plots for different Re_θ are shifted.

The peaks of the slow and rapid streamwise and wall-normal components of the pressure-strain correlation exhibit a behavior consistent with their fluctuating pressure source terms respectively. Figs. 6.9 and 6.10 show that the peak RMS value of both the slow and rapid fluctuating pressure source terms, and their corresponding pressure and pressure-strain components, occur in the boundary layer.

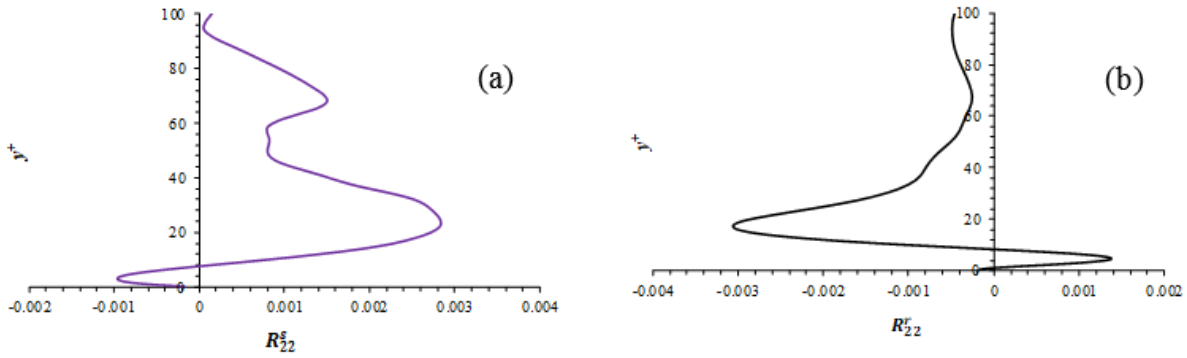

Figure 6.11 Variation of planar averaged values of (a) R_{22}^s, and (d) R_{22}^r versus y^+ in the fully developed turbulent regime $Re_\theta = 1036$.

The working hypothesis is used as the basis to identify a physically meaningful transition onset marker to determine when the breakdown to 3D turbulence begins is that this corresponds to the sudden growth in magnitude of the pressure-strain terms. Since transition is known to be an inherently nonlinear process, we assume that it is the slow pressure-strain terms that are responsible. These terms tend to redistribute energy from highly energetic components to lower energetic components (i.e. "return-to-isotropy"). From Fig. 6.11. it can be seen that in the outer part of the turbulent boundary layer ($y^+ > \sim 10$), the rapid pressure-strain terms for ($v'v'$) are negative which is in agreement with rapid distortion theory (RDT). The slow pressure-strain

terms are positive in this region, dominating over the rapid terms, and are responsible for providing energy to the wall-normal component of the turbulence. The transition marker, therefore, should somehow be related to the slow pressure-strain terms.

A critical ratio for the fluctuating pressure source term (Poisson equation), the fluctuating pressure, and the pressure-strain correlation is defined based on their peak RMS values in the boundary layer as follows:

$$C_{source} = \left|\frac{Slow - Rapid}{Rapid}\right| \qquad C_{p'} = \left|\frac{p'_s - p'_r}{p'_f}\right| \qquad C_{R_{ij}} = \left|\frac{R^s_{ij} - R^r_{ij}}{R^r_{ij}}\right| \tag{6.4}$$

For the flat plate boundary layer, the local minimum of the skin friction coefficient, C_f, was used as an indicator of the transition onset. The variation of the critical ratios in the pretransition, transition, and turbulent regimes with various Tu_{in} is shown in Fig. 6.12 and discussed below.

A local minimum in C_f can be observed at $Re_\theta = 333$, $Re_\theta = 435$ and $Re_\theta = 480$ for the flat plat boundary layer results with different $Tu_{in} = 3.5\%$, $Tu_{in} = 2.8\%$, and $Tu_{in} = 2.1\%$ respectively. It is also observed that all four critical ratios exhibit a clear peak at the same Re_θ location for all three Tu_{in} considered in the present study. Appropriate normalization for any future transition marker based on the critical ratios presented in this study has to be developed to ensure that the marker is independent of Re and Tu_{in}.

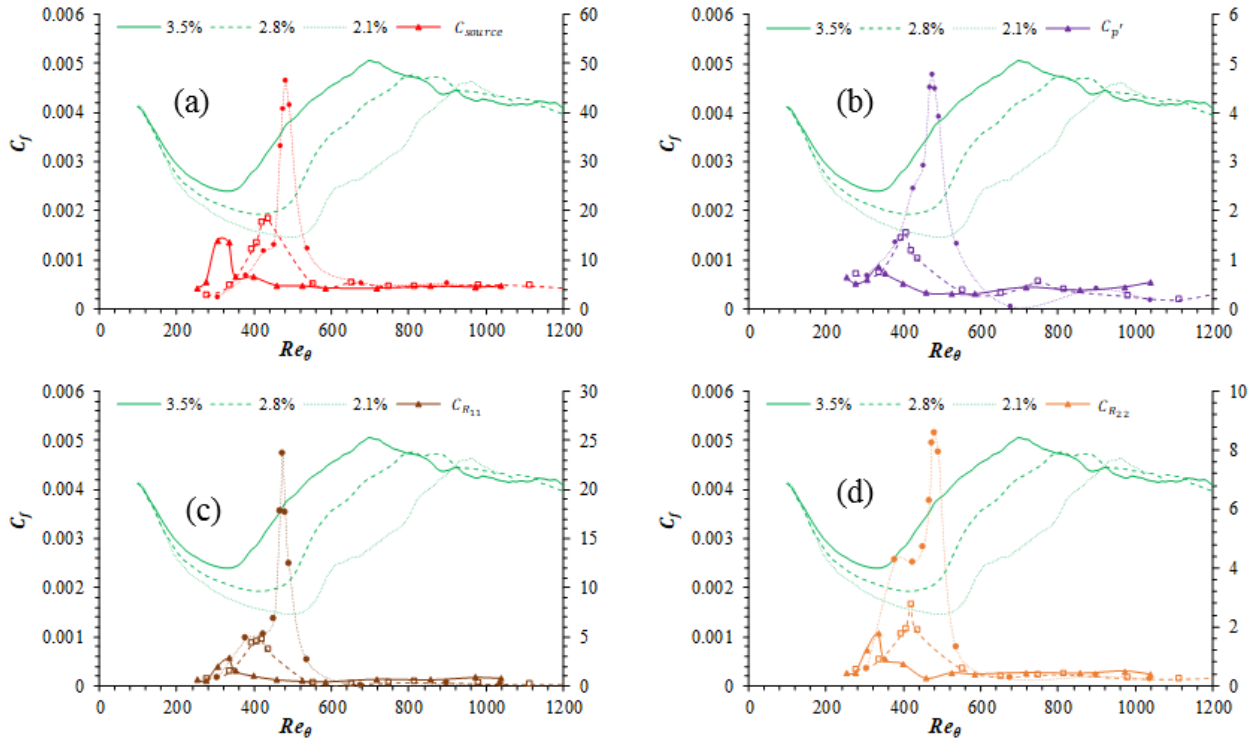

Figure 6.12 Variation of C_f with Re_θ for different Tu_{in} (Primary axis) showing the local minimum (transition onset location). Variation of the (a) critical ratio of fluctuating pressure source term C_s, (b) critical ratio of fluctuating pressure $C_{p'}$, (c) critical ratio of streamwise pressure-strain correlation $C_{R_{11}}$, and (d) critical ratio of wall-normal pressure-strain correlation $C_{R_{22}}$(Secondary axis) versus Re_θ.

Suppression of the pressure strain terms in the pretransitional regime can thus be understood to prevent breakdown of the boundary layer into fully 3-d turbulence. Transition initiation then can be seen as due to an increase in magnitude of the pressure strain terms – transfer of energy from $\overline{u'u'}$ to $\overline{v'v'}$ and $\overline{w'w'}$ which are salient futures of fully turbulent flow.

Evolution of the wall normal component of the rapid and pressure strain terms integrated over the entire boundary layer for the $Tu_{in} = 3.5\%$ case is shown in Figure 6.13 to depict the role of pressure strain terms on the onset of transition. Evolution of C_f is also shown in the same

figure. Transition onset as determined by the C_f minimum is around $Re_\theta = 330$. It can be seen that both the rapid and return pressure strain terms start increasing in magnitude right about in the vicinity of transition. It can be also be seen that overall the return pressure strain term is always positive and grows more rapidly after transition onset while the rapid pressure strain term is negative when integrated over the boundary layer.

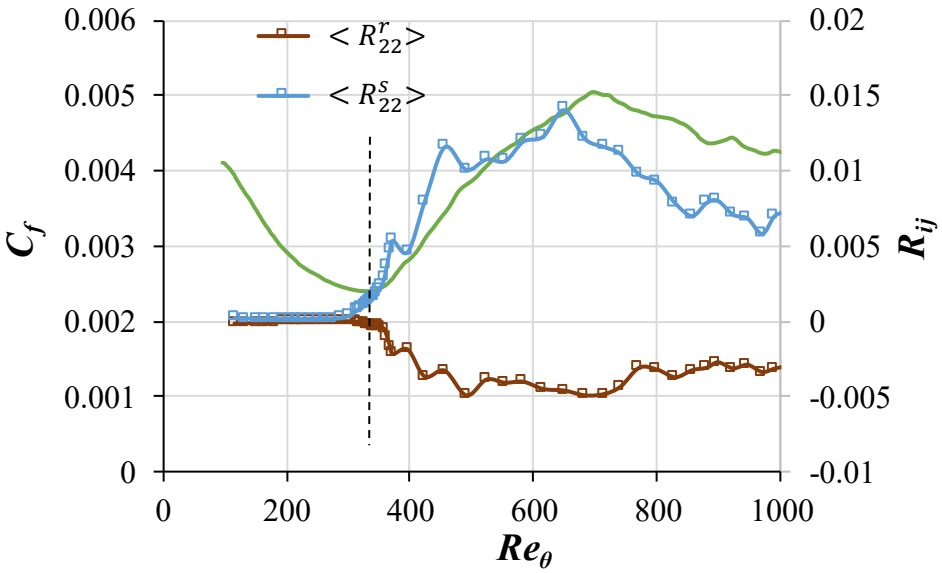

Figure 6.13 Integral of the rapid and return pressure strain terms for: $\overline{v'v'}$ for flat-plate boundary layer with $Tu_{in} = 3.5\%$ (Secondary axis). Variation of C_f is also shown (Primary axis).

Further by looking at the wall-normal profiles of the planar-averaged wall-normal rapid and return pressure strain terms in the pre-transitional regime as well as the transition and fully developed turbulent regimes in Figure 6.14 illustrates the shear sheltering effect. It can be seen that in the pre-transitional regime the rapid pressure strain terms have an equal and opposite effect to the return pressure strain terms thus blocking the return pressure strain terms from

redistributing energy from the streamwise to the wall -normal and spanwise components. At the onset of transition, the return pressure strain terms dominate over the rapid pressure strain terms thus energy redistribution initiates between the various fluctuating velocity components.

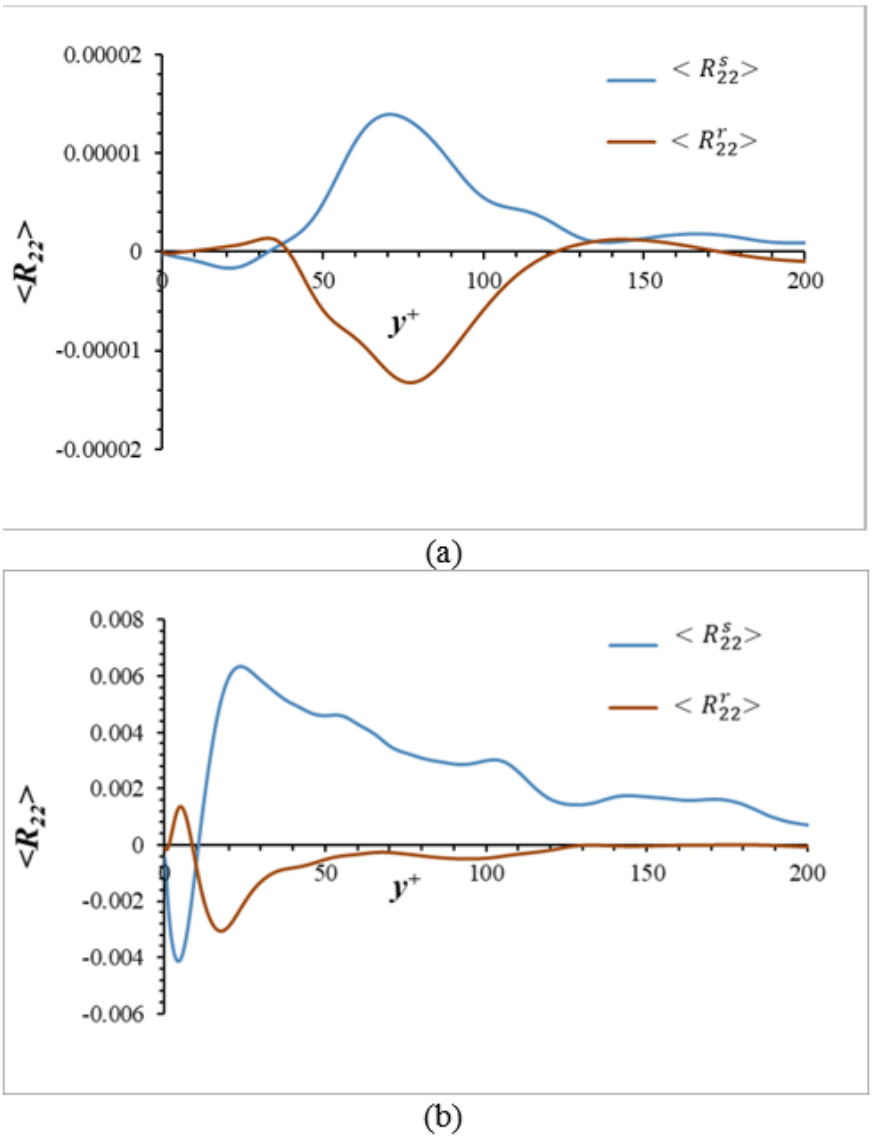

Figure 6.14 Wal-normal profiles of the rapid and return pressure strain terms for: $\overline{v'v'}$ for flat-plate boundary layer with $Tu_{in} = 3.5\%$ in the a) pre-transitional regime $Re_\theta = 200$ and the b) fully-developed turbulent regime $Re_\theta = 1036$

Future studies will focus on development of a phenomenological transition onset marker based on the pressure-strain correlation which satisfies the conditions identified in the previous study [82].

6.3 SCALING ANALYSIS – NEW TRANSITION ONSET MARKER

The slow and rapid fluctuations are solutions to the first two equations in Eq. (6.2) above, respectively. We use scaling arguments rather than the exact solution to find a relevant transition marker since the mean flow will provide us information about them. Let us then make one more modification to our hypothesis based on our analysis in the previous section (Figure 6.12) critical ratios for the source terms as well as the pressure fluctuations shown a peak at the Re_θ location which corresponds to the C_f minimum for all three Tu_{in} considered. Our hypothesis now becomes: *Transition initiates in the developing boundary layer at a location for which the fluctuating source term in the governing equation for slow pressure fluctuations becomes large relative to the fluctuating source term in the governing equation for rapid pressure fluctuations.*

Taking the relevant parts of the RHS of Poisson equation for the return and rapid pressure fluctuations from Eq. (6.2), our hypothesis then is that transition starts when the following ratio reaches a critical value:

$$\frac{\partial(u_k' u_l')}{\partial x_l \partial x_k} \Big/ \frac{\partial v'}{\partial x}\frac{\partial \bar{u}}{\partial y} \tag{6.5}$$

We define the following characteristic scaling parameters:

u'~ characteristic streamwise fluctuation magnitude

v'~ characteristic wall-normal fluctuation magnitude

ℓ_x~ characteristic streamwise fluctuation length scale

$\ell_y \sim$ characteristic wall-normal fluctuation length scale

$\Omega = \frac{\partial \bar{u}}{\partial y} \sim$ mean vorticity magnitude

From the fluctuating continuity equation, the following is assumed using the above scaling:

$$\frac{u'}{\ell_x} \sim \frac{v'}{\ell_y}$$

Substitution into source terms for the fluctuating pressure parts, Eq. (6.2) yields:

$$\begin{gathered} \frac{\partial(u_k' u_l')}{\partial x_l \partial x_k} \sim \frac{u'}{\ell_x}\frac{u'}{\ell_x} \sim \frac{v'}{\ell_y}\frac{v'}{\ell_y} \sim \frac{u'}{\ell_x}\frac{v'}{\ell_y} \\ \frac{\partial v'}{\partial x}\frac{\partial \bar{u}}{\partial y} \sim \frac{v'}{\ell_x}\Omega \end{gathered} \tag{6.6}$$

From this we find the ratio of the two terms scales as:

$$\frac{\partial(u_k' u_l')}{\partial x_l \partial x_k} \Big/ \frac{\partial v'}{\partial x}\frac{\partial \bar{u}}{\partial y} \sim \frac{u'}{\ell_y \Omega} \tag{6.7}$$

Finally, if we assume that the characteristic wall-normal fluctuation length scale is proportional to wall distance, and noting that in the pre-transitional boundary layer the turbulent kinetic energy $k \sim \frac{2}{3}u'^2$ then we have the following as a transition marker, i.e. we assume transition initiates when this quantity reaches a critical value:

$$\frac{u'}{y\Omega} \sim \frac{\sqrt{k}}{y\Omega} \tag{6.8}$$

Interestingly, for any dimensionless vertical location in the flat plate laminar boundary layer (i.e. for any value of y/δ), the value of $y\Omega$ does not vary with streamwise location and is proportional to the freestream velocity U. So, the local marker $\frac{\sqrt{k}}{y\Omega}$ is a proxy for $\frac{u'}{U}$, and the above hypothesis perhaps provides some phenomenogical underpinning for the success of that particular quantity as a transition indicator in so many previous studies and in our own results.

6.4 CONCLUSIONS

Temporally developing direct numerical simulations are performed for bypass transition of a zero pressure gradient flat plate boundary layer to improve understanding of the interplay between pressure-strain terms and flow instability mechanisms to propose and validate a phenomenological hypothesis for the identification of a robust transition onset marker for use in transition-sensitive Reynolds-averaged Navier-Stokes (RANS) computational fluid dynamics (CFD) simulations.

To achieve this objective, T-DNS predictions with free-stream turbulence $Tu_{in} = 3.5\%$ were first validated against spatially developing DNS. Following that stress budget analysis was performed to evaluate the role of pressure-strain on transition growth. Finally, the role of rapid and slow pressure-strain terms on the initiation of turbulence onset was analyzed to validate the research hypothesis.

The results demonstrate that the slow pressure-strain terms are responsible for the inter-component turbulence energy transfer from the streamwise component to other components, and this initiates at the transition onset. Once the turbulence is triggered, the rapid pressure-strain term compliments the slow term and accounts for the transfer of the energy from the mean flow to the turbulent flow.

Overall, the results validate the underlying hypothesis of the study that the transition initiates at a location for which the slow part of the pressure-strain term becomes more dominant than the rapid part of the pressure-strain term. Future work will focus on an analysis of the relative magnitudes of the rapid and slow source terms, rapid and slow fluctuating pressures and the corresponding pressure-strain components during the flow evolution. The scaling of the pressure-strain terms provides a physically meaningful large-scale parameter, $\frac{\sqrt{k}}{y\Omega}$ that can be used as a transition onset marker for RANS simulations.

CHAPTER VII

CONCLUSIONS AND FUTURE WORK

7.1 CONCLUSIONS

Computational issues associated with temporally developing simulations for bypass transition flow were investigated using DNS of flat-plate boundary layer under zero pressure gradient. The temporal simulations predict the growth of near-wall Klebanoff modes in the laminar regime, their subsequent breakdown in the transition regime, and the generation of counter-rotating quasi-streamwise and hair-pin structures in the turbulent regime. The optimal domain size for T-DNS is dictated by streamwise periodicity errors due to spatial correlation on smaller domains and boundary layer growth on larger domains. A domain size of $30\delta_0$ is identified to be the optimal domain size for simulation with $Tu_{in} = 2.1\%$ to 3.5%, but larger domains are required for a lower Tu_{in}. A formulation of the domain translation velocity was derived from the momentum integral turbulent boundary layer equations. The domain velocity was found to be the same both for the boundary layer growth and free-stream decay and the formulation was found to be robust for a range of Tu_{in}.

The growth of mean and turbulent flow in the boundary layer and free-stream decay predictions compared well with the spatial DNS and experimental data in both boundary layer and plate coordinates. The temporal simulations required 20 times smaller streamwise domain size compared to spatial DNS for $Tu_{in} = 3.5\%$. The domain size requirements for the temporal approach are expected to be even smaller for lower Tu_{in}. Overall, results demonstrate that the

temporal approach can accurately predict the interaction between the turbulent boundary layer and free-stream turbulence and is a viable inexpensive alternative to the spatial approach for bypass transition simulations focusing on flow physics analysis.

The temporally developing simulations involve the following two limitations. (1) They may have limitations in accurately resolving the near-wall Klebanoff streaks, as they extend up to breakdown, and periodicity assumption is not applicable. However, for sufficiently large domains the above limitation does not significantly affect the prediction. (2) The simulation does not allow for ensemble averaging similar to spatially developing simulations. The time-window averaging along with planar averaging over homogenous directions does significantly improve the convergence of turbulent statistics. The T-DNS simulations are intended for evaluation of transition onset markers[80], and for such cases planar and window averaging is sufficient. However, the most accurate way to achieve ensemble averaging is to perform multiple simulations with different initial conditions. The use of multiple simulations though is expected to increase the computational expense of the temporal approach, and adversely affect the advantages of the temporal approach over spatial approach.

Efficacy of several large-scale flow parameters as transition onset markers was evaluated for boundary layer bypass transition using temporally evolving DNS. The reliability of the parameters as effective markers was judged based on the appearance of well-defined peaks, monotonicity of the value during transition, and independence on Tu_{in} and Re variations. Preliminary results identify parameters $\frac{k_{2D}}{\nu\omega}$ and u'/U_∞ to be potentially reliable transition onset markers. Their critical values were estimated to be $\frac{k_{2D}}{\nu\omega} \approx 22\pm14\%$ and $\frac{u'}{U_\infty} \approx 14.3\pm12\%$.

Temporally developing direct numerical simulations are performed for bypass transition of a zero pressure gradient flat plate boundary layer to improve understanding of the interplay between pressure-strain terms and flow instability mechanisms to propose and validate a phenomenological hypothesis for the identification of a robust transition onset marker for use in transition-sensitive Reynolds-averaged Navier-Stokes (RANS) computational fluid dynamics (CFD) simulations.

To achieve this objective, T-DNS predictions with free-stream turbulence $Tu_{in} = 3.5\%$ were first validated against spatially developing DNS. Following that stress budget analysis was performed to evaluate the role of pressure-strain on transition growth. Finally, the role of rapid and slow pressure-strain terms on the initiation of turbulence onset was analyzed to validate the research hypothesis.

The results demonstrate that the slow pressure-strain terms are responsible for the inter-component turbulence energy transfer from the streamwise component to other components, and this initiates at the transition onset. The rapid pressure strain term plays a role of shear sheltering in the pre-transitional regime counteracting the return pressure strain term and thus preventing the breakdown into 3-D turbulence which is a critical aspect for onset of transition to turbulence. Once the turbulence is triggered, the return/slow pressure-strain term dominates the rapid term and accounts for the transfer of the energy from the mean flow to the turbulent flow.

Overall, the results validate the underlying hypothesis of the study that the transition initiates at a location for which the slow part of the pressure-strain term becomes more dominant than the rapid part of the pressure-strain term. The scaling of the pressure-strain terms provides a physically meaningful large-scale parameter, $\frac{\sqrt{k}}{y\Omega}$ that can be used as a transition onset marker for

RANS simulations and it needs to be further evaluated to test its efficacy in RANS transition simulations.

7.2 FUTURE WORK

- Investigate the underlying physical mechanisms represented by $\frac{\sqrt{k}}{y\Omega}$.
- Increase the DNS database for flows with adverse and favorable pressure gradients and extend the investigation for the behavior of physics based markers for such flows.
- Implement the pressure-strain based transition onset marker $\frac{\sqrt{k}}{y\Omega}$ in RANS transition simulations.

REFERENCES

[1] Morkovin, M. V., 1969, "On the Many Faces of Transition," *Viscous Drag Reduction*, pp. 1–31.

[2] Luchini, P., 2000, "Reynolds-Number-Independent Instability of the Boundary Layer over a Flat Surface: Optimal Perturbations," Journal of Fluid Mechanics.

[3] Spalart, P. R., and Venkatakrishnan, V., 2016, "On the Role and Challenges of CFD in the Aerospace Industry," Aeronautical Journal, **120**(1223), pp. 209–232.

[4] Wu, X., and Durbin, P. A., 2001, "Evidence of Longitudinal Vortices Evolved from Distorted Wakes in a Turbine Passage," Journal of Fluid Mechanics, **446**, pp. 199–228.

[5] Duan, L., 2014, "Direct Numerical Simulation of Turbulence in a Swept-Wing Boundary Layer," Journal of Fluid Mechanics, **630**, pp. 1–12.

[6] Jacobs, R. G., and Durbin, P. A., 2001, "Simulations of Bypass Transition," Journal of Fluid Mechanics, **428**, pp. 185–212.

[7] Zaki, T. A., and Durbin, P. A., 2005, "Mode Interaction and the Bypass Transition Route to Transition," Journal of Fluid Mechanics, **531**(85–111), pp. 85–111.

[8] Bose, R., and Durbin, P. A., 2016, "Helical Modes in Boundary Layer Transition," Physical Review Fluids, **1**(7), p. 073602.

[9] Schlatter, P., Brandt, L., de Lange, H. C., and Henningson, D. S., 2008, "On Streak Breakdown in Bypass Transition," *Physics of Fluids*, p. 101505.

[10] Schlatter, P., Örlü, R., Li, Q., Brethouwer, G., Fransson, J. H. M., Johansson, A. V, Alfredsson, P. H., and Henningson, D. S., 2009, "Turbulent Boundary Layers up to Reθ= 2500 Studied through Simulation and Experiment," Physics of Fluids, **21**(5), p. 51702.

[11] Moser, R., Kim, J., and Mansour, N., 1999, "Direct Numerical Simulation of Turbulent Channel Flow up to Reτ= 590," Physics of fluids, **11**(4), pp. 943–945.

[12] Akhavan, R., Ansari, A., Kang, S., and Mangiavacchi, N., 2000, "Subgrid-Scale Interactions in a Numerically Simulated Planar Turbulent Jet and Implications for Modelling," Journal of Fluid Mechanics, **408**, pp. 83–120.

[13] Bhushan, S., Warsi, Z., and Walters, D., 2006, "Estimating Backscatter in Subgrid Scale Turbulence through Algebraic Modeling," AIAA Journal, **44**(4), pp. 837–847.

[14] Bhushan, S., and Walters, D. K., 2012, "A Dynamic Hybrid Reynolds-Averaged Navier Stokes – Large Eddy Simulation Modeling Framework A Dynamic Hybrid Reynolds-Averaged Navier Stokes – Large Eddy Simulation Modeling Framework," Physics of Fluids, **015103**, pp. 1–7.

[15] Kubacki, S., Lodefier, K., Zarzycki, R., Elsner, W., and Dick, E., 2009, "Further Development of a Dynamic Intermittency Model for Wake-Induced Transition," Flow, Turbulence and Combustion, **83**(4), pp. 539–568.

[16] Walters, D. K., and Cokljat, D., 2008, "A Three-Equation Eddy-Viscosity Model for Reynolds-Averaged Navier–Stokes Simulations of Transitional Flow," Journal of Fluids Engineering, **130**(12), p. 121401.

[17] Praisner, T. J., and Clark, J. P., 2007, "Predicting Transition in Turbomachinery—Part I: A Review and New Model Development," Journal of Turbomachinery, **129**(1), p. 1.

[18] Singer, B. A., 1994, "Modeling the Transition Region," *Special Course on Progress in Transition Modelling*, pp. 7/1-33.

[19] Walters, D., 2009, "Physical Interpretation of Transition-Sensitive RANS Models Employing the Laminar Kinetic Energy Concept," ERCOFTAC Bulletin, **80**.

[20] Mayle, R. E., and Schulz, A., 1996, "The Path to Predicting Bypass Transition," *Volume 1: Turbomachinery*, p. V001T01A065.

[21] Lardeau, S., Li, N., and Leschziner, M. A., 2007, "Large Eddy Simulation of Transitional Boundary Layers at High Free-Stream Turbulence Intensity and Implications for RANS Modeling," Journal of Turbomachinery.

[22] Jacobs, R. G., and Durbin, P. A., 1998, "Shear Sheltering and the Continuous Spectrum of the Orr-Sommerfeld Equation," Physics of Fluids, **10**(8), pp. 2006–2011.

[23] Mandal, A., Venkatakrishnan, L., and Dey, J., 2010, "A Study on Boundary-Layer Transition Induced by Free-Stream Turbulence," Journal of Fluid Mechanics, **660**, pp. 114–146.

[24] He, S., and Seddighi, M., 2013, "Turbulence in Transient Channel Flow," Journal of Fluid Mechanics, **715**(60–102), pp. 60–102.

[25] Vaughan, N. J., and Zaki, T. A., 2011, "Stability of ZPG Boundary Layer Distorted by Klebanoff Streaks," Journal of Fluid Mechanics, **681**, pp. 116–153.

[26] Roach, P. E., and Brierley, D. H., 1990, "The Influence of a Turbulent Freestream on Zero Pressure Gradient Transitional Boundary Layer Development. Part 1: Test Cases T3A and T3B," *In Numerical Simulation of Unsteady Flows and Transition to Turbulence (Ed. O. Pironneau, W. Rodi, I. L. Ryhming, A. M. Savill & T. V. Truong)*, Cambridge University Press, pp. 319–347.

[27] Arnal, D., Casalis, G., and Houdeville, R., 2008, "Practical Transition Prediction Methods: Subsonic and Transonic Flows," VKI Lectures Series Advances in Laminar-Turbulent Transition Modelling.

[28] Dick, Eds. E; Elsner, W., 2009, "Transition Modeling," ERCOFTAC Bulletin, **80**.

[29] Vermeersch, O., and Arnal, D., 2009, "Bypass Transition Induced by Roughness Elements: Predictions Using A Model Based on Klebanoff Modes Amplification," ERCOFTAC Bulletin 80, **80**, pp. 87–90.

[30] Schobeiri, M., and Wright, L., 2003, "Advances in Unsteady Boundary Layer Transition Research, Part I: Theory and Modeling," International Journal of Rotating Machinery, **9**(1), pp. 1–9.

[31] Mayle, R. E., 1991, "The 1991 IGTI Scholar Lecture: The Role of Laminar-Turbulent Transition in Gas Turbine Engines," J. Turbomach, **113**(4), pp. 509–536.

[32] Abu-Ghannam, B. J., and Shaw, R., 1980, "Natural Transition of Boundary Layers—The Effects of Turbulence, Pressure Gradient, and Flow History," Journal of Mechanical Engineering Science, **22**(5), pp. 213–228.

[33] Suzen, Y. B., and Huang, P. G., 2000, "Modeling of Flow Transition Using an Intermittency Transport Equation," J. Fluids Eng, **122**(2), pp. 273–284.

[34] Langtry, R., and Menter, F., "Transition Modeling for General CFD Applications in Aeronautics," *43rd AIAA Aerospace Sciences Meeting and Exhibit*, American Institute of Aeronautics and Astronautics.

[35] Suluksna, K., and Juntasaro, E., 2008, "Assessment of Intermittency Transport Equations for Modeling Transition in Boundary Layers Subjected to Freestream Turbulence," International Journal of Heat and Fluid Flow, **29**(1), pp. 48–61.

[36] Langtry, R. B., and Menter, F. R., 2012, "Correlation-Based Transition Modeling for Unstructured Parallelized Computational Fluid Dynamics Codes," AIAA Journal.

[37] Rogallo, R. S., 1981, "Numerical Experiments in Homogeneous Turbulence," NASA Tech Memo. 81315.

[38] Orszag, S. A., and Patterson, G. S., 1972, "Numerical Simulation of Three-Dimensional Homogeneous Isotropic Turbulence," Phys. Rev. Lett., **28**(2), pp. 76–79.

[39] Bhushan, S., and Walters, D. K., 2014, "Development of Parallel Pseudo-Spectral Solver Using Influence Matrix Method and Application to Boundary Layer Transition," Engineering Applications of Computational Fluid Mechanics, **8**(1), pp. 158–177.

[40] Frigo, M., and Johnson, S., 2011, "FFTW for Version 3.3."

[41] Bhushan, S., and Warsi, Z. U. A., 2005, "Large Eddy Simulation of Turbulent Channel Flow Using an Algebraic Model," International Journal for Numerical Methods in Fluids, **49**(5), pp. 489–519.

[42] Bhushan, S., Warsi, Z., and Walters, D., 2006, "Estimating Backscatter in Subgrid Scale Turbulence through Algebraic Modeling," AIAA Journal, **44**(4), pp. 837–847.

[43] Bhushan, S., and Warsi, Z., 2007, "Large Eddy Simulation of Free-Shear Flows Using an Algebraic Model," Computers & Fluids, **36**(8), pp. 1384–1397.

[44] Bhushan, S., 2018, "Performance and Error Assessment of Parallel Pseudo-Spectra Methods for Direct Numerical Simulations," Engineering Applications of Computational Fluid Mechanics, **revised version submitted**.

[45] Moser, R., Kim, J., and Mansour, N., 1999, "Direct Numerical Simulation of Turbulent Channel Flow up to Reτ= 590," Physics of fluids, **11**(4), pp. 943–945.

[46] Nagarajan, S., Lele, S. K., and Ferziger, J. H., 2007, "Leading-Edge Effects in Bypass Transition," Journal of Fluid Mechanics, **572**, pp. 471–504.

[47] Ovchinnikov, V., Choudhari, M. M., and Piomelli, U., 2008, "Numerical Simulations of Boundary-Layer Bypass Transition Due to High-Amplitude Free-Stream Turbulence," Journal of Fluid Mechanics, **613**, pp. 135–169.

[48] Bhushan, S., Borse, M., Walters, D. K., and Pasiliao, C. L., 2016, "Analysis of Turbulence Generation and Energy Transfer Mechanisms in Boundary Layer Transition Using Direct Numerical Simulation," *Volume 1A, Symposia: Turbomachinery Flow Simulation and Optimization; Applications in CFD; Bio-Inspired and Bio-Medical Fluid Mechanics; CFD Verification and Validation; Development and Applications of Immersed Boundary Methods; DNS, LES and Hybrid RANS/L*, p. V01AT08A006.

[49] Muthu, S., and Bhushan, S., 2017, "Temporal Direct Numerical Simulations for Flat-Plate Boundary Layer," Journal of UAB ECTC, **16**, pp. 87–93.

[50] Roach, P. E., and Brierly, D. H., 1990, "The Influence of a Turbulent Freestream on Zero Pressure Gradient Transitional Boundary Layer Development. P.1: Test Cases T3A and T3B," ERCOFTAC Workshop: Numerical simulation of unsteady flows and transition, pp. 319–347.

[51] Morkovin, M. V., 1969, "On the Many Faces of Transition," *Viscous Drag Reduction*, pp. 1–31.

[52] Spalart, P. R., and Venkatakrishnan, V., 2016, "On the Role and Challenges of CFD in the Aerospace Industry," Aeronautical Journal, **120**(1223), pp. 209–232.

[53] Schlatter, P., Brandt, L., de Lange, H. C., and Henningson, D. S., 2008, "On Streak Breakdown in Bypass Transition," Physics of Fluids, **20**, p. 101505.

[54] Wu, X., and Moin, P., 2009, "Direct Numerical Simulation of Turbulence in a Nominally Zero-Pressure-Gradient Flat-Plate Boundary Layer," Journal of Fluid Mechanics, **630**, pp. 5–41.

[55] Wu, X., Moin, P., Wallace, J. M., Skarda, J., Lozano-Durán, A., and Hickey, J.-P., 2017, "Transitional–Turbulent Spots and Turbulent–Turbulent Spots in Boundary Layers," Proceedings of the National Academy of Sciences, **114**(27), pp. E5292–E5299.

[56] Bhushan, S., Warsi, Z. U., and Walters, K. D., 2006, "Modeling of Energy Backscatter via an Algebraic Subgrid-Stress Model," AIAA journal, **44**(4), pp. 837–847.

[57] Kim, J., Moin, P., and Moser, R., 1987, "Turbulence Statistics in Fully Developed Channel Flow at Low Reynolds Number," Journal of fluid mechanics, **177**, pp. 133–166.

[58] Bhushan, S., and Walters, D. K., 2012, "A Dynamic Hybrid Reynolds-Averaged Navier Stokes - Large Eddy Simulation Modeling Framework," Physics of Fluids, **24**(1), pp. 1–7.

[59] Spalart, P. R., 1988, "Direct Simulation of a Turbulent Boundary Layer up to Reθ = 1410," Journal of Fluid Mechanics, **187**(December), pp. 61–98.

[60] Guarini, S. E., Moser, R. D., Shariff, K., and Wray, A., 2000, "Direct Numerical Simulation of a Supersonic Turbulent Boundary Layer at Mach 2.5," Journal of Fluid Mechanics, **414**(February 2000), pp. 1–33.

[61] Maeder, T., Adams, N. A., and Kleiser, L., 2001, "Direct Simulation of Turbulent Supersonic Boundary Layers by an Extended Temporal Approach," Journal of Fluid Mechanics, **429**, pp. 187–216.

[62] Ostoich, C. M., Bodony, D. J., and Geubelle, P. H., 2013, "Interaction of a Mach 2.25 Turbulent Boundary Layer with a Fluttering Panel Using Direct Numerical Simulation," Physics of Fluids, **25**(11), p. 110806.

[63] Wray, A., and Hussaini, M. Y., 1984, "Numerical Experiments in Boundary-Layer Stability," Proceedings of the Royal Society of London. A. Mathematical and Physical Sciences, **392**(1803), pp. 373–389.

[64] Piomelli, U., Zang, T. A., Speziale, C. G., and Hussaini, M. Y., 1990, "On the Large-Eddy Simulation of Transitional Wall-Bounded Flows," Physics of Fluids A: Fluid Dynamics, **2**(2), pp. 257–265.

[65] Rogers, M. M., Moser, R. D., and Buell, J. C., 1990, "A Direct Comparison of Spatially and Temporally Evolving Mixing Layers," Bull. Am. Phys. Soc, **35**, p. 2294.

[66] Akhavan, R., Ansari, A., Kang, S., and Mangiavacchi, N., 2000, "Subgrid-Scale Interactions in a Numerically Simulated Planar Turbulent Jet and Implications for Modelling," Journal of Fluid Mechanics, **408**, pp. 83–120.

[67] Mathur, A., Gorji, S., He, S., Seddighi, M., Vardy, A. E., O'Donoghue, T., and Pokrajac, D., 2018, "Temporal Acceleration of a Turbulent Channel Flow," Journal of Fluid Mechanics, **835**, pp. 471–490.

[68] Bobke, A., Orlu, R., and Schlatter, P., 2016, "Simulations of Turbulent Asymptotic Suction Boundary Layers," Journal of Turbulence, **17**(2), pp. 157–180.

[69] Kozul, M., Chung, D., and Monty, J. P., 2016, "Direct Numerical Simulation of the Incompressible Temporally Developing Turbulent Boundary Layer," Journal of Fluid Mechanics, **796**, pp. 437–472.

[70] Zhang, X., Watanabe, T., and Nagata, K., 2018, "Turbulent/Nonturbulent Interfaces in High-Resolution Direct Numerical Simulation of Temporally Evolving Compressible Turbulent Boundary Layers," Physical Review Fluids, **3**(9), p. 094605.

[71] Tsukahara, T., Seki, Y., Kawamura, H., and Tochio, D., 2014, "DNS of Turbulent Channel Flow at Very Low Reynolds Numbers," TSFP DIGITAL.

[72] Taylor, G. I., 1938, "Production and Dissipation of Vorticity in a Turbulent Fluid," Proceedings of the Royal Society of London. Series A-Mathematical and Physical Sciences, **164**(916), pp. 15–23.

[73] Piomelli, U., Balint, J.-L., and Wallace, J. M., 1989, "On the Validity of Taylor's Hypothesis for Wall-Bounded Flows," Physics of Fluids A: Fluid Dynamics, **1**(3), pp. 609–611.

[74] Brandt, L., Schlatter, P., and Henningson, D. S., 2004, "Transition in Boundary Layers Subject to Free-Stream Turbulence," Journal of Fluid Mechanics, **517**, pp. 167–198.

[75] Jimenez, J., Hoyas, S., Simens, M. P., and Mizuno, Y., 2010, "Turbulent Boundary Layers and Channels at Moderate Reynolds Numbers," Journal of Fluid Mechanics, **657**, pp. 335–360.

[76] Moser, R. D., Kim, J., and Mansour, N. N., 1999, "Direct Numerical Simulation of Turbulent Channel Flow up to Re_τ= 590," Physics of fluids, **11**(4), pp. 943–945.

[77] Andersson, P., Berggren, M., and Henningson, D. S., 1999, "Optimal Disturbances and Bypass Transition in Boundary Layers," Physics of Fluids, **11**(1), pp. 134–150.

[78] Westin, K. J. A., Boiko, A. V., Klingmann, B. G. B., Kozlov, V. V., and Alfredsson, P. H., 1994, "Experiments in a Boundary Layer Subjected to Free Stream Turbulence. Part 1. Boundary Layer Structure and Receptivity," Journal of Fluid Mechanics, **281**, pp. 193–218.

[79] Pope, S. B., 2000, *Turbulent Flows*, Cambridge University Press, Cambridge, MA.

[80] Bhushan, S., Walters, K. D., Muthu, S., and Pasiliao, C. L., 2018, "Identification of Bypass Transition Onset Markers Using Direct Numerical Simulation," Journal of Fluids Engineering, (140(11)), p. 111107.

[81] Sharma, O. P., Wells, R. A., Schlinker, R. H., and Bailey, D. A., 1981, "Boundary Layer Development on Turbine Airfoil Suction Surfaces," *ASME 1981 International Gas Turbine Conference and Products Show*, p. V001T01A013-V001T01A013.

[82] Bhushan, S., Walters, K. D., Muthu, S., and Pasiliao, C. L., 2018, "Identification of Bypass Transition Onset Markers Using Direct Numerical Simulation," Journal of Fluids Engineering, (Accepted for Publication).

[83] Emory, M., and Iaccarino, G., 2014, "Visualizing Turbulence Anisotropy in the Spatial Domain with Componentality Contours," Center of Turbulence Research, Annual Research Briefs, pp. 123–138.

[84] Voke, P. R., and Yang, Z., 1995, "Numerical Study of Bypass Transition," Physics of Fluids, **7**(9), pp. 2256–2264.

[85] Lardeau, S., Li, N., and Leschziner, M. A., 2007, "Large Eddy Simulation of Transitional Boundary Layers at High Free-Stream Turbulence Intensity and Implications for RANS Modeling," Journal of Turbomachinery.

[86] Chang III, P. A., Piomelli, U., and Blake, W. K., 1999, "Relationship between Wall Pressure and Velocity-Field Sources," Physics of Fluids, **11**(11), pp. 3434–3448.

[87] Kim, J., 1989, "On the Structure of Pressure Fluctuations in Simulated Turbulent Channel Flow," Journal of Fluid Mechanics, **205**, pp. 421–451.

[88] Jiménez, J., and Hoyas, S., 2008, "Turbulent Fluctuations above the Buffer Layer of Wall-Bounded Flows," Journal of Fluid Mechanics, **611**, pp. 215–236.

[89] Hu, N., Reiche, N., and Ewert, R., 2017, "Simulation of Turbulent Boundary Layer Wall Pressure Fluctuations via Poisson Equation and Synthetic Turbulence," Journal of Fluid Mechanics, **826**, pp. 421–454.

APPENDIX A

INTEGRAL BOUNDARY LAYER EQUATION

Reynolds averaged Navier-Stokes equations for incompressible flow for 2D turbulent boundary layer with a zero mean pressure gradient are:

$$\frac{\partial U}{\partial x}+\frac{\partial V}{\partial y}=0 \tag{A.1a}$$

$$\frac{\partial U}{\partial t}+U\frac{\partial U}{\partial x}+V\frac{\partial U}{\partial y}=\frac{\partial}{\partial y}\left\{\nu\frac{\partial U}{\partial y}\right\}-\left[\frac{\partial\overline{u'u'}}{\partial x}+\frac{\partial\overline{u'v'}}{\partial y}\right] \tag{A.1b}$$

where, U and V are the ensemble averaged streamwise and wall-normal velocities, and u' and v' are the corresponding turbulent velocity fluctuations, and ν is the kinematic viscosity. Integrating the momentum equation over the boundary layer leads to:

$$\int_0^\delta\frac{\partial U}{\partial t}dy+\int_0^\delta U\frac{\partial U}{\partial x}dy+\int_0^\delta V\frac{\partial U}{\partial y}dy=\int_0^\delta\frac{\partial}{\partial y}\left\{\nu\frac{\partial U}{\partial y}\right\}dy-\int_0^\delta\frac{\partial\overline{u'u'}}{\partial y}dy-\int_0^\delta\frac{\partial\overline{u'v'}}{\partial x}dy \tag{A.2}$$

Using integration by part for the 3rd term on the left-hand side, LHS, results in:

$$\frac{\partial}{\partial t}\int_0^\delta Udy+\int_0^\delta U\frac{\partial U}{\partial x}dy+UV|_0^\delta-\int_0^\delta U\frac{\partial V}{\partial y}dy=\nu\frac{\partial U}{\partial y}\Big|_0^\delta-\overline{u'v'}|_0^\delta-\frac{\partial}{\partial x}\int_0^\delta\overline{u'u'}dy \tag{A.3}$$

Using no-slip boundary condition at $y=0$, wall shear stress $\tau_w=\rho\nu\frac{\partial U}{\partial y}$ at $y=0$ and $\frac{\partial U}{\partial y}=0$ at $y=\delta$, and turbulent shear stress $\overline{u'v'}=0$ at both $y=0$ and δ. Above equation simplifies to:

$$\frac{\partial}{\partial t}\int_0^\delta U dy + \int_0^\delta U\frac{\partial U}{\partial x}dy + U_0 V|_\delta - \int_0^\delta U\frac{\partial V}{\partial y}dy = -\frac{1}{\rho}\tau_w - \frac{\partial}{\partial x}\int_0^\delta \overline{u'u'}dy \tag{A.4}$$

where, U_0 is the free-stream velocity. Integrating mass conservation Eq. (A.1a) over the boundary layer gives:

$$V|_\delta = -\int_0^\delta \frac{\partial U}{\partial x}dy \tag{A.5}$$

Also note that the 2nd and 4th term on LHS of Eq. (A.4) can be combined using Eq. (A.1a), which results in:

$$\frac{\partial}{\partial t}\int_0^\delta U dy + 2\int_0^\delta U\frac{\partial U}{\partial x}dy - \int_0^\delta U_0\frac{\partial U}{\partial x}dy = -\frac{1}{\rho}\tau_w - \frac{\partial}{\partial x}\int_0^\delta \overline{u'u'}dy \tag{A.6}$$

The displacement thickness, $\delta^* = \int_0^\delta \left(1 - \frac{U}{U_0}\right)dy$, thus above equation can be reorganized as:

$$U_0\frac{\partial \delta^*}{\partial t} - \frac{1}{\rho}\tau_w = 2\int_0^\delta U\frac{\partial U}{\partial x}dy - \int_0^\delta U_0\frac{\partial U}{\partial x}dy + \frac{\partial}{\partial x}\int_0^\delta \overline{u'u'}dy \tag{A.7}$$

Note that it is assumed that mass with the boundary layer remains constant. The first two terms on the right-hand side can be combined as below:

$$U_0 \frac{\partial \delta^*}{\partial t} - \frac{1}{\rho}\tau_w = \int_0^{\delta} \frac{\partial}{\partial x}(U^2 - U_0 U)dy + \frac{\partial}{\partial x}\int_0^{\delta} \overline{u'u'}dy \tag{A.8}$$

Using the definition of momentum boundary layer thickness, $\theta = \int_0^{\delta} \frac{U}{U_0}\left(1 - \frac{U}{U_0}\right)dy$ results in:

$$U_0 \frac{\partial \delta^*}{\partial t} - \frac{1}{\rho}\tau_w = -{U_0}^2 \frac{\partial \theta}{\partial x} + \frac{\partial}{\partial x}\int_0^{\delta} \overline{u'u'}dy \tag{A.9}$$

Introducing $\frac{1}{{U_0}^2}\int_0^{\delta} \overline{u'u'}dy = U'$ for convenience, above equation simplifies to:

$$\frac{\partial \delta^*}{\partial t} - \frac{1}{\rho U_0}\tau_w = -U_0 \frac{\partial}{\partial x}(\theta - U') \tag{A.10}$$

For a temporally developing simulations, the right-hand side term represents the numerical errors due to spatial growth of the boundary layer within the domain.

For spatially developing simulations, the temporal growth is assumed to be negligible, thus the momentum integral equation is:

$$\frac{1}{\rho U_0^2}\tau_w = \frac{\partial}{\partial x}(\theta - U') \tag{A.11}$$

For a domain velocity $V_{D,MI}$, and assuming that the domain translation does not depend significantly on its acceleration, the spatial translation can be written in terms of time as:

$$x = V_{D.MI}t \tag{A.12}$$

Using Eq. (A.12) in Eq. (A.11) an expression for the domain velocity is derived as below:

$$V_{D,MI} = \frac{\partial}{\partial t}(\theta - U')/\frac{1}{2}C_f \tag{A.13}$$

where,

$$C_f = \frac{1}{\frac{1}{2}\rho U_0^2}\tau_w \tag{A.14}$$